TÉCNICO LISBOA

UNIVERSIDADE DE LISBOA
INSTITUTO SUPERIOR TÉCNICO

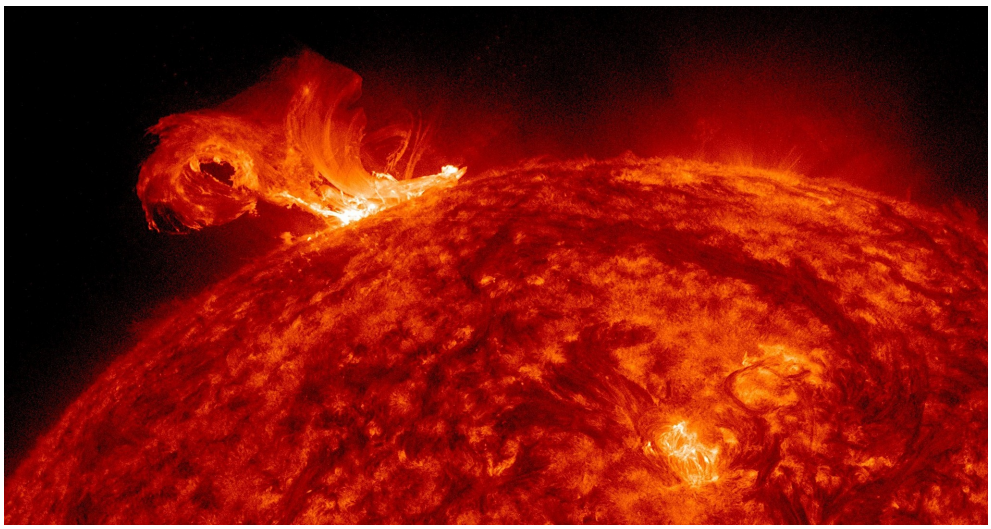

LFS/HFS edge and SOL plasma turbulence studies using fixed frequency reflectometers at AUG

Valentina Nikolaeva

Supervisor: Doctor Maria Emília Morais da Fonseca e Silva da Costa Manso
Co-Supervisors: Doctor Carlos Alberto Nogueira Garcia da Silva

Thesis approved in public session to obtain the PhD Degree in

Technological Physics Engineering

Jury final classification: Pass

2018

TÉCNICO LISBOA

UNIVERSIDADE DE LISBOA
INSTITUTO SUPERIOR TÉCNICO

LFS/HFS edge and SOL plasma turbulence studies using fixed frequency reflectometers at AUG

Valentina Nikolaeva

Supervisor: Doctor Maria Emília Morais da Fonseca e Silva da Costa Manso
Co-Supervisors: Doctor Carlos Alberto Nogueira Garcia da Silva

Thesis approved in public session to obtain the PhD Degree in

Technological Physics Engineering

Jury final classification: Pass

Jury

Chairperson: Doctor Luís Paulo da Mota Capitão Lemos Alves, Instituto Superior Técnico, Universidade de Lisboa.

Members of the committee:

Doctor Maria Emília Morais da Fonseca e Silva da Costa Manso, Instituto Superior Técnico, Universidade de Lisboa;
Doctor Maria Teresa Estrada Garcia, Laboratorio Nacional de Fusión, Centro de Investigaciones Energéticas, Medioambientales y Tecnológicas (CIEMAT), Spain;
Doctor Garrard David Conway, Max-Planck-Institut für Plasmaphysik, Germany;
Doctor Bruno Miguel Soares Gonçalves, Instituto Superior Técnico, Universidade de Lisboa.

Funding Institutions

Fundação para a Ciência e a Tecnologia, EUROfusion

2018

Resumo

Um dos principais desafios para o desenvolvimento da energia de fusão é compreender e controlar a turbulência na periferia do plasma e o transporte que lhe está associado. Isto é essencial para melhorar o desempenho da fusão e fazer extrapolações realistas para os próximos reatores de fusão. Esta tese apresenta um estudo sobre turbulência no tokamak ASDEX Upgrade (AUG) usando principalmente dados obtidos com o diagnóstico de reflectometria de onda contínua modulada em frequência (FM-CW) que permite medir perfis de densidade e flutuações no lado de campo magnético alto (HFS) e no lado de campo magnético baixo (LFS), com elevadas resoluções, espacial e temporal, cobrindo regiões dentro e fora da separatrix magnética do plasma. É apresentada pela primeira vez no AUG, uma visão global da turbulência e das suas assimetrias poloidais nas regiões da periferia e da designada "scrape-off layer" (SOL). Os dados do HFS são particularmente relevantes devido à falta de informação geral sobre esta região do plasma. Estudou-se a turbulência em situações em que as propriedades do plasma da periferia e do SOL devem mudar significativamente, nomeadamente em diferentes configurações magnéticas, regimes de confinamento (modo L e fase intermédia, "I phase") e condições de "detachment" do diversor. Foi desenvolvida uma metodologia para obter o nível de flutuações $\delta n_e/n_e$ a partir dos sinais de reflectometria homodínicos. No modo L os resultados mostram que $\delta n_e/n_e$ aumenta com o raio no HFS e no LFS. No LFS SOL, as flutuações de densidade são um fator 2 mais elevadas do que no HFS, de acordo com o transporte do tipo "ballooning". Em configurações magnéticas diferentes (nulo superior simples USN, nulo duplo DN, nulo inferior simples LSN) as ligações entre o HFS e o LFS são modificadas principalmente no SOL. As flutuações de densidade no LFS são maiores do que no HFS para todas as configurações magnéticas. As modificações das flutuações de uma configuração para outra são pronunciadas apenas no SOL e a assimetria HFS/LFS mais forte ocorre na configuração DN. Os dois resultados anteriores suportam um forte mecanismo de transporte do tipo "ballooning". O nível de flutuações mais baixo na topologia DN do que na LSN, no HFS e no LFS, está provavelmente associado a diferenças no cisalhamento do campo elétrico radial Er. Os resultados numéricos obtidos com estudos de simulação realizados com o código girofluido GEMR estão de acordo com os resultados experimentais. A comparação entre a fase intermédia ("I phase") em DN e LSN mostra que as flutuações de densidade na periferia apresentam uma dependência fraca da configuração magnética mas são bastante sensíveis

a mudanças de confinamento. As oscilações do tipo “limit cycle” (LOCs) modulam as flutuações de alta frequência na periferia, em fase com as perturbações do campo magnético, e de forma não uniforme ao longo do raio, propagando-se para o interior do plasma com uma velocidade aproximada de $\sim 200 - 300$ m/s. Nas descargas de rampa de densidade em modo L, com diferentes estados de “detachment” do diversor, as flutuações de densidade no SOL LFS apresentam uma variação modesta com o aumento da densidade do plasma, a qual resulta principalmente de uma subida das componentes de baixa frequência ($<$ 15 kHz). Quando o diversor do lado exterior começa a ficar “detached”, os resultados experimentais mostram um achatamento do perfil de densidade do SOL o que está de acordo com um aumento da convecção dos filamentos no LFS. Ao mesmo tempo no HFS SOL, as flutuações de densidade aumentam fortemente, o que pode estar associado à presença de filamentos mais rápidos, que tiveram origem no LFS. O nosso estudo sobre a turbulência, suportado em experiências com diferentes configurações magnéticas, regimes de confinamento e estados do diversor, dá pela primeira vez uma visão conjunta das assimetrias poloidais da turbulência, na periferia e no SOL do AUG. Esta importante contribuição para a caracterização da turbulência só foi possível devido às capacidades de medida do diagnostic FM-CW do AUG, nomeadamente a sua operação em modo ordinário (O), que depende apenas da densidade do plasma; a cobertura larga incluindo a periferia do plasma e o SOL, a sondagem no HFS, onde os dados são escassos e as medidas únicas simultâneas nos lados HFS e LFS, com elevadas resoluções especial e temporal.

Palavras-chave: plasma, fusão nuclear, turbulência, flutuações, reflectometria

Abstract

One of the main challenges towards fusion energy is to understand and control the edge turbulence and the associated transport in present devices. This is essential to improve fusion performance and to make realistic extrapolations for future fusion reactors.

This thesis presents a study of turbulence at the ASDEX Upgrade (AUG) tokamak using mainly data from the frequency modulated-continuous wave (FM-CW) reflectometry diagnostic that measures density profiles and fluctuations both at the High field side (HFS) and the Low field side (LFS) with high spatial and time resolutions, covering regions inside and outside the separatrix.

A consistent picture about turbulence and its poloidal asymmetries in the edge and scrape-off-layer (SOL) is presented for the first time at AUG. HFS data is most relevant due to the lack of density data in that plasma region. Turbulence was studied in situations where the edge/SOL plasma properties should be significantly modified, namely different magnetic configurations, confinement regimes (low confinement regime (L-mode) and I-phase) and divertor conditions.

A methodology was developed to obtain the level of density fluctuations $\delta n_e/n_e$ from the homodyne FM-CW reflectometry signals. In L-mode, results show that $\delta n_e/n_e$ increase with radius at both the HFS and the LFS. In the LFS SOL, density fluctuations are a factor of two larger than at the HFS, which is in agreement with ballooned transport.

In different magnetic configurations (upper single null USN, double null DN, lower single null LSN) the connections between the HFS and the LFS are modified mainly in the SOL. Density fluctuations at the LFS are larger than at the HFS for all magnetic configurations. The modifications of fluctuations from one configuration to the other are mainly pronounced at the SOL and the strongest HFS/LFS asymmetry occurs for the DN configuration. Both findings support a strong ballooning-like transport mechanism. The observed lower level of density fluctuations for USN than for LSN topology both at the HFS and the LFS, is possibly associated with differences in the radial electric field shear. Numerical results from dedicated simulations performed with the gyrofluide GEMR code are in a good agreement with the experimental results.

The comparison between I-phase in DN and LSN reveal that density fluctuations in the edge display a weak dependence on the magnetic configuration and are quite sensitive to confinement modifications. The limit cycle oscillations (LCOs) modulate the high frequency fluctuations at the edge in phase with the magnetic field perturbations in a non radially uniform way and propagating inward with a velocity $\sim 200 - 300$ m/s.

In L-mode ramp-up discharges with different divertor detachment states, the SOL density fluctuations at the LFS shows a modest variation with increasing background density resulting mainly from a rise of low frequency components ($<$ 15 kHz). At the beginning of the outer divertor detachment, experimental results display a flattening of SOL density profile in good agreement with an enhanced convection of filaments at the LFS. At the same time at the HFS SOL density fluctuations display a strong increase, which may be associated with the presence of faster filaments originated at the LFS.

Our study of turbulence, supported in a wide range of experiments with different magnetic configurations, confinement regimes and divertor states, provides for the first time a picture of the edge and SOL poloidal asymmetries of turbulence at AUG. This important contribution to improve the characterization of turbulence was only possible due to the measuring capabilities of the FM-CW diagnostic at AUG namely ordinary (O) mode operation solely depending on the plasma density, broad coverage including edge and SOL regions, HFS probing where data

is scarce, and unique simultaneous HFS and LFS measurements with both high spatial and temporal resolutions.

Keywords: plasma, fusion, turbulence, fluctuations, reflectometry

Acknowledgments

During this PhD program I worked with people from IPFN IST and IPP scientific groups, I am very grateful to every person I met and contacted during this time. I would like to acknowledge my family that always supported me, especially when I worked abroad, this thesis is dedicated to my parents. A special thank to my husband for his faith and endless love, being always by my side despite the distance.

This research work would not be done without the constant support, limitless encouragement and patient guidance of my supervisors, I would like to express my gratitude and deep regards to Prof. Maria Emília Manso and Dr. Carlos Silva. I would like to thank Dr. Garrard Conway for his advice and valuable suggestions regarding reflectometry data analysis. I am also deeply indebted to Dr. Peter Manz for his interest in my research, fruitful discussions of experimental results with theoretical background and running the simulation code GEMR. I would like to thank Prof. Ulrich Stroth for his useful critiques and time he dedicated for reading and improvement of this thesis. I am very grateful to Dr. Vladimir Vershkov for his detailed explanations of reflectometry issues and discussions about plasma turbulence.

I would like to express my gratitude to IPFN Reflectometry Group colleagues, particularly Dr. Antonio Silva, Dr. Jorge Santos, Dr. Filipe Silva, Luis Guimarais, Dr. Jose Vicente, Diogo Aguiam, Egor Seliunin and Luis Gil. Thanks for providing a great support in operation of the reflectometry diagnostics and being always ready to help with any issue.

I am very grateful to the whole ASDEX Upgrade team, in particular Dr. Elisabeth Wolfrum, Dr. François Ryter, Dr. Marco Wischmeier and Dr. Thomas Puetterich, for the help with experiments preparation and all the discussions.

My very special thanks to Anton Bogomolov who was always ready to help me with programming and to support me with absolutely everything. Most of the brightest events and stories of these years were related to the friendship I have been granted by Dr. Anton Bogomolov, Dr. Anna Medvedeva, Dr. Dmytro Meshcheriakov, Dr. Dmitrii Prisiazhniuk, Dr. Serhiy Mochalskyy, Ivan Erofeev and all other members of 'drinking tea scientific mafia' team. My enormous gratitude to Lena Kondratieva and Katya Fokina for all the good moments we spent together.

I am very grateful to the Erasmus Mundus International Doctoral College in Fusion Science and Engineering (FUSION-DC) for providing me this possibility to become part of the PhD program and to the EUROfusion Consortium for their financial support.

Last, but not least, I would like to thank my graduate work supervisor Valery Kurnaev at MEPhI for introducing me to this beautiful world of plasma physics and fusion with his enthusiastic encouragement and support.

Contents

List of Tables

List of Figures

Chapter 1

Introduction

"Everything is theoretically impossible, until it is done."

— Robert A. Heinlein

1.1 Nuclear Fusion

Nuclear Fusion is the process that powers the Sun and the stars. In the core of the Sun, at temperatures of $10 - 15$ million Kelvin, the hydrogen is converted to helium by fusion reactions generating enough energy to keep the Sun burning and to sustain life on Earth.

With expansion both of the world population and its dependence on energy supplies the demand on energy increased enormously. The need to find new and sustainable energy sources becomes critical in view of the environmental harm due to the CO_2 emission associated with the burning of fossil fuels and the long-lived radioactive waste from nuclear fission plants.

If the sun's fusion processes could be reproduced on the earth, hydrogen (for example, derived from water) could be used as an almost unlimited and powerful energetic fuel. However, it is not possible to reproduce on Earth the sun's considerable gravitational forces that confine its fusion reactions.

In order to get a fusion reaction two light nuclei should be on a very short distance (in order of 10^{-15} m) from each other, for atomic forces start to attract them. As the Coulomb barrier prevents the charged particles to approach each other, high kinetic energy is needed to overcome the barrier. The Coulomb barrier increases proportionally to the product of the charges Z of both nuclei. Consequently, it is easier to make fusion for the lightest nuclei, like nuclei of hydrogen isotopes as they have $Z = 1$.

The condition for sustainable fusion reactions to occur in the plasma, is that the triple prod-

uct: (plasma temperature $T\times$ density $n\times$ confinement time τ_E), surpasses a certain value derived from the Lawson Criterion. That is the value ($T \times n \times \tau_E$) to overcome the Coulomb barrier and for high fusion reaction rate to occur making the fusion reactions self-sustainable. The plasma is close to that condition for:

$$n \cdot \tau_E \cdot T > 5 \cdot 10^{21} \, [\mathrm{m}^{-3} \cdot \mathrm{s} \cdot \mathrm{keV}]. \tag{1.1}$$

Values higher that the critical in eq. 1.1 lead to a positive energy balance, which means that the produced fusion energy is higher than the external input energy source. Several schemes for fusion energy production have been developed, presently the most promising one is the confinement of the fusion plasma with magnetic fields.

For the highest achievable magnetic fields, the plasma temperature should be $100 - 200$ million Kelvin, the central density in the plasma should reach $1-2\cdot10^{20}$ particles per cubic meter and the energy confinement time should be $4 - 6$ seconds. The confinement time increases substantially with plasma size, for example, the Sun has an extensive energy confinement time. Non magnetic plasma confinement devices are also being investigated, mainly based on the inertial confinement or laser-induction [12].

On Earth fusion reactions more efficient than in the Sun are needed, such as those between two heavier forms of hydrogen: deuterium (D) and tritium (T):

$$D + T \rightarrow n + {}^4He + 17.6\,\mathrm{MeV} \tag{1.2}$$

$$T + T \rightarrow 2n + {}^4He + 11.3\,\mathrm{MeV}. \tag{1.3}$$

The $D - T$ reaction requires the lowest temperature T, density n and confinement time τ_E, so the D-T gas is considered as a favorable fuel for fusion reaction.

Also, reactions without producing of neutrons are considered. Their benefit is the absence of induced radioactivity. One of the most promising reactions is:

$$p + {}^{11}B \rightarrow 3\ {}^4He + 8.7\,\mathrm{MeV}, \tag{1.4}$$

but this requires a much higher performance of the fusion reactor, with the triple product being two orders of magnitude higher than the one for a $D - T$ reaction [13].

1.2 Magnetic confinement

The fusion plasma is kept inside a vacuum vessel with a torus-shaped chamber, which provides a high-vacuum environment and a radiation shielding. In a tokamak, the larger is the vacuum chamber volume, the easier is to confine the plasma and to achieve a large number of fusion reactions.

As plasma consists of both positive and negative charged particles, electric and magnetic fields can be used to isolate the plasma from the walls of the containment vessel. This isolation reduces the conductive heat loss through the vessel and also minimizes the release of impurities from the vessel walls into the plasma, which contaminate and cool down the plasma due to radiation losses. A rotational transform of the toroidal magnetic field may prevent the curvature drift of plasma particles towards the wall. As proposed by Spitzer and Mercier [14, 15], there are three different ways to twist the magnetic field: (i) creating a poloidal field by a toroidal electric current; (ii) rotating the poloidal cross-section of stretched flux surfaces around the torus; (iii) making the magnetic axis non-planar. There are two classes of magnetic confinement devices: tokamaks and stellarators [16], while tokamaks use the first approach, stellarators usually rely on the latter two methods.

Tokamak

The word "tokamak" is an abbreviation for "toroidal camera with magnetic coils" (Russian: "**to**roidalnaya **ka**mera s **ma**gnitnymi **ka**tushkami)" [17]. The concept of tokamak implies a relatively simple construction based on a toroidally shaped vacuum chamber, where the plasma is created, with magnetic coils over the chamber. The plasma is confined inside the chamber by a superposition of toroidal and poloidal magnetic fields. The tokamak principle is schematically illustrated in Fig. 1.1. The toroidal magnetic field is created by the external toroidal magnetic coils, whereas the poloidal field is created by a current which is induced in the plasma [18]. The use of the plasma current is the main feature of the tokamak class devices. A transformer is used to induce the current in the plasma, being the secondary coil. The current in tokamaks is also used to heat the plasma by means of ohmic heating.

Stellarator

In stellarators, the magnetic field is completely created and twisted by external non-axisymmetric magnetic coils. The coil design of stellarators is much more complicated in comparison with the tokamak requiring a very precise calculation and manufacturing. However, with techni-

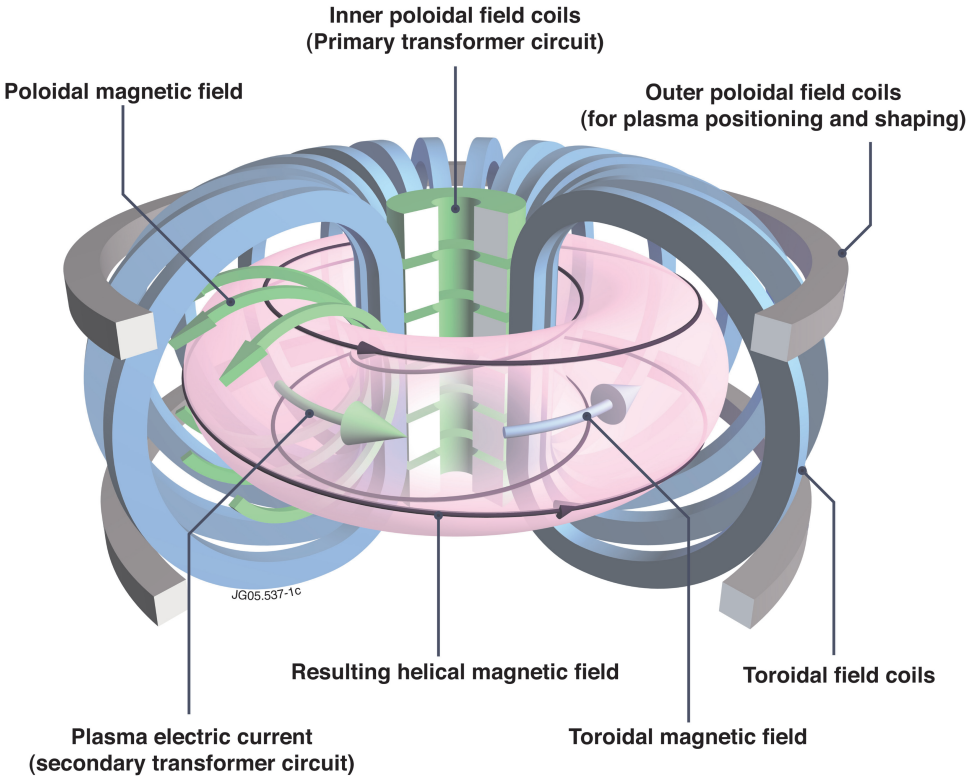

Figure 1.1: Schematic view of the tokamak principle: arrangement of magnetic field coils and the resulting magnetic field that confines the plasma [1].

cal advances in the last decades the stellarator concept became a plausible alternative to the tokamak. The stellarators are able to operate the plasma in steady state since there is no transformer as in the tokamaks. However the more unconfined particle orbits in the stellarators can lead to high neoclassical transport of energetic and thermal particles. Overall, the advantages of stellarators include intrinsically steady-state operation, less MHD activities and nearly disruption-free [19].

1.3 Heating

Fusion plasmas loose energy at their edge and therefore must be heated to achieve the fusion relevant temperatures.

Ohmic heating

An effective heating mechanism in tokamaks is the Ohmic heating (OH) due to the induced plasma current I_p. The plasma current provides the poloidal magnetic field and consequently produces the heat resulting from the ohmic resistance of the plasma. Ohmic heating is limited by the following reasons: (i) the plasma current is induced via transformer that employs an

increasing magnetic field that does not allow continuous plasma operation; (ii) the heating become ineffective at high temperatures because the electric resistivity described by the Spitzer conductivity strongly decreases with plasma temperature. In order to obtain the necessary target temperatures and to keep a continuous heat, additional heating is required. Neutral particle beams (NB) heating and resonant electromagnetic waves (radio frequency, RF) heating are used. Those two main schemes for plasma heating are presented in Figure 1.2.

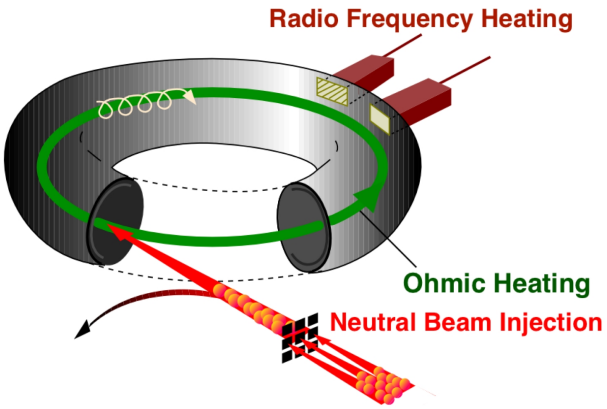

Figure 1.2: Schematic representation of tokamak plasmas heating [2].

Neutral beam and radio-frequency heating

Neutral beams as well as electromagnetic waves are used for the additional energy deposition that modifies the plasma parameters profiles. This technique is referred as "plasma tailoring" and is used to optimize the plasma performance and/or to improve the plasma confinement.

Additional plasma heating by neutral beams is based on neutral injection. The beam atoms carry a large unidirectional kinetic energy. In the plasma, the beam atoms loose electrons due to collisions, i.e. they get ionized and as a consequence they are captured by the magnetic field of tokamak. These new ions are much faster than the average plasma particles. In a series of subsequent ion-ion, ion electron and electron-electron collisions, the energy of the beam atoms results in an increased mean velocity of the chaotic motion of all plasma particles and thereby the neutral beam heats the plasma.

The neutral beams in fusion experiments are usually formed with atoms of the hydrogen isotopes (hydrogen, deuterium or tritium). The beam consists of neutral atoms otherwise it could not penetrate through the strong magnetic field that confines the fully ionized plasma. The beam energy (corresponding to the velocity of its atoms) should be sufficient to reach the

plasma center because if the beam atoms were too slow they would get ionized immediately at the plasma edge.

RF heating uses electromagnetic waves with certain frequencies to produce strong heating through resonant absorption, which is a collisionless process. Resonant absorption can take place in the magnetized plasma at several resonant frequencies corresponding to the different plasma particles. Ion cyclotron resonance heating (ICRH) and electron cyclotron resonance heating (ECRH) are typically used. The basic layout for the RF heating scheme is an efficient high power generator at a remote location from the plasma, a low-loss transmission line and an efficient antenna to couple the electromagnetic energy to the plasma. The wave propagation in the plasma is required to be with negligible loss to localize the absorption zone of energy deposition. The location of the absorption should be externally controlled in order to be more effective and to avoid deposition/reflection on the plasma facing components.

1.4 Plasma edge and SOL

In order to increase the volume of the high temperature plasma (to increase fusion reactions), the geometry of the tokamak has been optimized so that most of the temperature drop from the plasma core takes place over the few centimeters near the vessel walls. Therefore, in this region, which is called the plasma edge, the temperature may decrease by several tens of million degrees per centimeter. The edge region has been the focus of intense research in the last decades due to its key role in the plasma wall interactions (namely power and particle exchanges) that influence also the core plasma. Indeed, the plasma edge region can protect the plasma-facing components and also to prevent the plasma from cooling down due to impurity ejection.

The region with open magnetic field lines is called the scrape-off-layer (SOL). Usually it is a region with a few cm width outside the Last Closed Flux Surface (LCFS), which is the so-called separatrix that separates the plasma regions with close and open field lines.

In an idealized scenario, the plasma particles guided along the closed field lines following the Lorentz force (see Figure 1.3) have no collisions with the first wall. In reality, there are processes that force plasma particles to leak out from the confined region. Particles may leave the confined region due to classical diffusion processes, for example changing from a close guiding field line to an open one due to collisions with other plasma particles. However, the radial transport associated with the diffusion and collisions of particles is negligible in comparison with the anomalous transport that is always present in fusion experiments. The source of that transport is the plasma turbulence driven by complex instability mechanisms (see chapter 2).

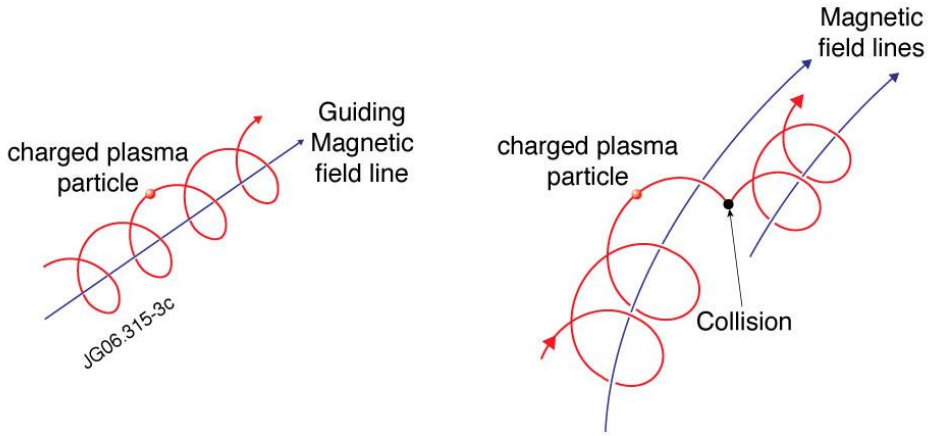

Figure 1.3: Schematic representation of plasma particles movements along the field lines [3].

1.5 Limiters and divertors

There are two ways by which the last closed field line can be delimited. The simplest option is to insert a barrier into the plasma, this is called a limiter and essentially it protects the walls from the hot core plasma. This solution has two main disadvantages: (i) any material released by the impact of the plasma on the limiter could penetrate straight into the confined region and degrade the plasma properties, (ii) in a reactor it would not be possible to sufficiently pump away the helium ash (resulting from fusion reactions and diluting the core plasma). Therefore a more sophisticated solution was developed using a modification of the magnetic field lines at the plasma edge, so that the field lines of the SOL are diverted into a dedicated region where the plasma exhaust ends up in collisions with the wall (the target plates) or with a gas. This is called a divertor configuration, shown in Fig. 1.4, with the diversion of the field lines at the bottom. The divertor configuration has been shown experimentally to be more advantageous than the limiter one. The main purpose of limiters and divertors is to separate the plasma from the first wall and to improve the tokamak performance. Within each flux surface the particles can move freely, leading to much faster movements along the magnetic field lines than perpendicular to them, so particles are transported mainly along the field lines into the divertor targets. Also, by cross-field transport particles enter the SOL and move radially outwards into the wall. In its simplest form, due to the radial exponential decay of the temperature and density, the heat and particle fluxes onto the walls become sustainable for the wall materials. Most particles and nearly all the power entering the SOL are immediately guided along the open magnetic field lines to the limiters or to the divertor targets.

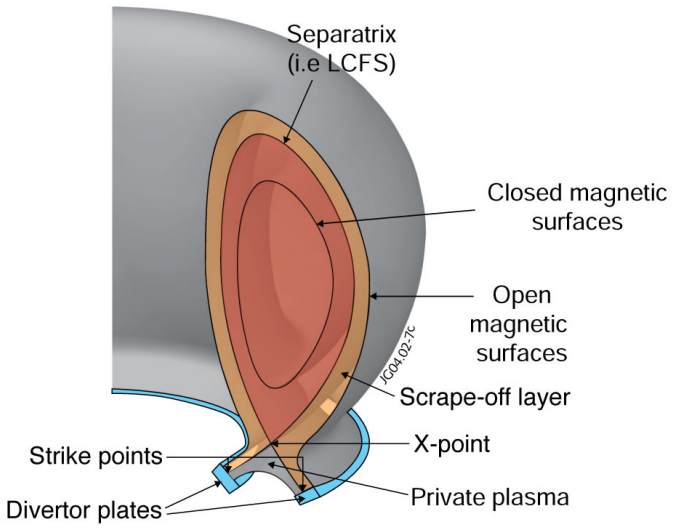

Figure 1.4: Geometry of a toroidal magnetic field with a divertor [1].

Main advantages of divertors

The divertor concept presents important advantages over limiters, namely:

- The materials facing the exhaust plasma are not in any direct contact with the main (confined) plasma so tokamaks with divertor plasmas have lower levels of impurities in the core plasma. As a result they tend to achieve much higher temperatures in the core, increasing the probability for fusion reactions.

- The so-called high confinement mode (or H-mode) discovered in 1982 [20], can be achieved nearly exclusively in the presence of divertors. In the improved confinement, a cross-field transport barrier reduces significantly the transport into the SOL, followed by the steepening of both the density and temperature edge profiles.

- The divertor plasma is not transparent to neutrals and a large proportion of the neutrals are re-emitted from the divertor target and are re-ionized in the divertor region without reaching neither the SOL nor the core plasma (see section 1.6). On average, the recycled neutrals and molecules are emitted perpendicularly to the recycling surfaces (divertor targets) [21]. Hence, the target orientation can determine the region where the neutrals will be ionized. Divertor design has been focused on achieving large re-ionization in the divertor for the widest possible range of operating plasma conditions (i.e. temperature and density at the separatrix). A divertor where intense neutral (and impurity) re-ionization takes place, produces large energy losses (ionization and radiative), which decrease the power load into the divertor plates [22]. Those losses contribute to the reduction of the

plasma temperature at the divertor target which, in turn, can reduce the physical sputtering of the target. Also, when the neutral pressure at the divertor increases it makes particle pumping easier.

The disadvantage of the divertor configuration is that it reduces the volume where fusion reactions take place. Once the most expensive units of a tokamak are the magnetic field coils, the volume inside such coils in which fusion reactions can occur needs to be maximized to make fusion cost efficient, so the divertor increases the reactor costs as compared to a limiter approach.

1.6 Divertor detachment

Plasma transport parallel to the magnetic field is assumed to be governed by Coulomb collision. By making some simplifying assumptions a model has been proposed relating divertor and main SOL parameters without calculating the quantities in between, the so-called two-point model [23]. Two limits are found with this model: (i) a conduction limited regime, where the temperature values at the target plates are significantly lower than at the mid-plane; and (ii) a convection sheath limited regime, where both temperatures are nearly equal.

The sheath limited regime occurs only at low densities, i.e. low collisionality. That regime is characterized by a small ionization (low recycling) in the divertor as compared to the detachment regime. Particles and power enter the SOL upstream at the stagnation point and flow downstream into the target plate, being accelerated up to the sound speed at the target according to the Bohm criterion. The sheath heat transmission factor determines the parallel heat flux through the SOL. Most of the power undergoes convection, so the temperature drop along field lines in the SOL is negligible. At higher collisionality (higher density), the dominant type of the heat transport changes from convective to conduction in the SOL and temperature gradient along the magnetic field lines from upstream to target increases. As the temperature in the divertor decreases over a large volume, electrons and ions can recombine to form neutrals volumetrically. This process is amplified by the presence of those neutrals that, once recycled at the solid surfaces, act as a “break” for the plasma that flows towards the targets. They increase the time that the charged particles have for recombination, making this process more likely to happen. When this occurs in large quantities the measured particle flux at the target plates drops by more than an order of magnitude. Neutral atoms transport the residual power and as they are not bound by magnetic field lines, they can deposit power and particles over broad areas reducing the peak values to acceptable levels for materials to sustain the bom-

bardment. This regime is known as the detachment divertor regime as the plasma becomes detached (separated) from the solid surfaces. Plasma detachment allows higher operating temperatures upstream. Due to the high neutral particle densities/pressures established in the divertor volume in front of the pump ducts, the pumping of the helium ash becomes more efficient. Following the decreased connection of the plasma with the plasma facing material the impurities may be reduced. Both regimes are schematically presented in Fig. 1.5.

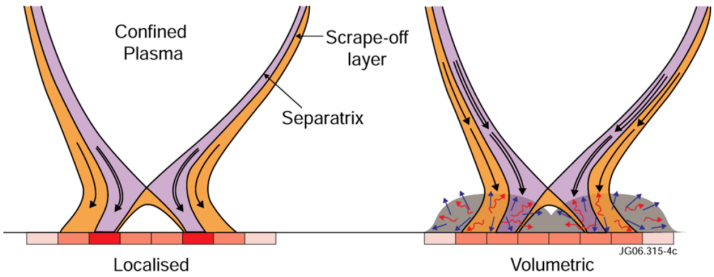

Figure 1.5: Sheath-limited (left) and detachment (right) divertor regimes. In the high recycling regime part of the energy is carried by radiation or CX neutrals which reduce the peak heat flux in the strike lines [4].

1.7 Magnetic configuration

The plasma configuration is settled up by magnetic fields. The currents in the magnetic coils, in the plasma and in the first wall influence the magnetic topology in the machine. The shape and position of the plasma is controlled by a set of vertical magnetic field coils. By changing the vertical magnetic fields strength in the corresponding coils, the plasma can be moved in vertically and field nulls can be created. Therefore, different magnetic configurations can be achieved: upper single null (USN), lower single null (LSN) and double-null (DN) configurations with the location of the X-points at the top, bottom or top plus bottom, correspondingly. Also, the polarity of the toroidal magnetic field and the toroidal current (i.e. the poloidal magnetic field) can be reversed. The magnetic topology of the divertor configuration guides the edge plasma towards the target plates. As the magnetic configurations differ mainly at the edge and SOL, the plasma properties are expected to be modified mostly in those regions.

1.8 Operational regimes

1.8.1 The H-mode confinement regime

The mode with improved confinement properties (H-mode) in comparison to the standard regime (L-mode) was discovered at ASDEX tokamak [20] in divertor configuration. Later this regime had been also observed in other tokamaks and stellarators, either with poloidal field divertors or with pure limiter geometry [24]. It was found that the transition from the low confinement state (L-mode) to the high confinement state (H-mode) occurs when a certain heating power threshold is surpassed and it does not depend on the type of heating [25]. The transition to the H-mode is characterized by (i) a decrease of the D_α radiation and recycling close to the plasma boundary, (ii) the formation of a steep pedestal region close to the separatrix and (iii) the change of the radial electric field (E_r) at the edge. That leads to the formation of a edge transport barrier (ETB), with a corresponding suppression of turbulence and improvement of the confinement properties [26–29].

Due to the improvement of confinement, the H-mode is considered as the base line operating scenario for future fusion reactors. The mechanism leading to the L-H transition, however, is not yet identified and it is one of the key issues in fusion physics [30].

1.8.2 The I-phase confinement regime

In some cases, when the heating power is close to the L-H transition threshold, a regular pulsations in the low kilohertz range at the edge plasmas (the so-called limit cycle oscillations or LCOs) are observed in several devices (DIII-D [31, 32], JET [33, 34], EAST [35, 36]) before the transition to H-mode regime. This regime is called intermediate I-phase on AUG and as it is slower in comparison to fast L-H transition, it is favorable for understanding the L-H transition mechanism. For that reason, limit-cycle oscillations (LCOs) are being intensively studied in various fusion devices [35–42]. The LCOs had been typically observed in the edge radial electric field and have been associated with an interplay between turbulence, mean flows and low frequency zonal flows. The mechanism behind the LCOs is still not fully understood. At AUG, two possible mechanisms are considered: (i) a competition between a turbulence drive and an enhanced flow shearing that leads to a modulation of density fluctuation level and poloidal flow velocity [39]; (ii) a competition between ballooned transport and the pressure gradient [38].

The I-phase regime can be achieved by an increase of the heating power of the L-mode but not sufficient to reach the H-mode. Another way, used the experiments in this work, is a

constant heating power and the magnetic scan from USN towards LSN (due to the lower P_{th} in DN and LSN) causing the I-phase transition. Detailed study of the turbulence and the radial electric field properties in this regime may contribute to better understand the L-H transition mechanism.

1.9 Thesis motivation and outline

The edge plasma region, extending from the pedestal to the SOL (for $\rho \gtrapprox 0.95$), plays a key role in the performance of a tokamak fusion reactor. Over the last fifty years there has been a sustained effort to measure and understand the edge plasma turbulence. Plasma turbulence greatly enhances the transport of energy and particles, being generally the dominant form of losses in fusion experiments [43–45]. Turbulence is known to be ballooned and to be influenced by the SOL plasma parameters. The aim of this thesis is to contribute to a better understanding of turbulence, namely by studying its poloidal asymmetries taking advantage of the FM-CW reflectometry diagnostic that provides measurements at both the HFS and the LFS edge plasma with high temporal and spatial resolution. In this work, the edge plasma is studied for different magnetic configurations to assess its influence on the turbulent transport. Due to the expected ballooning character of the turbulence it is anticipated that the SOL turbulence should be particularly sensitive to the magnetic configuration. Additionally, as SOL filamentary transport was found to be strongly influenced by the divertor collisionality, the evolution of the HFS/LFS density fluctuations in different divertor detachment states is investigated in density ramp up discharges.

The following main goals are addressed in this thesis:

1. Develop a technique to estimate the density fluctuation level from the homodyne FM-CW reflectometry signal and validate the new methodology by comparison with results from other diagnostics.

2. Study of the density fluctuations and their poloidal asymmetries in different magnetic configurations.

3. Comparison of the measured radial profiles of the density fluctuations with turbulence simulations from the GEMR code.

4. Study of the edge density fluctuations in the I-phase.

5. Investigation of the influence of divertor conditions on the mid-plane density fluctuations.

The thesis is structured as follows: chapter 2 describes the plasma turbulence introduction and the state of art. Chapter 3 presents the reflectometry diagnostic principles with the description of the model used to estimate the density fluctuations. In chapter 4 the AUG tokamak, diagnostics used in this work and the typical discharges are described. The methodology developed to estimate the density fluctuation levels from reflectometry systems with homodyne and heterodyne (single-ended detection) is described in chapter 5. Chapter 6 is devoted to the study of the turbulence properties in different magnetic configurations: USN, DN and LSN. Radial profiles (covering edge and SOL plasmas) of density fluctuations at the HFS and the LFS are compared with the simulations from the turbulence code GEMR. In chapter 7 the properties of edge density fluctuations are studied in I-phase confinement regime. Chapter 8 describes the asymmetric influence of the filamentary activity in the mid-plane density fluctuations along the divertor detachment. The last chapter 9 summarizes the obtained results and presents an outlook for further investigations.

Chapter 2

Turbulence in tokamaks

"I am among those who think that science has great beauty."

— Marie Curie

Turbulence is a phenomenon observed in fluids or gas flows typically characterized by the appearance of vortices. In a plasma, turbulence causes fluctuations in the main plasma parameters, such as particles density, temperature, magnetic and electric fields, potential, etc. influencing the radial transport of particles and energy. In this chapter, plasma turbulence is introduced, the main instabilities driving turbulence and turbulent properties are discussed.

2.1 Turbulence

The basic equation to describe turbulence in incompressible neutral fluids $(\nabla \cdot u = 0)$ is the Navier-Stokes equation:

$$\rho_m(\frac{\delta \mathbf{u}}{\delta t} + (\mathbf{u} \cdot \nabla)\mathbf{u}) = -\nabla p + \nu \nabla \mathbf{u} + \mathbf{F}. \tag{2.1}$$

Here ρ_m is the mass density, u the velocity field, p the pressure, ν the viscosity of the fluid and F is additional external forces. Using the characteristic scale of the system L_0 a dimensionless equation can be obtained, where u_0 is the characteristic velocity and $t_0 = L_0/u_0$ the characteristic time. Specifying spatial and temporal derivatives as $\nabla' = L_0\nabla$ and $\delta/\delta t' = t_0 \cdot \delta/\delta t$ and neglecting additional forces **F** one can obtain:

$$\frac{\delta \mathbf{u'}}{\delta t'} + (\mathbf{u'} \cdot \nabla')\mathbf{u'}) = -\nabla' p' + \frac{1}{Re}\nabla' \mathbf{u'}, \tag{2.2}$$

where **u'** $= \mathbf{u}/u_0$, $t' = t/t_0$ and $p' = p/\rho_m u_0^2$. The Reynolds number Re is a dimensionless

constant defined as

$$Re = \frac{u_0 L_0 \rho_m}{\nu} \tag{2.3}$$

representing the balance between the kinetic energy and the viscous damping in a fluid flow, which characterizes the dynamic state of the system. Therefore, the dimensionless Navier-Stokes equation 2.2 can be used to compare systems with different characteristic scales, which can be similar dimensionally if they have the same Reynolds number (similar dynamics).

At low Reynolds number $Re << 1$, the flow is laminar with parallel velocities and a fully developed turbulence state appears at Reynolds numbers $Re >> 1$ with a superposition of different scales and directions of motions. In the real systems with high Reynolds number (that corresponds to vortices) an arbitrarily small perturbation changes radically the stability of the solution of the Navier-Stokes equation. The slightest perturbation (butterfly effect) will make the solution unstable and another solution becomes stable. The transition from a laminar flow to fully developed turbulence can not be completely described but it can be simulated under certain assumptions.

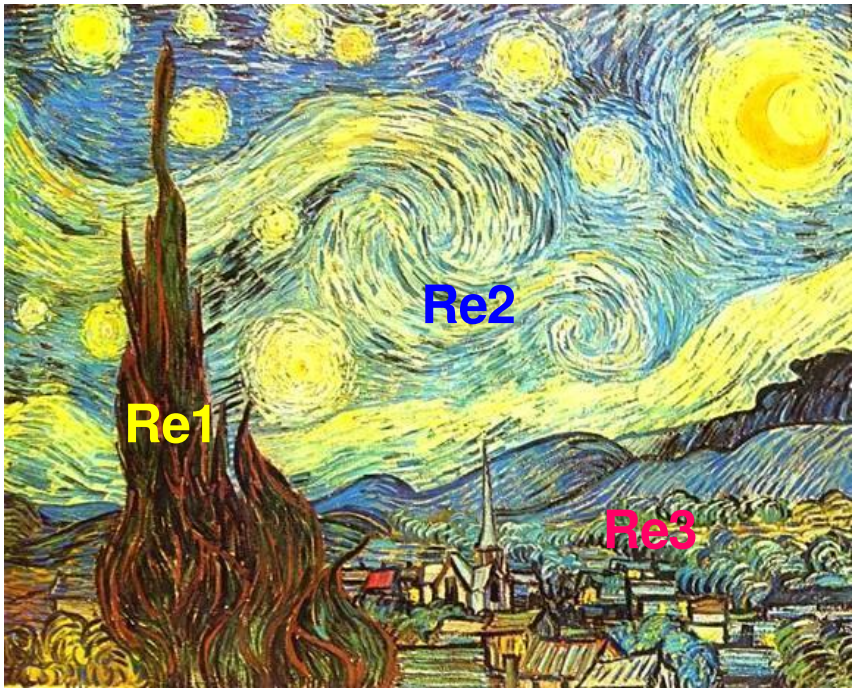

Figure 2.1: Schematic representation of flows behaviour at different Reynolds numbers $Re1 < Re2 < Re3$ (adapted from Vincent Willem van Gogh)

2.2 Turbulence spectra

Kolmogorov energy transfer between different turbulent scales has been described by a L. Richardson's poem:

> "Big whirls have little whirls
> That feed on their velocity,
> And little whirls have lesser whirls
> And so on to viscosity."

Here we suppose that the system can be characterized by the interaction of different scale vortices. Then we assume that the energy transfer between vortices at different scales depends only on the energy flux ϵ from the largest to the smallest vortices. It is also considered that the energy transfer from large scale vortices to smaller scale vortices does not dissipate to heat and is constant.

A typical turbulent system transfers energy from an injected instability towards different scales. In a system of units whose main quantities are length, mass and time (LMT) the energy flow can be expressed by a dimensional analysis as:

$$[\epsilon] = \frac{\Delta E}{t_0} = \frac{{L_0}^2}{{t_0}^3}, \tag{2.4}$$

where t_0 and L_0 are the characteristic time and size of the system.

The wave number k dimension is $1/L_0$. The basic characteristic of turbulence is the energy spectral function $W(k)$, which represents the distribution of energy in the different scales or velocities of the movement. For vortices with a particular wavenumber k (dimension $1/L_0$) the energy per unit of volume (energy density) can be expressed as:

$$W(k) = \frac{{L_0}^3}{{t_0}^2}. \tag{2.5}$$

We assume that the movement in the L_0 scale solely depends on ϵ and therefore the energy spectrum $W(k)$, the energy flow ϵ and the wave number k are linked by an equation which does not involve any other parameters. Using a dimensional analysis $W(k)$ can be given by:

$$W(k) \approx C\epsilon^x k^y, \tag{2.6}$$

where C is a dimensionless constant because the equation should remain the same for events with different scales and it should not depend on the choice of units.

Using above equations we have in terms of dimensions:

$$\frac{L_0^3}{t_0^2} = \left(\frac{{L_0}^2}{{t_0}^3}\right)^x \left(\frac{1}{L_0}\right)^y \tag{2.7}$$

with a simple system

$$L_0^3 = {L_0}^{2x} {L_0}^{-y} \tag{2.8}$$

$$t_0^2 = {t_0}^{3x}, \tag{2.9}$$

where the solution is $x = \frac{2}{3}$ and $y = -\frac{5}{3}$. Therefore we arrive to the Kolmogorov's "5/3" law:

$$W(k) \approx C\epsilon^{2/3} k^{-5/3}. \tag{2.10}$$

The above law corresponds to wavenumbers $k > k_{inj}$, where k_{inj} is the wavenumber of the driving instability. The shape of the spectrum was found to depend on the dimension. Transport in fusion devices along a magnetic field line is much faster compared to the slow drifts perpendicular to the magnetic field. Then two-dimensional (2D) turbulence can be characterized by anisotropic structures instead of isotropic three-dimensional (3D) ones. The 2D turbulence case has been described by Krainchan [46]. Two different cascades have been found: a direct cascade from the injection scale k_{inj} towards smaller structures, and an inverse cascade from the injection scale k_{inj} towards larger structures. The spectral energy per wavenumber is described as:

$$W(k) \approx k^{-5/3}, k < k_{inj} \tag{2.11}$$

$$W(k) \approx k^{-3}, k > k_{inj}. \tag{2.12}$$

The power spectrum knee point ($k = k_{inj}$) indicate the injection scale of the underlying instability. However, if several injection scales exist simultaneously (that is typically for the real plasmas) then both the spectral indexes and knee points can be influenced. Both examples of 3D and 2D turbulence spectral energy per unit wavenumber are schematically presented in Figure 2.2.

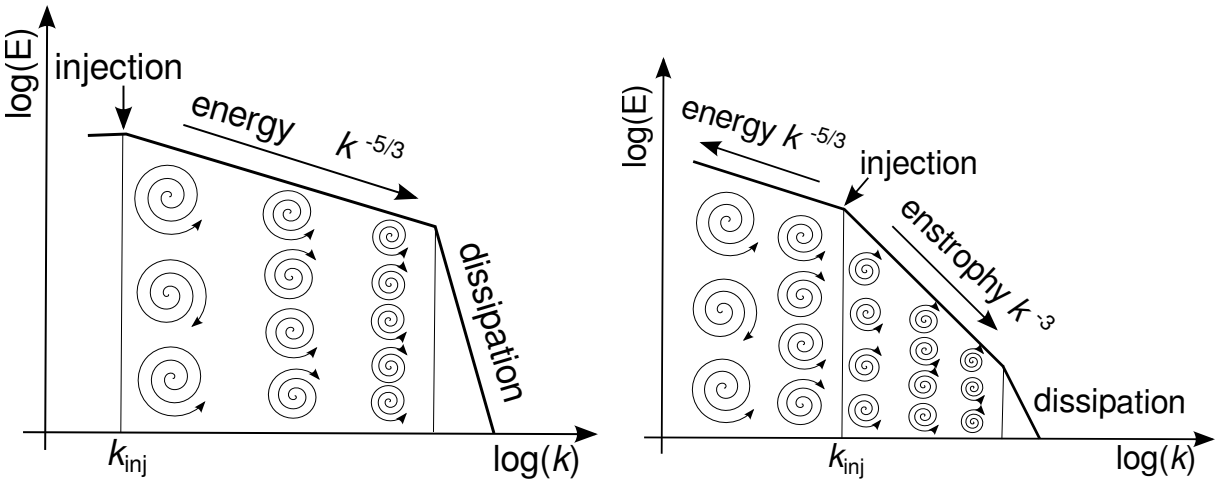

(a) 3D (b) 2D

Figure 2.2: Spectral energy for (a) 3D turbulence with direct energy cascade, (b) 2D turbulence with inverse energy and direct enstrophy cascades.

2.3 Radial transport

In fusion devices with magnetic confinement such as tokamaks, due to the transport (classical, neoclassical and turbulent), confinement properties degrade and plasma particles diffuse into the peripheral regions interacting with the surfaces enclosing the plasma. As the cross-field transport through the edge plasma strongly influences the heat and particle flux to the plasma facing components, processes of recycling, impurity influx and He ash removal have been considered. The identification and reduction of radial transport losses became a key challenge for theoretical and experimental physicists.

It has been recognized for many years that the cross-field plasma transport in the edge plasmas is dominated by turbulence. Overviews of the edge turbulence investigation [22, 43–45, 47–53] reveal the importance of measurements performed in small and medium-sized tokamaks. Plasma turbulence in the confinement region of tokamaks and stellarators seems to be responsible for the radial profiles in this region and thus co-determines the density and temperature in the core plasma. In addition, all the radial particle and heat transport must eventually be transferred across the separatrix into the SOL.

Particular attention has been paid to coherent structures in plasma turbulence. It was observed that turbulence-driven transport is convective and intermittent [50, 51, 54, 55] thus it cannot be governed only by a simple diffusive process. Intermittent transport has been characterized and its universality was confirmed across the edge plasma in different magnetic confinement devices [54–57]. Substantial theoretical and experimental evidence shows that the sheared flows play an important role in the dynamics of plasma turbulence and cross-field

transport. However, the details of the formation of these turbulent structures in the plasma edge still require clarification. For this spatially and temporally resolved data are most important but difficult to obtain due to the limitations of the available diagnostics.

2.4 Plasma instabilities driving turbulence

The assumption that the increased diffusion of plasma (caused by chaotic fluctuations in the electric field) was due to the development of plasma instabilities, was first made by D. Bohm in 1949. Since then, numerous experimental and theoretical studies of turbulence were performed in tokamaks and other magnetic confinement systems in order to describe the anomalous plasma diffusion. This task is still quite difficult, even considering that there were significant achievements in the research of hydrodynamic turbulence of ordinary liquids because in plasmas, which typically have two charged fluids (electrons and ions) interacting with each other, the electromagnetic forces play a significant role.

The plasma turbulence can be developed due to several types of instabilities. The linear instabilities are driven by gradients in density, temperature and pressure while the saturated instabilities drive broadband turbulence through non-linear coupling. In systems with magnetic confinement, turbulence properties are largely determined by the anisotropy created by the strong magnetic field present in magnetically confined fusion devices.

There are two fundamental linear instabilities (see Fig. 2.3) relevant for plasma turbulence, the interchange and the drift-wave instability. It has been shown [58, 59] that, if the dominant driving mechanism remains the same, the characteristics of the linear instabilities is also present in the state of fully developed turbulence. Plasma turbulence near the wall is associated with the presence of the pressure gradient across the magnetic field lines. An instability caused by the plasma pressure gradient is typical for the devices with magnetic confinement. This instability is caused by the movement of magnetic plasma tubes towards the position with less total energy and can be developed in the vicinity of the closed magnetic field lines [60]. Its localization is limited by the shear, which is defined by the variations in the rotational transform angle with the distance from the magnetic surfaces to the magnetic axis of the system. Zero shear corresponds to Rayleigh-Taylor instability of the fluid in a gravitation field, where it is assumed that the density increases with altitude. The role of gravity in magnetic fields is played by the curvature of the magnetic filed lines. In this model, one can expect an increased level of turbulence in regions with bad magnetic field-line curvature (when magnetic-field and pressure gradients are co-directional) that is at the LFS of the tokamak. Reduction of turbulence occurs in regions with good magnetic field-line curvature (magnetic-field and pressure gradi-

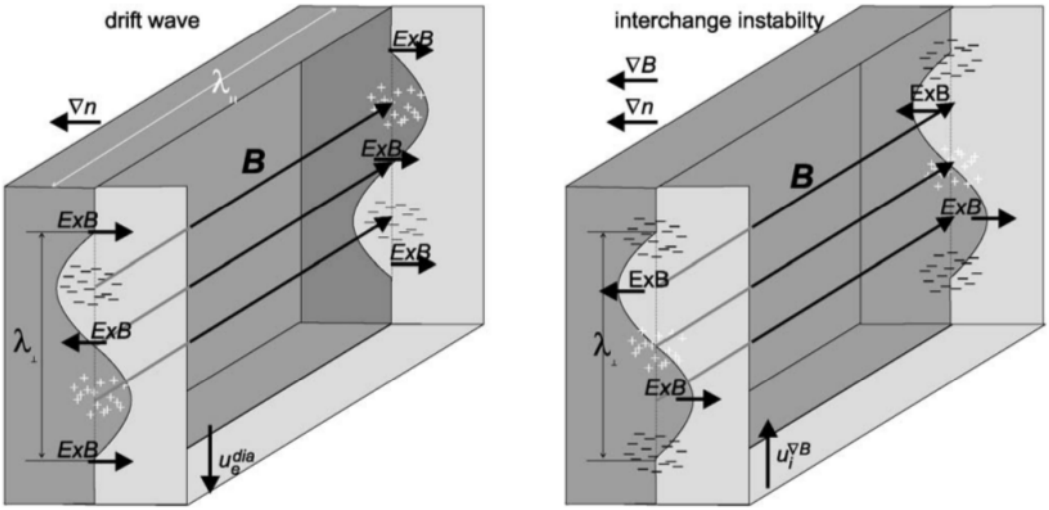

Figure 2.3: Microscopic mechanisms and properties of (left) the linear drift-wave and (right) the interchange instability (adapted from [5]. A sinusoidal line separates regions of high (left) and low plasma density. Diamagnetic, $E \times B$ and curvature drifts are indicated by arrows. In the right picture, there is a gradient of magnetic field [6].

ents are counter-directional), which happens at the HFS [60]. The schematic representation of the interchange instability mechanism is illustrated in Fig. 2.3 (right). The density perturbation is two-dimensional ($k_{\|}$ = 0) and is driven by the vertically directed and charge dependent curvature drift [6]. The cross-phase between potential and density perturbations is $\pi/2$ and the propagation in the fluctuating electric field is in the radial direction. Several instabilities are based on this mechanism such as the electron-temperature-gradient (ETG) [61], the ion-temperature-gradient (ITG) [62] and the trapped energetic particle mode (TEM) [63]. All those instabilities contribute to the transport in the plasma core.

The drift wave instability mechanism is illustrated on the left side of Figure 2.3. In this case the density perturbations are elongated along the magnetic field lines. The three-dimensional structure of the perturbations is represented by parallel and perpendicular wave numbers $k_{\|} \neq 0$ and $k_{\perp} \gg k_{\|}$, respectively. The high electron mobility parallel to the magnetic field leads to a negligible cross-phase between density and potential perturbations, so they are almost in phase. According to the drift in the electric field, propagation is in the direction of the electron-diamagnetic velocity u_e^{dia}. The drift wave becomes unstable due to the electron-ion collisions, magnetic induction or particle-wave interaction that causes a delay of the electron parallel response. In case of enhanced transport the cross-phase between density and potential perturbations increases [6]. Drift-wave turbulence is expected to make an important contribution to transport in the LFS edge of fusion plasmas [58].

Due to the different values of the cross-phase in drift-wave and interchange turbulence, its importance for turbulence suppression is also expected to be different. In the case of drift

waves, a small variation in the cross-phase between density and potential can lead to large transport changes. In interchange turbulence, the same variation would have a much weaker impact [6].

2.5 Edge/SOL turbulence and intermittent transport

Edge and SOL plasma turbulence is usually characterized by high levels of density fluctuations. As relative density fluctuation levels typically increase towards the first wall [43] and due to the boundary conditions the highest density fluctuation levels correspond to the edge/SOL plasma regions. Density fluctuations have broadband power spectra in the typical frequency range ~ 5 kHz -350 kHz.

In recent years, particular attention has been paid to intermittent coherent structures within plasma turbulence, associated with the so-called blobs and filaments [43, 45, 47, 50, 51, 54, 64–86]. Despite their small population ($< 10\%$ of the events), those coherent structures can be responsible for up to 50% of the total transport [45].

The intermittency was first discussed by E.A. Novikov and R.W. Stewart [87]. It was described as a local violation of the turbulence homogeneity, where active turbulent regions coexist with passive (quasi-laminar) ones. Intermittency is typically observed as the presence of non-periodic bursts (pulsation) with high amplitude and irregular shapes in comparison with the standard plasma fluctuations.

Those bursts can be caused by the presence of large-scale structures with high density [88]. Due to their quasi-two-dimensional structure they are usually called filaments. The cross-field particle flux is characterized by a probability distribution function, which deviates from Gaussian and exhibits very long tails. These tails correspond to strong transport events represented mainly by positive density bursts, associated with filaments or blobs [89]. According to the law of scale invariance, when some events become larger they become less frequent. This can be applied to plasma turbulence including multi-scale coherent structures.

The statistical properties of intermittent structures in the edge plasmas were found to be similar in different magnetic confinement devices [55–57, 90]. Data from small tokamaks with circular cross-section plasmas, large tokamak with divertor configuration and small linear plasma device were compared, revealing that intermittent convective transport is universal [57].

The suggested mechanism of this type of transport is the nonlinear saturation of turbulence or the presence of MHD instabilities in the edge plasma [91]. Many models and numerical simulations have been developed to describe the generation, propagation and transport properties of such plasma blobs. As an example, filaments have been modeled as poloidally localized,

coherent structures of high pressure that extend along the magnetic field lines. In this case curvature driven instabilities (interchange/ballooning) compete with the fluctuating parallel currents to give rise to a ∇B polarization [92]. The polarization causes an $E \times B$ drift which moves filaments towards the wall in the LFS SOL [93]. This blob model provides a radial transport mechanism with a radial velocity that is in agreement with experimental results. Experimental results and numerical simulations show that blobs are typically born on the LFS edge (close and inside of the separatrix) [57, 91, 94], which is in agreement with the interchange instability being dominant at the LFS edge (section 2.4).

The filaments are the dominant source of particle transport in the far SOL region [91]. Due to their movement to the wall, a significant interaction of filaments with the plasma facing components strongly influence the recycling processes. Overall, filaments reduce the effectiveness of the plasma confinement and increase thermal stress, erosion and destruction of the elements facing the tokamak plasma.

2.6 Turbulence poloidal asymmetries

Before the 90's, it was typically assumed that plasmas are toroidally and/or poloidally symmetric, however further observations in tokamak plasmas suggested that the assumption of symmetry is often violated. The existing information about poloidal asymmetries is still limited because most measurements are performed at the LFS mid-plane where diagnostic access is easier and not at the HFS where the space constrains are severe. The experimental investigation of asymmetries in the confined zone (close and inside the separatrix) is even more limited as measurements are mostly performed with the Langmuir probe diagnostics operating typically in the SOL. Strong evidence of SOL poloidal asymmetries in electron density, particle fluxes, density scrape-off length, electron temperature and floating potential was found in different tokamaks, for example ASDEX, T-10, Alcator C-Mod, JT-60, DIII-D, JET, COMPASS, ISTTOK, HYBTOK-II, MAST, EAST,etc. [53, 64–66, 86, 92, 95–107]. Typically, the measured fluctuation level of the plasma parameters at the LFS substantially exceeds the level at the HFS indicating that the turbulence drive is ballooning-like.

In the above experiments no unique interpretation is provided for the asymmetry, tentative explanations include the variations of the cross-field transport with the poloidal angle, variation of the field line connection lengths between limiting surfaces and the existence of convective flows.

An extensive experimental research was performed at Alcator C-Mod divertor tokamak [86, 97]. Significant HFS/LFS asymmetries were found at the SOL in the electron temperature and

the density profiles and also in plasma flows. Asymmetries were also found in the power spectra of the density fluctuations that are narrower at the HFS than the LFS [86]. Experimental observations at JT-60 divertor tokamak revealed the significant difference in density fluctuations levels at both the LFS and the HFS SOL and also the asymmetry of the intermittent structures observed mainly at the LFS [64, 98]. LFS/HFS asymmetries data are also available from limiter machines as T-10 and ISTTOK where a comprehensive study was done [65, 66, 96, 99]. Significant in/out asymmetries in the confined region were observed, particularly in density fluctuation properties, providing strong evidence for a poloidally asymmetric transport mechanism that induces preferential losses at the LFS. In summary, reports from different devices suggest a ballooning transport mechanism in tokamaks. Hence, lower fluctuations levels are expected at the HFS and plasma properties in the HFS SOL should depend on the magnetic configuration. The HFS region, in addition to an expected sensitivity to magnetic topology, displays specific phenomena as the formation of a high field side high density front (HFSHD)/MARFE[10, 108–110] and the existence of strong plasma flows [111]. Thus, data from the under-diagnosed HFS is essential to understand turbulence and transport.

2.7 Turbulence in different magnetic configurations

The magnetic configuration of a fusion device is defined both by the external coil system and the internal plasma current profile. For tokamaks, it is well established that the plasma shape and the magnetic shear have an impact on stability and transport. As the interchange drive plays an important role for both stability and transport, they are affected simultaneously. Information from different magnetic configurations will contribute to a better understanding of the transport asymmetries (e.g. ballooning-like transport) mainly because the connections between the LFS and the HFS are different for each magnetic configuration.

It was found for the first time on ASDEX [112] that fluctuations at the HFS are strongly reduced in the double null configuration, i.e. where there is no connection between the HFS and the LFS SOL, contrary to what happens in single null configurations. Experiments on Alcator C-Mod [97, 113] confirmed that in double- null plasmas, where the HFS/LFS SOL regions are disconnected, the HFS SOL presents turbulence levels that are substantially lower than at the LFS SOL, revealing further compelling evidence for the existence of a strong ballooning-like transport mechanism. These experimental findings are also strongly supported by simulations with the gyrofluide GEM code [114].

The effect of upper single null versus lower single null magnetic configurations on density fluctuations was studied in different machines, although limited either to the SOL (Alcator-C

Mod, ASDEX and EAST) [97, 115–118] or to the edge (DIII-D) [119] plasmas, but no global observations and an unique interpretation are provided.

Experiments on EAST reveal that the divertor asymmetry is strongly dependent on the plasma conditions and magnetic configurations. In USN higher particle and heat fluxes are observed at the upper HFS divertor target than at the LFS, in contrast to LSN, demonstrating the effect of classical drifts [116]. In DIII-D fluctuation characteristics have been found to differ substantially for the two configurations at the LFS edge of L-mode plasmas [119]. The large-scale turbulent structure distribution observed in the USN configuration is not apparent in the LSN. Also, reduced radial correlation lengths and decorrelation times are observed in LSN versus USN, suggesting that a flow shear may stabilize turbulence. The density fluctuations profile in LSN configuration exhibits a slightly higher amplitude near $r/a = 0.96$, but over most of the LFS edge profile, the amplitudes are rather similar, within the error bars. In MAST the properties of the edge turbulence in ohmic L-mode plasmas are reported to be independent of the magnetic field configuration [118]. In Alcator C-Mod low fluctuation levels are measured at the HFS SOL, similar for both USN and LSN magnetic topologies [97] while at the LFS SOL (≈ 1 cm from separatrix) density fluctuations (in ion saturation current signals) are observed to be higher in LSN than in USN. Further investigations are required to obtain a consistent picture about the poloidal asymmetries of turbulence versus magnetic configuration covering edge and SOL plasmas at both HFS/LFS.

Typically, E_r or its first derivative $\delta E_r/\delta r$ (i.e. shear) are considered important parameters for plasma turbulence stabilization (together with density and temperature gradients). The dependence of edge radial electric field profiles on the plasma shape was investigated in different devices (e.g. in ASDEX Upgrade [120]). In USN smaller absolute values of E_r compared to LSN discharges were found. This observation is supported by numerical simulations, which shows that the upper or lower divertor configurations change the parallel fluxes in the plasma SOL and edge, resulting in changes of E_r [121]. This is an important issue for understanding the L-H mode transition where the $E \times B$ shear plays a key role.

The magnetic configuration was also found to influence the L- to H-mode power threshold P_{thL-H} on many devices [122]. A larger power threshold is observed for configurations with the ion $B \times \nabla B$ drift directed away from the X-point [123–126]. The physics mechanisms behind this observation is still unknown. Some attempts to explain it has been based on neoclassical ion cross-field fluxes driven by poloidal temperature gradients in the SOL [127–129]. However, no significant differences were found in the edge ion temperature gradients in both upper and lower single null configurations. A large difference is observed in the poloidal flow velocities

in USN and LSN (favorable and unfavorable drift topologies) in DIII-D and Alcator C-Mod [119, 126, 130]. In DIII-D the local shear of the poloidal velocity at the LFS is larger for plasmas with the ion ∇B drift pointing towards the divertor X-point (LSN), which is in agreement with results in AUG. This suggests that the poloidal velocity shear may be a key parameter affecting the power threshold of the L-H transition [119, 126].

Effect of divertor detachment on the edge turbulence

As the divertor collisionality increases an enhanced cross-field transport has been reported at ASDEX tokamak at the LFS [131], leading to the formation of a density shoulder [11]. In L-mode, a change of the filamentary regime (high density transition, HDT) takes place above a density around $0.5\frac{n_c}{n_{GW}}$ (named high density transition, HDT), where n_c is the plasma core line density and n_{GW} is the Greenwald density, $n_{GW} = I_p/\pi a^2$ (I_p and a are the plasma current and minor radius) [11]. Above that critical density, the SOL density profile flattens and a "shoulder" is formed. The flattening of the SOL density profiles that was observed in many machines [50, 64, 132–134], was linked for the first time by LaBombard in C-Mod to an enhanced radial convective transport [76]. For $f_{GW} < 0.5$, the SOL displays two distinct regions, one with a steep gradient in the near SOL, followed by another with a flat gradient up to the wall. After a detailed analysis of SOL transport it was concluded [76] that in the first region parallel conduction dominates over perpendicular transport while the far SOL is dominated by perpendicular convection. Above $f_{GW} \sim 0.5$ the flat gradient region extends from the separatrix to the wall and convection dominates the whole SOL.

The enhanced filamentary transport is considered to be due to a transition from the sheath limited [93] to the inertial regime [135] of blob propagation, where the curvature drive of the blobs is balanced by the polarization current [135]. It was found that the polarization current not only modify the propagation of the plasma blobs, but also the inverse energy cascade [136], which is responsible for the self-organization of the turbulence at larger scales and lower frequencies. The link between the polarization current and both effects - blob propagation and strength of the inverse energy cascade - has been emphasized in [137].

The plasma turbulence at the SOL has also been observed to be sensitive to divertor detachment in TEXTOR [138] and DIII-D [139] tokamaks. In these studies based on density and/or potential measurements, the properties of plasma fluctuations were compared in attached and detached plasmas. In DIII-D the low frequency potential fluctuations in the vicinity of the X-point region were found to increase during detachment outside the frequency range of the $E \times B$ drift wave-like modes and to be quite different in character from broadband turbu-

lence in detached plasmas. In TEXTOR it was observed a significant increase in correlations of the turbulence in the detached state along with the suppression of high frequency density fluctuations.

2.8 Codes to interpret turbulence

In order to better understand the plasma turbulence and transport mechanisms 3D codes have been built to simulate plasma turbulence. The codes are based on a set of Braginskii-like plasma fluid equations [140] coupled with an electromagnetic model that accounts for the finite inductance in parallel Ohm's law and handles the associated magnetic field perturbations [58, 141, 142]. One of the main difficulties in the available turbulence codes is to reproduce the tokamak boundary conditions and the SOL region.

Although there are several turbulence codes available, the GEMR code has been used in this thesis due to its availability at AUG and because it takes into account the plasma boundary conditions at AUG. The GEMR code includes several instabilities such as the interchange, the drift-wave and the conducting wall instabilities in a tokamak geometry at the transition from closed to open field lines. Overall, it includes most effects that should play an important role in the SOL turbulence dynamics, such as three-dimensional, electromagnetic, finite ion temperature or finite Larmor radius and shear flow effects [136].

2.8.1 GEMR

The experimental results in this work were compared with numerical results from the 3D gyrofluid turbulence model GEMR [143]. The open field lines corresponding to the SOL are implemented by the boundary conditions via a perturbed Debye sheath current [114, 144]. The parameters of the simulation correspond to the parameters used in the experiments at the AUG separatrix position (mainly electron density n_e, electron temperature T_e and the radial electric field E_r). Although GEMR is a $\delta - f$ limited code, it allows following the gradients evolution thus demonstrating a turbulence spreading. However, the deviation from the preprogrammed background gradients must be small. The simulation is also able to provide the E_r shear flow effects, which are important for the plasma turbulence analysis [145–147].

Chapter 3

Microwave Reflectometry

> "Engineering is achieving function while avoiding failure."
>
> — Henry Petroski

Reflectometry diagnostics in fusion plasmas are based on the radar principle. A radar launches electromagnetic waves into a medium and the echo coming from a reflecting target is detected providing information about the target and its location [148–151].

For many radar applications the refractive index of the medium is constant and the distance to the target can be directly obtained from the phase shift (or the time delay) that the waves suffer while traversing the medium. In a plasma, however, the refractive index N varies along the propagation and it depends also on the wave probing frequency F. Therefore, to localize the plasma layers along the density profile, a data set of phase shifts (or equivalently group delays) of waves with different frequencies must be obtained, as explained in section 3.1.2. The density of the reflecting layers is derived from the cutoff layers where the refractive index goes to zero.

Reflectometry diagnostics are active but non perturbing systems once they carries its own low power electromagnetic waves and therefore do not depend on the ambient radiation to perform the measurements as most optical and infrared sensors do. Reflectometry diagnostics for fusion plasmas have several advantages: (i) are able to make several plasma measurements such as density profiles, fluctuations, MHD, modes, etc; (ii) require minimal access to the machine using compact and robust equipment; (iii) the probed plasma layer can be moved across the plasma radius by varying the incident frequency, so broad regions of the plasma can be probed with the same system and (iv) as the technique relies on waves that can propagate inside the plasma even in extreme conditions, reflectometry can measure from the outer edge to the core plasma. This is in contrast with Langmuir probes that can only be placed in the most

outer part of the plasma due to the very high temperatures of a fusion plasma.

Reflectometry to obtain plasma density profiles is a very demanding application because the systems must operate in fast swept frequency mode in a wide range of frequencies and the distances to be measured are within the centimeter range (corresponding to nanoseconds time delays) and the required precision is in the millimeter range. For fluctuation studies the operation is in fixed frequency but the interpretation of the plasma response can be quite complex and models must be used. For typical fusion plasmas the adequate probing frequencies lies in the microwave and millimeter wave frequency ranges covering the standard frequency bands K (18-24 GHz); Ka (24-36 GHz); Q (33-49.2 GHz); V (49-72 GHz); W (74-100 GHz) and D (110 – 170 GHz).

3.1 Wave propagation in a fusion plasma

The wave propagation in the fusion (anisotropic) plasma depends on several factors such as the plasma conditions, the wave frequency and the angle between the wave number vector and the magnetic field (B_0). Wave propagation is very sensitive to plasma fluctuations leading to refraction, diffraction (including forward and backward scattering), oscillations and/or corrugations of the reflecting layer. Due to those multiple effects the plasma response is complex and simplified models are usually employed to interpret the output signals as well as (in some cases) numerical simulations. First, we consider the wave propagation in an homogeneous plasma.

3.1.1 Wave propagation in an homogeneous magnetized plasma

Plasma refractive index

The plasma refractive index N is the ratio between the speed of light in vacuum and the phase velocity of the waves in the plasma medium. The interaction of the probing waves with the plasma can be described by the properties of the refractive index for the characteristic plasma waves (waves that maintain their polarization along the propagation path).

Cold plasma approximation

As the probing waves travel in the fusion plasma with a phase velocity v close to the speed of light and the thermal electron speed v_{th} is much smaller than v, a cold plasma approximation can be used. The cold plasma model that corresponds to neglecting the pressure term in the

equation of particle motion gives a good description of the wave propagation except for waves with extremely low phase velocity such as close to resonances.

High frequency approximation

The wave frequencies are much larger than all the ionic frequencies therefore the induced ionic motions are negligible because of their larger mass and can be disregarded. Reflectometry uses only waves propagating perpendicularly to the magnetic field so the refractive index N can be described by the high frequency approximation of the Appleton-Hartree dispersion relation for waves with $k \perp B_0$ [152]:

$$\frac{c^2k^2}{w^2} = N^2_{O,X} = 1 - \frac{2(1-X)X}{2(1-X) - Y^2 \pm Y^2} \tag{3.1}$$

with $X = \omega_p^2/\omega^2$ and $Y = \omega_c/\omega$, $\omega_p = \sqrt{\frac{n_e e^2}{\varepsilon_O m_e}}$ and $\omega_c = \frac{eB}{m_e}$ are the electron plasma frequency and electron cyclotron frequency, respectively; n_e is the electron density, m_e is the electron mass, e is the electron charge and B_o is the total magnetic field. The plus $(+)$ corresponds to the ordinary O-mode wave and the minus $(-)$ to the extraordinary X-mode waves, respectively:

$$N^2_O = 1 - X \tag{3.2}$$

$$N^2_X = 1 - \frac{X(1-X)}{1-X-Y^2} \tag{3.3}$$

From the above equations it can be seen that the O-mode refractive index depends solely on the density, while the X-mode depends both on the plasma density and the magnetic field.

O-mode and X-mode polarizations

The geometry of the O-mode and X- mode waves are represented in Figure 3.1.

For X-mode the wave electric field is perpendicular to B_0 whereas the ordinary wave is polarized along B_0 ($E \parallel B_0$). Therefore the term $v \times B$ in the Lorenz force $F = q(E + v \times B)$ equals zero and O-mode, is as seen above, not sensitive to the magnetic field.

In the following we consider only O-mode propagation because the experiments covered in this thesis only reflectometers operating in O-mode were used.

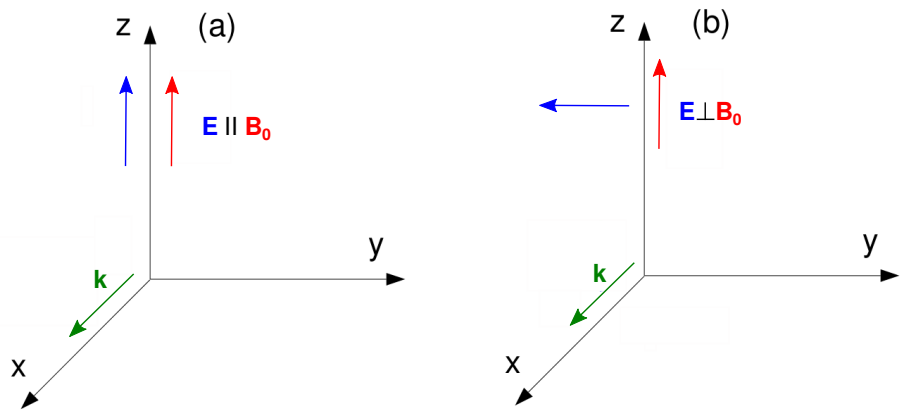

Figure 3.1: Schematic geometry of wave propagation in (a) O-mode and (b) X-mode.

3.1.2 Wave propagation and reflection in the inhomogeneous magnetized plasma

A complete description of the wave propagation in the inhomogeneous anisotropic fusion plasma would be too complicated and simplifying approximations are usually employed such as the Wentzel-Kramers-Brillouin (WKB). We also assume that the medium variations are mostly pronounced in only one direction, along the density inhomogeneity ∇n_e.

Cutoffs and resonances

$N = 0$ is the cutoff condition where wave reflection occurs. It divides the plasma propagation region from the region where the waves became evanescent. The condition $N \to \infty$ is called resonance; in the resonances the phase velocity becomes extremely low and waves can be totally or partially absorbed.

WKB approximation

In this approximation the density variations are assumed to be sufficiently slow (as compared to the wave wavelength λ) so that the plasma can be considered as a stratified medium (along the radial position r) where in each thin layer the plasma density can be considered constant. In terms of the wavelength λ it can be written as:

$$\frac{d\lambda}{dr} \ll 1. \tag{3.4}$$

The physical meaning of the WKB solution (that corresponds to the geometric optical approximation) is to neglect the secondary reflections occurring between consecutive layers and taking only the main wave that propagates along the inhomogeneous plasma until it meets the cutoff layer and reflection occurs. This is equivalent to assume that the electric field amplitude

varies slowly as compared to the wave phase.

For the propagation in the inhomogeneous plasma the Helmholtz wave equation can be written as:

$$\frac{d^2E(r,\omega)}{dr^2} + k^2(r)E(r,\omega) = 0, \tag{3.5}$$

where the wavenumber k depends on r, $k^2(r) = \frac{\omega^2}{c^2}N^2(r)$.

By applying the WKB approximation, the solution of the above wave equation for the wave electric field is:

$$E(r,t) = \frac{E_0}{\sqrt{k(r)}} exp[\pm i \int k(r)dr] exp[-i\omega t], \tag{3.6}$$

where E_0 is the electric field amplitude and $\pm \int k(r)dr$ is the electric field phase.

Wave reflection

Close to the cutoff layer an abrupt variation of the wavenumber k occurs ($k \rightarrow 0$) and the WKB solution is no longer valid. In the vicinity of the reflecting layer the solution may be obtained numerically. It can be shown [153] that in cases when the density gradient can be taken as uniform in the reflection region (this condition is not always met in the experiments) the phase shift due to plasma propagation and reflection in the plasmas at position r_a can be written as:

$$\phi = \frac{2}{c}\int_{r_c}^{r_a} (\omega^2 - {\omega_p}^2)^{1/2} dr - \frac{\pi}{2}, \tag{3.7}$$

where r_c is the cutoff position corresponding to $\omega_p = \omega$ [154].

In the above equation the term $\pi/2$ accounts for the phase shift due to the non-metallic reflection at the cutoff layer. The equation shows that the phase delay depends not only on the distance to the target but also on the refractive index $N(r)$ along all the propagation path until the reflecting layer and back to the launching region.

Localization of the reflecting layer

From equation 3.7, using an Abel inversion the distance from the launching zone (antenna mouth) at r_a to the cutoff layer r_c can be obtained as:

$$r_c(F) = r_a - \frac{c}{2\pi^2}\int_0^F \frac{d\phi/df}{\sqrt{F^2 - f^2}} df. \tag{3.8}$$

,

where F is the cutoff frequency. The above expression enables to localize each probed density plasma layer $n_e(F, r)$.

Density at the reflecting layer

According to the O-mode cutoff condition ($F = 2\pi\omega_p$) the density of the reflecting layers n_e is simply related to the wave frequency F. A practical expression can be derived from equation 3.2 as:

$$n_e[10^{18}m^{-3}] \cong \frac{F[GHz]^2}{9}. \tag{3.9}$$

3.1.3 Reflectometry in plasma with fluctuations

Bragg resonant scattering

When an incident electromagnetic wave with frequency $\omega = 2\pi F$ and wavenumber k is launched into the inhomogeneous plasma in the presence of density fluctuations characterized by wavenumber and frequency k_f,ω_f part of the wave energy is subtracted from the wave and scattered into the space. The wave energy is redistributed and the scattered wave propagates with the wave vector k_d given by:

$$\begin{aligned} k_d &= k \pm k_f \\ \omega_d &= \omega \pm \omega_f. \end{aligned} \tag{3.10}$$

The angle θ of the scattered wave follows the Bragg relation as,

$$|k_f| = 2|k|sin\frac{\theta}{2}. \tag{3.11}$$

At the location where the Bragg condition is met, the fluctuations wave number k_f is resonant and the coupling between incident wave and fluctuation is maximum. Another important process leading to perturbations of the reflected signals are the oscillations of the cutoff layer induced by plasma fluctuations. Resonant Bragg backscattering occurs along the propagation path and at the cutoff position. Experimental and numerical studies showed that due to the swelling of the wave electric field occurring close to the cutoff and the typical shape of fluctuation spectra in tokamaks (with an abrupt decay above some critical k value) the dominant part

of the reflected signal (amplitude and phase) contains mainly information about fluctuations located close to the cutoff layer [155–157].

3.2 Reflectometry systems

A reflectometry system has an emission section with microwave sources that generate the probing waves and transmission lines that carry the waves from the generators until the emission antenna that launch them into the plasma. At the reception part the waves are collected by the receiving antenna (the same antenna can be used for both emission and reception) and guided through the returning transmission line until the detection section. The transmission lines are an important part of the reflectometry system because they must carry the low power waves through long and often complicated paths with minimal losses and spurious reflections. The antennas design is critical because antennas must focus the wave energy on the plasma density layers to be probed but those layers move following the profile dynamics. The detected signals are obtained from the reflected signals and a sample of the incident probing ones. The reflectometry systems use different detection techniques namely homodyne, heterodyne single ended and heterodyne IQ detection (double ended) producing different output signals.

3.2.1 Systems with homodyne detection

The single ended homodyne detection as displayed in Figure 3.2 is the simplest detection scheme. However as the diagnostic should operate in very fast frequency mode over a wide frequency band for density profile measurements (as will be described in section 3.4) even with a simple detection the system is always a complex instrument. The microwave source produces a signal with constant amplitude A (after leveling) and fixed or linearly variable frequency F.

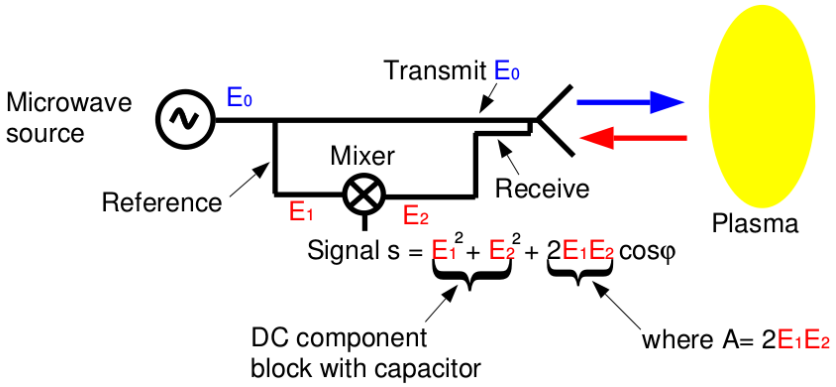

Figure 3.2: Schematic view of an homodyne reflectometer system [7].

A small part of the launched signal E_1 (that is used as a reference signal) is mixed the

reflected signal E_2 resulting in the output signal $s(t) = A(t)cos[2\pi F + \phi(t)]$. So at detection amplitude $A(t)$ and phase $\phi(t)$ components of the output signals are not separated. The phase $\phi(t)$ is determined by the distance that the waves have traveled (back and forth) in the plasma and both the phase and the amplitude are sensitive to the features of the density profile and to the plasma fluctuations.

3.2.2 Systems with heterodyne I/Q detection

The systems with heterodyne I/Q detection that provide phase $\phi(t)$ and amplitude $A(t)$ separately are used for the density fluctuation measurements that operate in fixed frequency regime, so electronics complexity and costs are still kept at reasonable levels. In this detection configuration two detectors are combined into a quadrature-phase scheme as depicted in Figure 3.3 that improves the dynamic range and the sensitivity of the diagnostic.

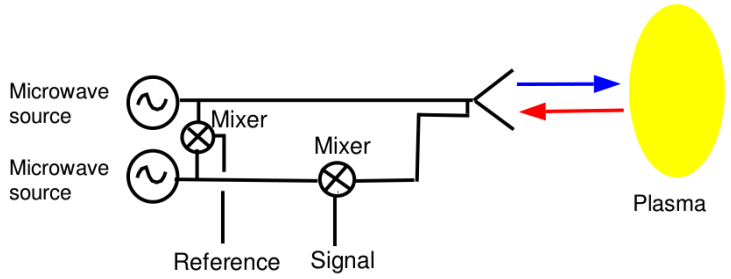

Figure 3.3: Schematic view of an heterodyne (double ended) reflectometer system [7].

The reference and the reflected signals are mixed to obtain the in-phase signal $I(t)$. An extra phase shift of $\pi/2$ is added to the reference signal and after mixing with the reflected signal, the quadrature signal $Q(t)$ is obtained. From $I(t) = A(t)cos(\phi(t))$ and $Q(t) = A(t)sin(\phi(t))$ the phase $\phi = tan^{-1}(Q/I)$ is derived.

3.2.3 Homodyne versus single ended and I/Q heterodyne detection

The homodyne system is simpler than the heterodyne scheme and is used with success for profile measurements in the lowest frequency bands (K, Ka and Q). In the higher frequency bands where the level of reflection can be lower because the reflecting plasma layers are further away from the launching antennas, homodyne detection may not be sufficient. The losses can be due both to geometrical effects and to the cumulative wave scattering caused by the plasma fluctuations. In these situations a single ended heterodyne detection offers improved sensitivity and is easily compatible with the ultra fast swept operation, avoiding an augment of the electronics complexity and much higher costs. However, for fluctuation measurements

from operation in fixed frequency, where it may be important to obtain phase directly, the I/Q heterodyne detection should be employed whenever possible. The homodyne system is simpler than the heterodyne scheme and is used with success for profile measurements in the lowest frequency bands (K, Ka and Q). In the higher frequency bands where the level of reflection can be lower because the reflecting plasma layers are further away from the launching antennas, homodyne detection may not be sufficient. The losses can be due both to geometrical effects and to the cumulative wave scattering caused by the plasma fluctuations. In these situations a single ended heterodyne detection offers improved sensitivity and is easily compatible with the ultra fast swept operation, avoiding an augment of the electronics complexity and much higher costs. However, for fluctuation measurements from operation in fixed frequency, where it may be important to obtain phase directly, the I/Q heterodyne detection should be employed whenever possible.

3.3 O-mode reflectometry diagnostics at AUG

Here we discuss the main characteristics of the O-mode reflectometry diagnostics at AUG and its measuring capabilities. In Figure 3.4 it is represented, in a toroidal section of AUG, the locations of the FFH system (at the LFS between sectors 4 and 5) and the FM-CW system at both HFS and LHS (between sectors 5 and 6).

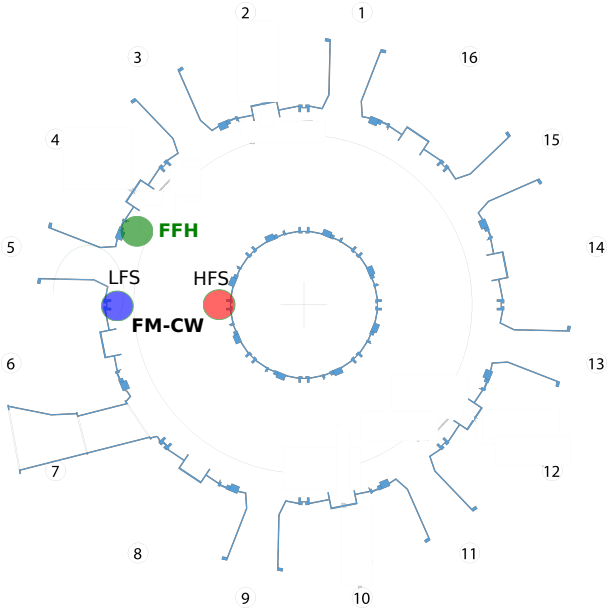

Figure 3.4: Schematic view of the FM-CW (blue and red) and FFH (green) diagnostics location in a toroidal section of AUG.

FM-CW reflectometry system

The multichannel FM-CW reflectometry system at AUG was designed (in 1990) primarily to measure density profiles at HFS/LFS at the tokamak midplane, from the SOL to the bulk plasma (depending on the plasma conditions) with both high spatial and temporal resolutions. This is a most demanding application for reflectometry systems because it requires ultra fast operation over large frequency ranges. The FM-CW system has been upgraded along the years namely a new W band (75-110 GHz) channel was added (ASilva, 1999) equipped with a single ended heterodyne detection scheme and the Q band (35-50 GHz) channel detection was changed from homodyne to single ended heterodyne. Other upgrades such as a new frequency calibration method (ASilva, 2006) enabled to improve the temporal and spatial resolutions of the profile measurements.

The system is equipped with five O-mode channels at the LFS in K (18-24 GHz); Ka (24-36 GHz); Q (33-49.2 GHz), V (49-72 GHz) and W (74-100 GHz) frequency bands and four at the HFS (in K, Ka, Q, V bands). Two additional X-mode channels are available at the LFS in the Q and V bands to probe the most outer plasma. Those two channels could not be used because they were not in operation when the experiments under this work were done.

Some of the main characteristics of the diagnostic can be seen in Figure 3.5 displaying the schematic representation of two channels of the FM-CW system (one at the LFS and the other at the HFS) in a poloidal section of AUG.

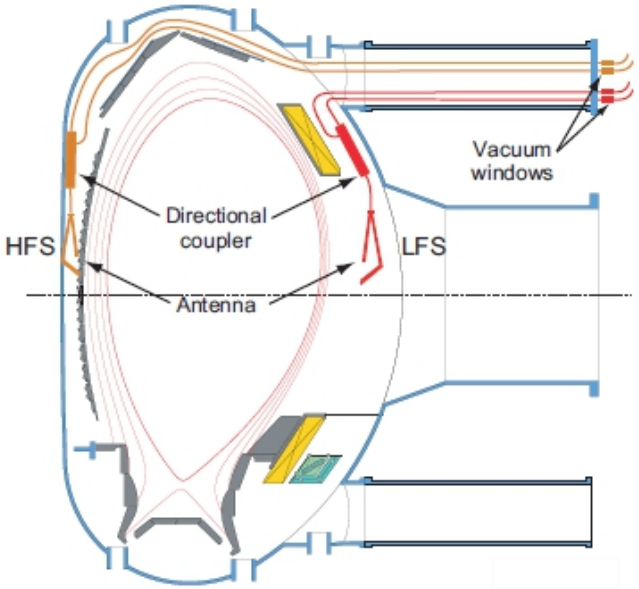

Figure 3.5: Schematic representation of the FM-CW diagnostic location in a poloidal section of AUG [8].

Each channel operates in a full standard frequency band using: (i) generators able to sweep

in frequency over the entire frequency band; (ii) in vessel transmission lines and antennas; and (iii) transmission of incident and reflected waves through fundamental metallic waveguides. All the above features contribute to minimize spurious reflections. Emission and reception of the probing waves are optimized, by using focused antennas in a monostatic arrangement (each antenna is used both for emission/reception). This also reduces the access to the machine, which is of key importance specially at the HFS where the transmission line paths are longer and more complicated due to the severe space constrains.

The detection scheme is homodyne (single ended) and compatible with the ultrafast swept frequency operation over the full frequency band. Accurate and dynamic calibrations of the whole system were performed in the lab and in the tokamak environment, to guarantee high precision measurements. From the point of view of the plasma probing, O mode waves were selected because they depend solely on the plasma density thus leading to a simpler interpretation of the reflected signals.

Measuring capabilities of the FM-CW system

Profile measurements are performed with ultra fast swept frequency operation of each channel. All channels are operated simultaneously to obtain the large set of group delay data at covered frequency range, needed for plasma density profile estimation according to equation 3.8. In this work we address the edge and SOL plasma regions so we used the K, Ka and Q channels (both at the HFS and at the LFS to study poloidal asymmetries) covering frequencies from 18 to 72 GHz, corresponding to probing densities $n_e : 0.40 - 6.43 \cdot 10^{19}$ m^{-3}. Each incident frequency F (in the GHz range) is measured with a very high accuracy (errors are typically 1-2 MHz) using dedicated delay lines (one per each frequency band) that provide a detailed dynamic frequency characteristic of the oscillators that is repetitively obtained during the system operation. An homodyne detection is used in K, Ka, Q bands and a more sensitive single ended heterodyne detection is employed for V and W bands, which probe layers further inside the plasma suffering higher losses associated with the longer propagation paths, as explained in 3.2.3.

Both detections provide output signals $s(t) = A(t)cos\phi(t)$, where A is the amplitude and ϕ is the signal phase. The swept frequency operation regime over the complete frequency band is used for density profile measurements. Individual profile measurements are taken every 1 ms (due to the limitations of the acquisition system at the time the experiments were made) in bursts of 4 frequency sweeps (25 μs sweeping time with a minimum dead time between sweeps of 10 μs which corresponds to the best time resolution of 35 μs). The density profiles require a post-processing for easier representation of the typical profile properties. Usually, the density

profiles are averaged over 10-50 profiles that corresponds to 10-50 ms time ranges. For an easier visualization of a density profile evolution, iso-density lines are considered displaying both the radial and time evolutions of the selected plasma density layers.

Besides broadband frequency operation, the FM-CW system can also operate at several fixed frequencies to measure density fluctuations at fixed density layers (determined by the incident probing frequencies). Due to its unique capability of performing HFS/LFS simultaneous measurements, the FM-CW system can measure density profiles, fluctuations and their poloidal asymmetries at SOL, edge and core plasma (depending on the plasma conditions) using combined swept and fixed frequency operation (as will be explained in chapter 5).

FFH reflectometry system

The fast frequency hopping (FFH) reflectometer is dedicated to density fluctuation measurements close to the LFS mid plane of the AUG tokamak. The system has two Q and V frequency band channels probing densities in the density range $n_e : 1.35 - 6.43 \cdot 10^{19}$ m^{-3}. Each channel/band uses a single antenna in a monostatic arrangement; the antennas are tilted poloidally to be as close as possible to perpendicular propagation. The above characteristics of the diagnostic can be seen in Figure 3.6 displaying a poloidal cross section of the tokamak with flux surfaces corresponding to a lower single null discharge.

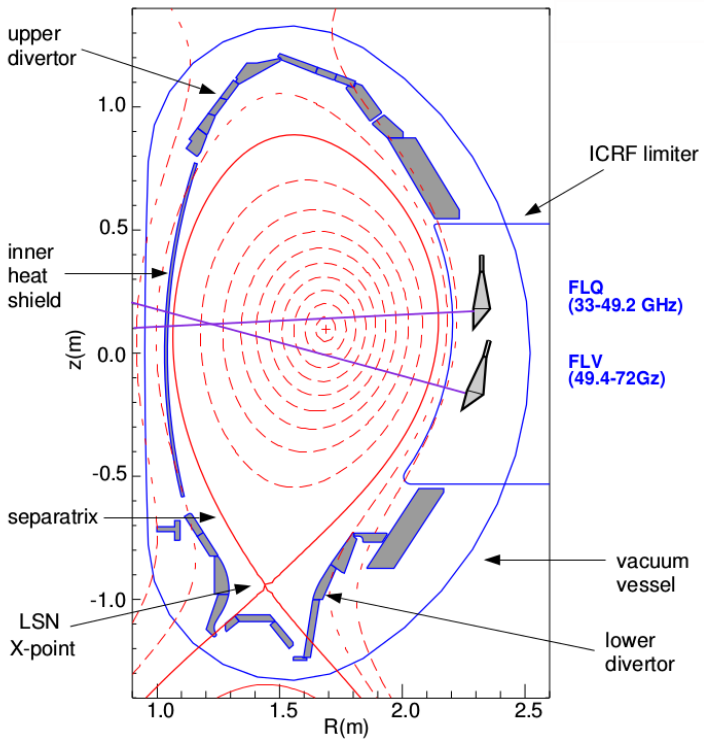

Figure 3.6: Poloidal cross-section at AUG showing position of reflectometer antennas [7].

The lines of sight show that they are aligned to be as close to perpendicular propagation in the probed edge plasma region. The FFH system is equipped with an with I-Q heterodyne detection allowing separation of the signals phase $\phi(t)$ and amplitude $A(t)$. The data acquisition system currently has a sample rate of 2 MHz. The diagnostic has a hopping frequency capability, so each channel can be pre-programmed with a selected frequency pattern allowing fluctuation measurements in several plasma regions in each discharge. Figure 3.7 displays a typical staircase frequency pattern, which is repeated continuously along the discharge.

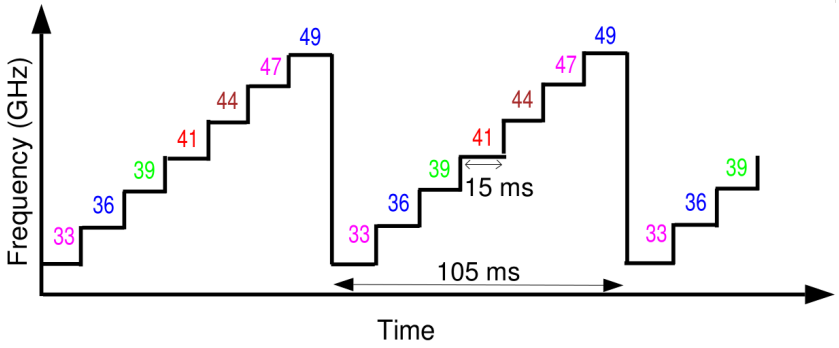

Figure 3.7: Schematic representation of the typical Q-band staircase launch frequency pattern [7].

The probe frequency is held constant typically for pre-programmed time range ($10ms < \Delta t < 8s$) and can change and lock to another frequency in≈2-3 ms.

3.4 Density profiles

With O-mode waves the density of the plasma layers, where the probing waves are reflected, can be simply determined from the probing frequencies F according to eq. 3.9, which corresponds to the O-mode cutoff condition. So, in density profile measurements, the measured quantity is the localization (r_c) of the plasma reflecting layers or equivalently the distance from the launching antenna to the plasma reflecting layers. According to equation 3.8, this requires a set of phase derivative ($d\phi/dF$) measurements from $F = 0$ up to the frequency F(GHz) that is reflected in the plasma layer to be localized. Therefore, the density profile measurement is the continuous localization of the cutoff density layers $r_c(n_c)$ along the profile.

The reflected signals are mixed at detection in a detector that can operate in the full frequency band with a sample of the launched signal, which is taken as the reference signal (see section 3.2.1) resulting in an interference signal $s(t)$ at the detector output named beat signal

that is given by:

$$s(t) = \frac{E_0(t)^2 + E_r(t)^2}{2} + E_0(t)E_r(t)cos\phi(t), \tag{3.12}$$

where $E_0(t)cos(\omega t)$ and $E_r(t)cos(\omega t + \phi)$ are the reference and the reflected signals, respectively, and $\phi(t)$ is the phase difference between the two signals.

After low pass filtering, the low frequency component of the detected signal displays a beat frequency f_b given by:

$$f_b(t) = \frac{1}{2\pi}\frac{d\phi}{dt}. \tag{3.13}$$

that can also be written as:

$$f_b(t) = \frac{1}{2\pi}\frac{d\phi}{dF}\frac{dF}{dt}. \tag{3.14}$$

The quantity $\frac{1}{2\pi}\frac{d\phi}{dF} = \tau_G$ corresponds to the so called group delay τ_G that is the delay of a group of waves (by definition a group of waves have a narrow spectrum around the main frequency). The term dF/dt is the probing frequency sweeping rate. The variation of the group delay along the entire probing frequency range can be estimated using the Abel inversion integral, and this is the key information for the density profile evaluation.

The homodyne output signals from the FM-CW reflectometry system are recorded for further digital processing which is a great advantage because data analysis is flexible and can be adapted to each target density profiles and physics studies.

3.5 Estimation of density fluctuation amplitudes

Reflectometry diagnostic is able to measure important characteristics of plasma fluctuations (such as frequency spectrum, level of fluctuation, correlation length, etc) by operating at fixed frequencies. As the waves are most sensitive to plasma fluctuations close to the cutoff layer where reflection occurs, reflectometry has the advantages of performing localized fluctuations measurements and to probe fluctuations in different plasma regions with the same system just by changing the incident frequency (thereby changing the plasma density layer where cutoff occurs).

Density perturbations can be taken into account by adding a term in the refractive index as

follows:

$$N^2 = 1 - n_e(r) + \delta n_e(r), \tag{3.15}$$

where $n_e(r)$ is the unperturbed plasma density at the cutoff layer and $\delta n_e(r)$ are the density perturbations.

Due to the refraction and diffraction (including scattering) effects, as well as oscillations of the plasma reflecting layer, the interpretation of the plasma response is complex and models must be used. For low level of fluctuations the scattering models indicate that the phase variations in the reflected signals results mainly from the Bragg scattering of the incident probing waves by density fluctuations, as discussed in section 3.1.3.

3.5.1 Models to estimate density fluctuations

For small level of density fluctuations it has been theoretically shown that the phase fluctuations of the reflectometer signal are proportional to $\delta n_e/n_e$. To estimate the fluctuation level $\delta n_e/n_e$ from the reflectometry signals, 1D or 2D models were developed. The more sophisticated 2D models [e.g. 158] may provide a more precise understanding of the turbulence properties, especially in case of large density fluctuations. However, 1D models are still often employed such as the Fanack model [155, 159, 160] due to their simplicity and ability to describe the behavior of fluctuations in spite of their limitations.

Fanack model

In fusion devices density fluctuations are typically calculated using the 1D C. Fanack model [155] by

$$\frac{\delta n_0}{n_{cr}} \approx \frac{\Delta\Phi_{max}}{C}\left(\frac{k_f/k_0}{L_n/\lambda_0}\right)^{1/2}, \tag{3.16}$$

where n_{cr} is the value of the density at the cut-off, $\Delta\Phi_{max}$ is the maximum phase shift, k_f is the wavenumber of the fluctuations, k_0 is the vacuum wavenumber, L_n is the density gradient length at the cutoff layer, λ_0 is the vacuum wavelength of the probing waves and C is a coefficient that depends on the model approximation. The equation above shows that, in order to estimate density fluctuations, it is necessary (in addition to the phase data) to obtain the local density profile gradients, which provide a factor weighting the response of the probing signals to different density gradients.

One important question behind the selection of the more adequate model is what is the dominant effect once the probing waves are affected by many different phenomena, such as

oscillations of cutoff layers, scattering, diffraction, etc. When there are no large movements of the plasma cutoff layer position, the backscattering effect is considered to be the dominant one. Also attributed mainly to scattering, are the large variations of the density fluctuations amplitude typically observed at the edge and SOL regions, which can not be solely explained by oscillations of the density cutoff layer. Consequently, in this thesis density fluctuations are calculated using the 1D C. Fanack model when the Bragg backscattering is the dominant process (in this case the coefficient C in equation 3.16 is $\pi\sqrt{2}$ [155]). The model does not cover 2D and 3D effects that are important for example when multiple reflections are present [161]. In addition, changes of the fluctuation wavenumber (see equation 3.16) that might be due to variations of the turbulence properties (for instance between the confined region and the SOL) were not taken into account. The used value for the fluctuation wavenumber is $k_f = 2$ cm^{-1}.

Numerical simulations can contribute to improve the interpretation of reflectometry measurements, in particular full-wave simulations coupled to turbulence codes will enable quantitative measurements of density fluctuations especially at high turbulence levels. An attempt to validate the 1D model for the absolute density fluctuation was done using a full-wave GYRO code simulations for fast swept reflectometry [162]. As in this thesis fixed frequency reflectometry is rather used, it is important to contrast the results obtained from the experimental data with the 1D Fanack model (which uses an approximate WKB solution) with the 2D full wave numerical simulations.

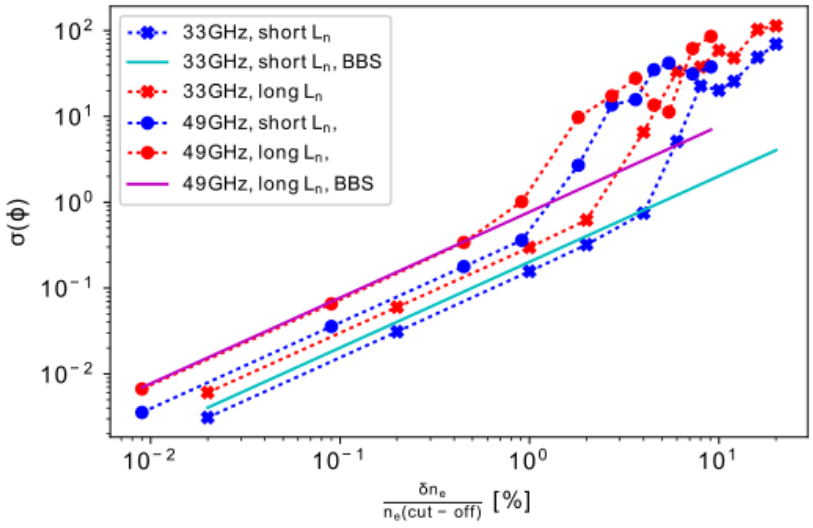

Figure 3.8: Standard deviation of reflectometry phase signals $\phi(t)$ for turbulence level scans with two probing frequencies F_p and two density gradient scale lengths L_n [9].

In Figure 3.8 it is presented a comparative analysis [9] of the standard deviation of reflectometry phase signals $\phi(t)$ for different turbulence levels. Experimental results are analyzed

the case of Bragg backscattering and fluctuations with k_f = 2 cm^{-1} (cyan and magenta lines) and numerically data was obtained using a 2D full wave REFMUL code [163] (red and blue data points). To cover different regions and density gradients, two probing frequencies were considered ($F_1 = 33$ GHz and $F_2 = 49$ GHz corresponding to cutoff densities n_{e1} = 1.35 10^{19} m^{-3} and n_{e2} = 2.98 10^{19} m^{-3}) with both short and long density gradient scale lengths L_n.

Full wave simulations show that plasma fluctuations display a linear relation to the phase deviation of reflectometry signals for lower fluctuation levels, while the relation becomes non-linear for fluctuation levels higher than 2-4%. In the part displaying a linear behavior a good agreement is observed between experimentally calculated data using the 1D Fanack model and the numerical data from the full wave code. Therefore it is expected that the 1D analysis can provide a reasonable estimation of the fluctuation levels for the linear regime.

However, to get more precise data about the density fluctuations, especially for high levels of plasma turbulence, full-wave simulations coupled to turbulence codes (including 2D and 3D effects) need to be developed.

Homodyne signal

Reflectometry systems with homodyne detection provide output signals that contains both non separable phase and amplitude components. Experimental and numerical studies [156] indicate that the homodyne signal gives a good representation of the fluctuation behavior and other properties even for high level fluctuations. This approach was considered in the thesis (see chapters 5 and 8).

Chapter 4

Experimental setup

> "Many new technologies come with a promise to change the world, but the world refuses to cooperate."
>
> — Henry Petroski

4.1 ASDEX Upgrade

ASDEX Upgrade (Axially Symmetric Divertor EXperiment) is a medium size tokamak with divertor, which operates in Garching, Germany since 1991. The work at ASDEX Upgrade is aimed to the preparation of the physics base for future fusion projects, i.e. ITER and DEMO. The vacuum chamber of ASDEX Upgrade (AUG) has a D-shape, a similar shape of the chamber is going to be used in ITER, which allows to extrapolate the obtained physical results. ASDEX was one of the first tokamaks to use a divertor concept that minimizes the impact of wall contact with a consequent decrease of an impurities amount, therefore helping to keep the plasma confinement. This improvement in plasma confinement led to the discovery of the high confinement mode (H-mode) on ASDEX [20].

The geometric parameters of AUG are: major radius is 1.65 m, minor radius is 0.5 m, with a plasma volume 14 m^3. Main parameters are presented in Table 4.1. The typical toroidal magnetic field strength is 2.5 T and a plasma current is 1 MA, however, it can be operated with magnetic fields up to 3.1 T and plasma currents up to 1.4 MA. The maximum plasma density, that can be achieved, is 1×10^{20} m^{-3}, the maximum temperature is 10 keV and the pulse duration can be up to 10 s [164].

Table 4.1: AUG parameters and operational limits

General parameters	
Major radius (R)	1.65 m
Minor radius (a)	0.50 m
Plasma volume (V)	14 m^3
Maximum average triangularity ($< \delta >$)	0.5
Max. toroidal magnetic field (B_t))	3.1 T
Max. plasma current (I_p)	1.4 MA
Max. pulse duration	10 s
Max. electron density (n_e)	1×10^{20} m^{-3}
Max. electron temperature (T_e)	10 keV
Plasma types	H, D, He
Heating systems	
Ohmic heating (POH)	1 MW
NBI heating (PNBI)	20 MW ((with D))
ECRH heating (PECRH)	4 MW (140 GHz)
ICRH heating (PICRH)	6 MW (30 MHz - 120 MHz)

4.2 Diagnostics

The aim of this thesis is to study the edge density fluctuations. It uses mainly the reflectometry diagnostics with support of several diagnostics for edge plasma characterization. The following section gives a brief overview of the diagnostics that were used.

4.2.1 Reciprocating Langmuir probes

The reciprocating Langmuir probe is used to diagnose the edge and the SOL plasmas at the AUG midplane in the LFS. The probe is inserted horizontally ≈30 cm above the midplane by the fast reciprocation, thus measuring radial profiles mainly in the SOL, the maximum stroke is $\sim$ 90$-$100 mm [11]. Different probe heads can be used with multi-pin Langmuir probes. Langmuir probes measure the ion saturation current I_{sat} or floating potential V_f with the typical acquisition rate of 2 MHz [165]. Measurements by the reciprocating Langmuir probe are taken during pre-programmed plunges, where probe moves towards the separatrix and back. Probe data from stationary phases of plunges are analyzed, which typically have a duration of $\sim$ 100$-$200 ms.

4.2.2 Doppler reflectometry

Microwave Doppler reflectometry diagnostic provides direct measurements of the radial electric field E_r profile, as well as coherent E_r fluctuations and plasma turbulence properties [166]. In contrast to conventional reflectometry, where the waves favor propagation perpendicular to the magnetic field lines, in Doppler reflectometry the launching waves have a tilt angle. Accord-

ing to a Bragg condition, diagnostic is sensitive to density perturbations with finite turbulence wavenumber $k_\perp$ that depend on the tilt angle in the reflecting layer.

The perpendicular wavenumber of the density fluctuations is determined with a ray tracing code (such as TORBEAM [166]) using experimental density profiles and equilibria.

4.2.3 Thomson scattering and ECE

Thomson scattering

Thomson scattering diagnostic measures the electron temperature and the electron density using the scattering of electromagnetic radiation from the plasma. The launched electromagnetic wave accelerates electrons and they emit radiation in all directions, so-called incoherent scattering. The radiation intensity and the Doppler width are proportional to n_e and T_e, correspondingly. The contribution of ions is neglected as the electromagnetic radiation in plasmas is mainly scattered by the light electrons [167]. At ASDEX Upgrade the Thomson scattering diagnostic uses Nd:YAG lasers [168–170]. Density and temperature profiles are measured with 16 channels system in the core plasma (spatial resolution is 25 mm) and 11 channels in the edge (spatial resolution is around 3 mm) [171].

ECE

This diagnostic is based on the electron cyclotron emission, which results from the cyclotron motion of electrons (with frequency f_ce) around magnetic field lines and provides the electron velocity distribution function [172]. Then, under suggestion that the distribution function is Maxwellian, the electron temperature can be inferred from the radiation intensity. At ASDEX Upgrade the diagnostic operates at the second harmonic extraordinary X-mode due to the high optical thickness [173]. The magnetic field and plasma density determine the resonances and cut-offs for the electron cyclotron emission. The toroidal magnetic field B_t in AUG varies in the range of $1-3$ T and the density in the range of $10^{19}-10^{20}$ m^{-3}. Under these conditions the microwave range (around 100 GHz) is the most suitable for the ECE diagnostic [174]. The radial resolution of the ECE system on AUG is up to 5 mm and the temporal resolution is 1 μs [174].

4.2.4 Lithium beam

The lithium beam is a standard diagnostic used for measurements of the edge electron density profiles. The diagnostic is based on collisional excitation of neutral lithium particles, which

are injected into the plasma [175]. The emission depends on the plasma density and can be detected by spectroscopic methods. The line of sight of the detector crosses the lithium beam at a certain angle, which allows to perform localized measurements at the edge and pedestal regions and to infer the plasma electron density profile. The IPP technique is inherently capable of deriving absolute density profiles from the relative line-radiation profile without the need for cross-calibration. [175–177].

The lithium beam diagnostic on AUG has a spatial resolution of 5 mm in the radial direction and 12 mm in the direction of the magnetic surfaces, whereas the temporal resolution is 50 μs. The diagnostic cannot measure the density continuously due to high background noise. The background level is measured and subtracted from the signal with 2 kHz frequency [178].

4.2.5 Laser interferometry

Laser interferometry measures the line average electron density n_e along a line of sight. The diagnostic is based on the phase shift that appears during the propagation of electromagnetic ordinary waves through the plasma. The O-mode wave refractive index in the plasma depends solely on electron density n_e (see chapter 3), therefore by comparing the phase shifts measured in the plasma and a vacuum paths with equal lengths, the averaged density along the line of sight can be obtained. Waves in the microwave range cannot be used to avoid refraction/reflection and also due to the high losses in the waveguides, which increase with decreasing wavelength. Therefore interferometers operate in the sub-millimetre range using far-infrared laser frequencies.

At AUG, a deuterium cyanide (DCN) laser is used, with a wavelength of 195 μm that provides a temporal resolution of 300 μs [179]. The DCN system consists of 6 laser beams (H-0 to H-5) measuring the line averaged density along six different lines of sight. In this work we use data from beams H-1 and H-5 that provides core and edge electron line average densities, respectively. The locations of H1 and H5 beam lines in poloidal section AUG are illustrated in Figure 4.1.

4.2.6 Magnetic coils and equilibrium reconstruction

The plasma equilibrium in a tokamak is estimated mainly from the magnetic flux and poloidal magnetic field measured with the magnetic diagnostics. These diagnostics consist of magnetic coils and loops of different configurations placed outside the plasma. The information on the magnetic fields derived by the coils is used as an input data for codes for reconstruction of the tokamak magnetic surfaces.

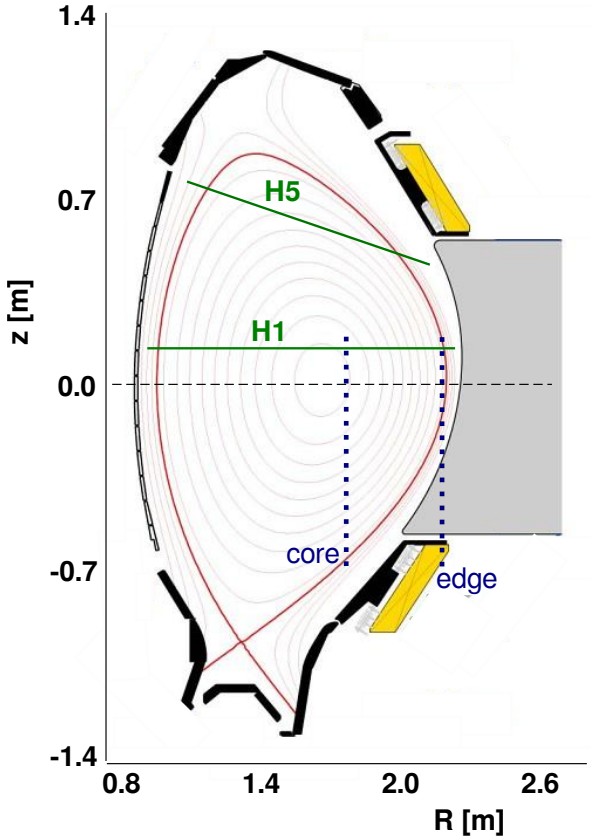

Figure 4.1: Position of the H1 and H5 beam lines in the schematic view of AUG poloidal section.

In AUG the magnetic diagnostic is a set of 32 poloidal Mirnov coils, which measure the perturbed poloidal magnetic field dB_θ and allow to determine the poloidal mode number. Also, there are 10 toroidal Mirnov coils available to obtain the toroidal mode number.

The locations of Mirnov coils in toroidal and poloidal sections of AUG are shown in Figure 4.2. MHD mode activity up to 1 MHz can be measured from the magnetic coil signals with a 2 MHz of sampling frequency during 10 s. To obtain the radial structure of MHD modes diagnostics such as ECE, soft X-rays and reflectometry are required.

For the reconstruction of the plasma equilibrium the consolidate CLISTE code (CompLete Interpretive Suite for Tokamak Equilibria) is used at AUG [180].

4.2.7 IDA

The Integrated Data Analysis (IDA) at ASDEX Upgrade, is a tool based on a forward modeling of the measured data, which provides statistical and systematic uncertainties in the measured data and in the modeling parameters [181]. The quality of the measured parameters is improved by combining data from different diagnostics. IDA is applied routinely to estimate electron density and temperature profiles using data obtained with lithium beam emission spectroscopy, laser interferometry, electron cyclotron emission and Thomson scattering spec-

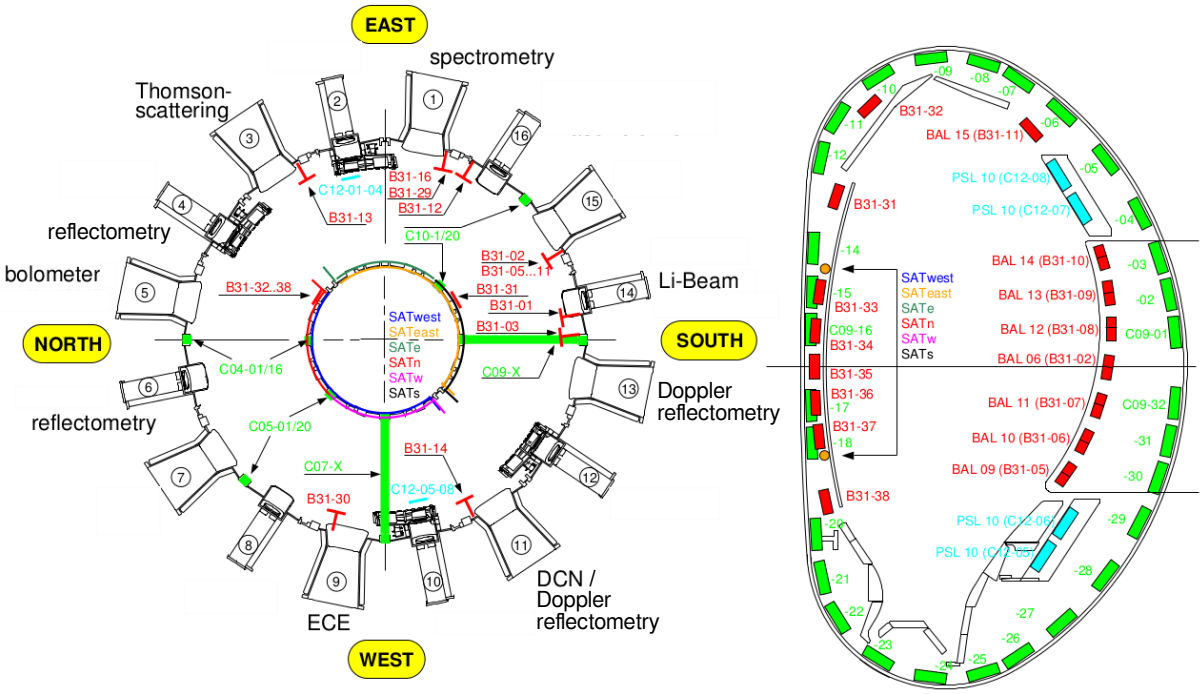

Figure 4.2: Locations of Mirnov coils and the described above diagnostics in the schematic view of AUG toroidal and poloidal sections.

troscopy. Due to its modular concept, other diagnostics can be added. Reflectometry is also included in the IDA analysis upon request.

4.3 Description of the experiment

Magnetic configuration scan

Experiments were made at AUG in USN and LSN configurations as well as in discharges with magnetic configuration scan aiming to access a DN magnetic configuration. The goal of the experiments is to study a possible influence of the magnetic configuration on the HFS/LFS turbulence asymmetries. Dedicated discharges were performed where the magnetic topology evolves from USN to LSN through DN with the main discharge parameters maintained constant. Figure 4.3 illustrates the magnetic equilibrium corresponding to the different configurations along the discharge.

In these discharges the USN phase is characterized by the confinement parameter H_{98} above 0.55 indicating I-mode confinement regime. For the study of an influence of the magnetic topology on turbulence, L-mode discharges in USN and LSN with similar confinement parameters and heating power were compared. The evolution of the main plasma parameters for discharges #31633 and #31634 with magnetic configuration scan, which have similar main

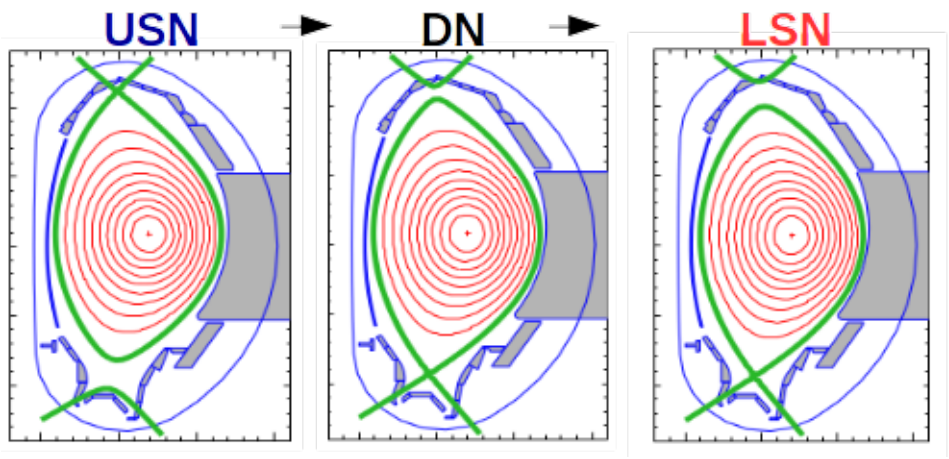

Figure 4.3: Schematic sequence of magnetic equilibria used in the experiments (discharges #31633 and #31634) - from USN through DN to LSN.

plasma parameters but slightly different evolution of the magnetic configuration is shown in Fig. 4.4. Discharges are characterized by a toroidal magnetic field of B_t = -2.5 T, a safety factor of $q_{95} \approx$ 4.7 and a plasma current of I_p = 900 kA. The electron cyclotron resonance heating (ECRH) power during the steady state part of the discharges was in the range 600 - 630 kW. The core and edge line-averaged density were $\bar{n}_e \approx 3.9 \cdot 10^{19}$ and $2.0 \cdot 10^{19}$ m^{-3}, respectively.

The magnetic configuration is indicated by the $dRXP$ parameter which is the distance between the primary and secondary separatrices that correspond to lower and upper magnetic flux surfaces, respectively (it is positive for USN and negative for LSN). A significant uncertainty is associated with the identification of the configuration mainly due to limitations of the magnetic equilibrium reconstructions. In addition, oscillations are observed in the $dRXP$ parameter near the DN configuration indicating that the DN phase is not stationary.

The confinement regime is characterized here by β_N, reveling a significant confinement enhancement (I-phase) when approaching the DN configuration and lasting in the LSN configuration. Significant ECRH power was applied during the discharge early phase (that is then reduced to a value of $\sim$600 kW) to avoid strong MHD activity that would lead to a plasma disruption. Due to the configuration dependence of the H-mode power threshold, it is challenging to maintain the discharges in L-mode for all magnetic configurations. Since the H-mode power threshold is higher for plasmas in USN [182] a transition to I-phase occurs when the magnetic configuration approaches DN, preventing a direct comparison of configurations in L-mode. Also, typically the USN phase of the discharges is clearly in I-mode while the confinement regime of the LSN phase is not always easy to determine. After the DN phase, the plasma confinement may remain in I-phase or be reduced to near L-mode values. It should be noted that the ECRH power reduction in order to prevent the transition to I-phase is not appropriate due to the

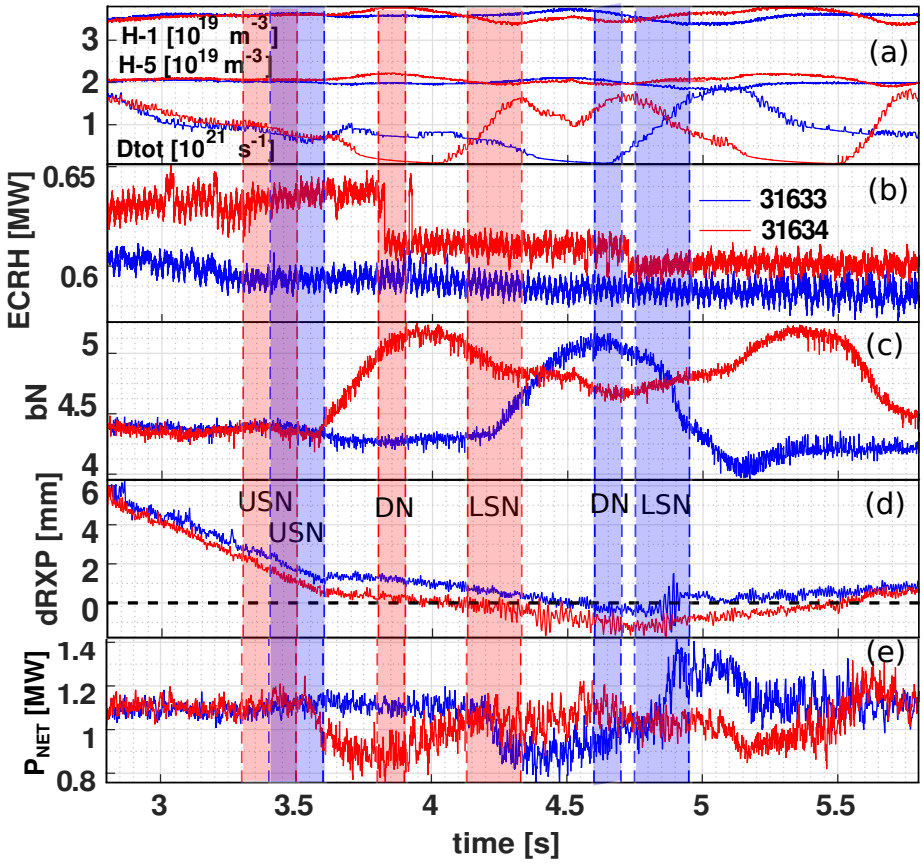

Figure 4.4: Temporal evolution of the main plasma parameters for discharges #31633 (blue) and #31634 (red): (a) core (H_1) and edge (H_5) line-averaged density, D_2 fuelling rate; (b) ECRH power; (c) beta normalized; (d) magnetic configuration parameter $dRXP = \Delta XP/[B_{pol} * 2\pi * R_{aus}]$, where ΔXP is the flux difference between upper and lower plasma surfaces, R_{aus} radial coordinate of the outermost point of the plasma surface and B_{pol} is poloidal magnetic field at R_{aus}; (e) Netto power P_{NET} = total input power $- dW/dt$, which is considered as power loss. Vertical dashed lines indicate time ranges used for the comparison of different magnetic configurations: USN, DN and LSN.

discharge disruption.

As described above, it is not possible to compare the three magnetic configurations in the same confinement regime. To overcome this limitation the USN L-mode discharge was compared with a standard LSN L-mode discharge. For the I-phase, the comparison is performed between data from DN and LSN magnetic configurations obtained in the multi-configuration discharge.

The L-H power threshold is usually defined as $P_{LH} = P_{ohm} + P_{heat} - dW/dt$, where P_{ohm} is the ohmic power, P_{heat} is the heating power and dW/dt is the rate of change of the stored plasma energy. The net power through the separatrix is also shown in Fig. 4.4, with a value around 1.1 MW observed for the USN part of the discharge that is then reduced to about 0.9 MW during the I-phase due to the confinement enhancement. For AUG, the power threshold

at density of $4 \cdot 10^{19}$m^{-3} was found to be in the range 1.1 to 1.4 MW for LSN discharges [25], meaning that the discharge being studied should be marginally in L-mode for the LSN phase as observed. Note that the power threshold to achieve the I-phase is slightly below the value required for the L-H transition. The evolution of the confinement regime during the discharge confirms previous observation that the power threshold is larger for USN than LSN and even lower for DN configuration (below 0.9 MW).

Reflectometry diagnostic parameters

Density fluctuations were estimated in this thesis using the Frequency Modulation - Continuous Wave (FM-CW) system operated in fixed frequency (FF) mode. The detailed information about diagnostic and data analysis is in chapters 3 and 5, correspondingly. The probing frequencies used in this study for each frequency band and the corresponding probed density layers are indicated for the analyzed discharges in Table 4.2.

Table 4.2: Probing frequencies and respective cut-off density values

Discharge, #	Band	K	Ka	Q	V
31633	F[kHz]	18	28	36	-
31634 USN-DN-LSN	$n_e[10^{19}$ m$^{-3}]$	0.40	0.97	1.61	-
33631 LSN	F[kHz]	24	35	40	52
	$n_e[10^{19}$ m$^{-3}]$	0.70	1.52	1.98	3.35
33484 LSN	F[kHz]	18	26	36	52
33547 USN	$n_e[10^{19}$ m$^{-3}]$	0.40	0.84	1.61	3.35

Density ramp-up discharges with divertor detachment

Density ramp-up discharges were performed in a standard LSN magnetic configuration with the ion ∇B drift towards the X-point by increasing the deuterium gas injected while maintaining constant levels of additional heating power. The evolution of the plasma parameters measured in the divertor and SOL regions during a typical density ramp-up discharge is shown in Figure 4.5. A rate of the density ramp-up varies along the discharge, slowing down around 2.7$-$3.4 s. During the faster ramp in the beginning and the end of the discharge the dn_e/dt rate is $\approx 2 \cdot 10^{19}$ m$^{-3}/s$. As the density is continuously increased along the discharge a rough correspondence between time and density may be used. Indicated by color are the different divertor states as they have been described in detail in [10]. At low densities the plasma is in the attached state (AS). As the inner divertor detaches the plasma is in the onset state (OS) [$t \approx$ 2.1$-$2.4 s]. Then low frequency oscillations occur at the X-point, this is called the fluctuating state (FS) [$t \approx$ 2.4$-$3.0 s]. Finally, for $t >$ 3.0 s the transition to the complete detachment state

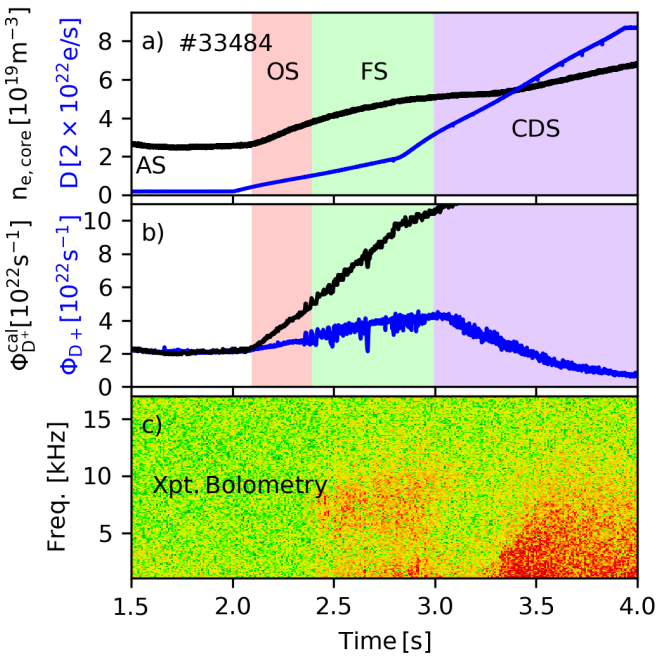

Figure 4.5: Temporal evolution of the main plasma parameters for discharge #33484: (a) core line-averaged density (black), D_2 fuelling rate (blue); (b) ion flux to the inner divertor measured by the divertor probes Φ_{D_+} (blue) and the calculated ion flux assuming a scaling with the square of the line-integrated plasma density $\Phi_{D_+}^{cal}$ (black) [10]; (c) spectrogram of the line-integrated radiated power measured by an AXUV diode (above the X-point). The different detachment states are indicated by the color blocks.

(CDS) happens when the quasi-coherent radiative X-point fluctuations disappear and also the outer divertor starts to detach from the strike-line regions. The CDS is not meant to describe the quality of detachment, which is often also described by partially or complete detachment.

The magnetic parameters were kept constant: toroidal magnetic field of B_t = -2.5 T, safety factor of $q_{95} \approx 4$, plasma current of I_p = 800 kA and ECRH power of 400 kW. The core and edge line-averaged density are ramped-up during the discharge in a range of $\bar{n}_e = 2.7-7.2$ and $1.5-4.4 \times 10^{19}$ m^{-3}, respectively.

Reflectometry diagnostic parameters

Density fluctuations were measured with a FM-CW O-mode reflectometry diagnostic operating at fixed frequency. This study is based on measurements covering mainly the plasma SOL, at six probed densities in K-, Ka- and Q-bands, three at the LFS and three at the HFS, as indicated in Table 4.3. The FM-CW system was also operated in swept frequency mode in paired discharges to obtain density profiles at both the HFS and the LFS enabling to localize the layers where fluctuations are measured along the discharge.

Table 4.3: Probing frequencies and respective cut-off densities.

Frequency bands (HFS/LFS)	K	Ka	Q
F [GHz]	18	26	36
$n_e[10^{19}$ m$^{-3}]$	0.40	0.84	1.61

Definition of the edge and SOL regions

Further on, in this work for separation and comparison of plasma turbulence properties inside and outside the separatrix, the term "edge" will be used only for confined edge plasmas inside the separatrix, and term "SOL" by the definition for plasmas outside the separatrix.

Chapter 5

Methodology for estimation of the density fluctuation level from homodyne FM-CW reflectometry

> "Never do anything complicated when something simple will serve as well. It's one of the most important secrets of living."
>
> — Erich Maria Remarque, The Black Obelisk

In this chapter it is described the methodology used to obtain quantitative information about the plasma density fluctuations, $\delta n_e/n_e$, from the frequency modulated-continuous wave (FM-CW) system, which does not provide the underlying phase data directly. The fast frequency hopping (FFH) system that gives the phase directly is also employed to validate the $\delta n_e/n_e$ data from the FM-CW system.

The estimation of the plasma density fluctuation level from reflectometry is challenging (using either FFH and FM-CW systems) because the probing waves are very sensitive to the plasma fluctuations especially at the cut off region where reflection occurs. This localized higher sensitivity is due the swelling of the electric field associated with the abrupt decrease of the wave number at cutoff layer [150], is beneficial because it improves the spatial resolution of the fluctuation measurements. But on the other hand, it makes the plasma response quite complex as the waves suffer from several effects due to the plasma fluctuations, namely scattering, refraction and diffraction. For this reason, to estimate plasma fluctuations from the corresponding perturbations in the reflected signals, models are usually required. Here we use

due to its simplicity, the 1D Fanack model and describe its advantages and limitations.

5.1 Data analysis for fast frequency hopping reflectometer

The fast frequency hopping system has two channels in the Q and V frequency bands that can operate either in fixed frequency or in frequency steps (frequency hopping) with variable pre-programmed frequencies and step durations. The system is equipped with heterodyne detection providing in-phase and quadrature (IQ) signals thus allowing phase (ϕ) and (A) amplitude to be obtained directly, as described in section 3.3.

The signals at the output are:

$$I(t) = I_0 + A(t)cos(\phi(t)) \tag{5.1}$$

$$Q(t) = Q_0 + (A(t) + \delta A')sin(\phi(t) + \delta\phi'). \tag{5.2}$$

Some corrections must be applied to the I and Q signals (equations 5.1 and 5.2), in order to remove direct current (DC) offsets (I_0 and Q_0), phase deviations ($\delta\phi'$) and amplitude imbalances ($\delta A'$), etc. [183]. For fixed frequency operation or hopping mode with short steps of the probing frequency ($\approx$ 10-20 ms), the DC offsets are measured for each discharge (at the different probing frequencies), during the current ramp-up phase of the discharge when no significant reflection from the plasma is obtained. For long frequency steps ($>$ 20 ms) the above procedure cannot be implemented due to the limited time range of current ramp-up phase and the offsets are estimated at the time where measurements for each probing frequency are performed. The presence of phase deviations $\delta\phi'$ and amplitude imbalance $\delta A'$ are clearly seen in a non-centered polar representation of I and Q signals. The imbalances are measured previously in the experiments in the laboratory, typical values are $\delta\phi' \approx \frac{\pi}{2}$ and $\delta A' \approx 1$ [7].

Data points from reflectometry are expected to describe a circle with center in the origin and radius proportional to the maximum amplitude that can be reflected to the receiving antenna. As illustrated in Figures 5.1 - 5.2, the I/Q plots correspond to a circular shape but often the center is shifted from the origin. This means that I and Q signals have offsets which are caused by electronic hardware that must be removed before retrieving the amplitude and phase. A simple method for determining the offsets was used by computing the average value of the minimum and maximum I and Q values (respectively below and above a certain threshold).

Figure 5.1 displays an example of the IQ correction of signals from the hopping Q band channel measured in discharge #33547. Measurements were obtained during time interval t:

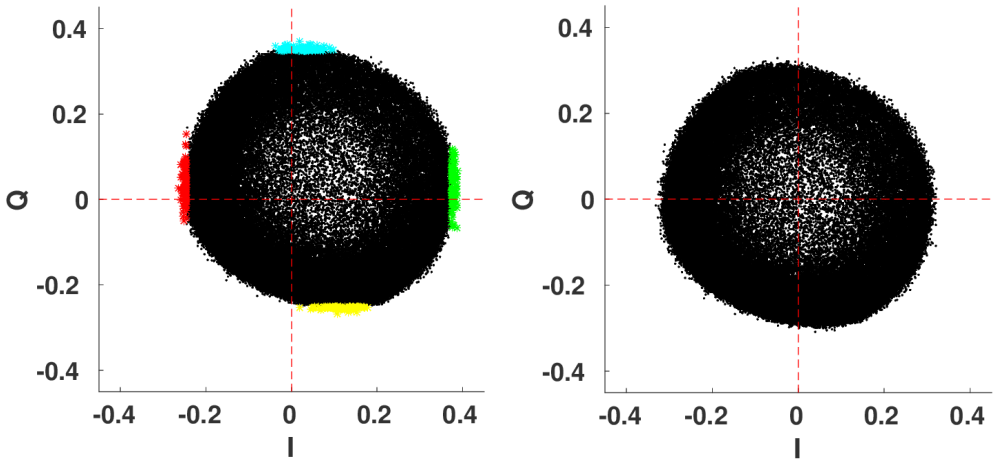

(a) initial data (b) corrected

Figure 5.1: Example #1 of FFH reflectometer signal correction for Q band signal, measured in discharge #33547 with F = 38 GHz for t = 3.21-3.29 s: (a) initial IQ data and (b) corrected signal.

3.21−3.29 s with incident frequency F = 38 GHz, probing the density layer $n_e = 1.8 \cdot 10^{19}$ m^{-3} located at $\rho_{pol} \approx 0.97 - 0.99$. This case corresponds to a favorable situation where most IQ data points lay in a circle displaying the complete circumference.

A shift of the circumference center can be clearly seen in both the I and Q axis Fig. 5.1a). Using an approximation for the farthest points (presented in colors in Fig. 5.1a) the shifts could be easily estimated and corrected resulting in the centered circumference shown in Fig. 5.1b.

In the second example presented in Figure 5.2, the experimental results were obtained for t: 3.11−3.19 s with incident frequency F = 52 GHz, probing the density layer n = 3.3·10^{19} m^{-3} located at $\rho_{pol} \approx 0.87 - 0.97$. This example corresponds to a less favorable situation where fluctuations are low and the IQ signals do not display the full circumference. However, the circumference parameters can still be obtained as at least $\pi/2$ arc of circumference can be identified.

The circumference parameters are extracted using an approximation for the farthest data points, the circumference radius is estimated and the IQ signals after shift removal were obtained as shown in Fig. 5.2b.

It should be noted that many data points are located at the edge of the circle indicating a strong reflection but a significant number is also spread inside the circumference of maximum amplitude displaying low amplitude, as presented in Fig. 5.2. This usually occurs when the cutoff layers are located further inside the plasma due to scattering of the probing waves away from the receiving antenna thus decreasing the signal to noise ratio.

Offset values are mainly due to the electronics and they are different for each probing fre-

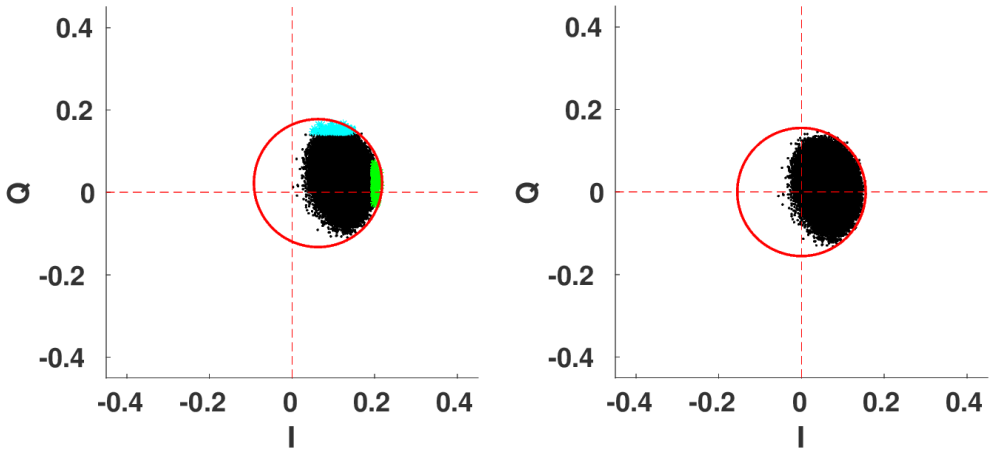

(a) initial data (b) corrected

Figure 5.2: Example #3 of FFH reflectometer signal correction for V band signal measured in discharge #33547 with F = 52 GHz for t = 3.11-3.19 s: (a) output IQ data and (b) corrected signal.

quency. As they stay approximately constant along the discharge and varies only slightly from discharge to discharge, it is possible to use the I_0 & Q_0 offset values measured without plasma to correct the IQ plots. The correction is fine tuned by fitting a circle to the extrema points. After the offsets removal, amplitude A and phase ϕ of complex signal $S(t) = A(t)e^{-i\phi(t)}$ can be obtained directly as:

$$A(t) = \sqrt{(I^2 + Q^2)} \tag{5.3}$$

$$\phi(t) = tan^{-1}(Q(t)/I(t)) \tag{5.4}$$

5.2 Data analysis for the FM-CW reflectometer

The FM-CW system is equipped with an homodyne receiver thus providing only the I signal, $I(t) = A(t)cos(\phi(t))$, thereby preventing to obtain the phase directly [184]. Since the reflected signal can be described as a sum of co-sinusoids, the missing quadrature signal can be estimated using a linear operator of $\pi/2$ phase rotation for each frequency component. This task can be accomplished by the Hilbert transform (HT) technique, which can be implemented using simple operations (in combination with the Fourier transform) as will be described in the next section.

5.2.1 Hilbert transform technique

The Hilbert transform is an important technique in signal processing, especially used in the telecommunications area. With the HT it is possible to derive the analytic function of any real valued function that comprises the original function and its Hilbert transform, thereby extending a real signal $u(t)$ into the complex plane in such way that it satisfies the Cauchy Riemann equations (being differentiable at every point of the $\mathbb{C}$ domain).

Analytic function and signal

In complex variables, a function is analytic at a point $z_0 \in \mathbb{C}$ if it is infinitely differentiable in a neighborhood of z_0 [185]. This implies that an analytic function is infinitely differentiable at any point in time and is given by the same Taylor series. The Taylor series expansion of the analytic function $f(x)$ around a is:

$$f(x) = \sum_{n=0}^{\infty} \frac{f^{(n)}(a)\,(x-a)^n}{n!}. \tag{5.5}$$

An analytic function along one of the axes has the corresponding analytic signal (here is the real axis):

$$f(x) = u(x,0) + i \times v(x,0) = cos(x) + i \cdot sin(x). \tag{5.6}$$

Analytic signals have one-sided Fourier transforms (no negative-frequency components) and its imaginary part is the Hilbert transform of the real part. Therefore any analytic signal can be written in the form:

$$s(t) = u(t) + i \cdot H[u(t)] = u(t) + i \cdot \hat{u}(t). \tag{5.7}$$

Hilbert transform

So for a real signal $u(t)$, its Hilbert transform $v(t)$ is:

$$v(t) = H[u(t)] = \frac{1}{\pi} P \int_{-\infty}^{\infty} \frac{u(\tau)}{t-\tau} d\tau = \frac{1}{\pi} P \int_{-\infty}^{\infty} \frac{u(t-\tau)}{\tau} d\tau, \tag{5.8}$$

where P is the Cauchy principal value. The Hilbert transform cannot be calculated as an ordinary improper integral due to the pole at τ = t. However, the Cauchy principal value expands the class of functions for which the integral exists. The definition of this integral can be found in [186]. Since the integration is the linear operation, the Hilbert transform is also a linear operator.

In signal processing the Fourier transform is used to get the imaginary part in frequency

space ω from the real signal $s(\omega)$ measured directly. The imaginary part is given by $-i \cdot sgn(\omega)s(\omega)$, where sgn is the signum function that extracts the sign of a real part:

$$sgn(\omega) = \begin{cases} 1 & \text{if } \omega > 0 \\ 0 & \text{if } \omega = 0 \\ -1 & \text{if } \omega < 0. \end{cases} \tag{5.9}$$

As the inverse Fourier transform of $-i \cdot sgn(\omega)$ equals $1/(\pi\omega)$, a convolution between it and $s(\omega)$ gives $s(\omega) * 1/(\pi\omega) = H(s(\omega))$, which is the Hilbert transform [187]. Hence the multiplier of Hilbert transform is $\sigma H(\omega) = -i \cdot sgn(\omega)$, using the Euler's formula:

$$\sigma H(\omega) = \begin{cases} -i = e^{-\frac{i\pi}{2}} & \text{if } \omega > 0 \\ 0 & \text{if } \omega = 0 \\ i = e^{+\frac{i\pi}{2}} & \text{if } \omega < 0. \end{cases} \tag{5.10}$$

Therefore, Hilbert transform shifts the phase of the negative frequency components of signal by $+\pi/2$ and the phase of the positive frequency components by $-\pi/2$. This means that any function that can be expanded into a sum of sinusoids, can be easily Hilbert transformed.

5.2.2 Applicability of the Hilbert transform to reflectometry signals

The Hilbert Transform technique has been widely applied in areas (for example telecommunications) where the signals are deterministic. In the case of the signals reflected from a fusion plasma these cannot be simply described to any reasonable accuracy by explicit mathematical relationships. Experimental data is usually described as being either deterministic or random but in practice no reflectometry data can be considered fully deterministic since there is always a random component in the signal, for instance due to noise.

The decision about physical data being more deterministic or random is usually based upon the ability to reproduce the data. Although in our experiments the statistical properties of the data can be repeated with identical results (for instance the probability density function can be reproduced within the limits of the experimental error), the time series are not reproduced and therefore signals cannot be considered deterministic.

The standard condition for the application of the Hilbert transform is that the frequency spectra of phase and amplitude signals are disjoint (do not have the same power at each time and frequency point) [188]. This guarantees that the Hilbert transform of a signal $s(t) = a(t)cos\phi(t)$ gives $a(t)sin\phi(t)$. In Figure 5.3 it is shown typical power spectra of phase, amplitude and I com-

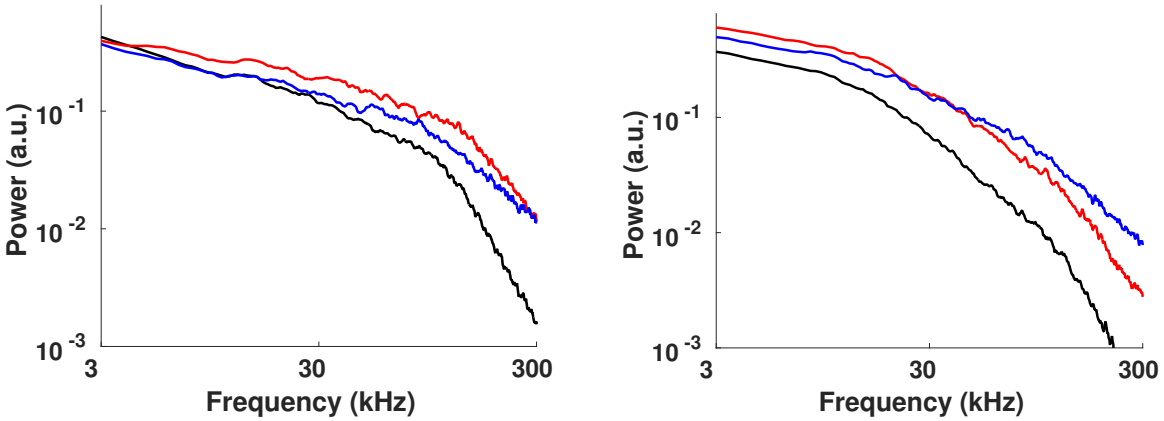

(a) $t : 2.5 - 2.6$ s
$\rho \approx 0.99$

(b) $t : 3.5 - 3.6$ s
$\rho \approx 1.01$

Figure 5.3: Power spectra of Q band I signal component (black), phase (blue) and amplitude (red) by FFH reflectometer at different time ranges and ρ_{pol} locations, discharge #33484.

ponent of the reflectometry signals obtained with the FFH system in L-mode discharge #33484, for two time ranges where probed density layers are respectively inside and outside the separatrix. As seen in the figure, the power spectra corresponding to the phase and amplitude of the reflectometry signals typically overlap in most of the frequency range and therefore it might be a limitation for the application of the Hilbert transform.

However, it is reasonable to assume that the condition of disjoint power spectra between amplitude and phase signals may be replaced by a condition of low coherence between the amplitude and phase signals as this implies that signals are at least partially independent. As it was found that the coherence between the reflectometry phase and amplitude signals is very small for all frequencies (see Figure 5.4), it is plausible to expect that the Hilbert transform can be applied to the reflectometry signals. The experimental results presented in section 5.4 provide a strong support for the above assumption.

In addition, the applicability of the Hilbert transform, also requires that the amplitude of the signal does not vary much during the time of analysis. This condition may not be fulfilled for example for the highest level of fluctuations as they impact on the amplitude of the reflected signals [156].

5.3 Phase evaluation

With the application of the Hilbert transform, the phase of the FM-CW reflectometry signal is evaluated from:

$$\phi(t) = tan^{-1}(\hat{u}(t)/u(t)), \tag{5.11}$$

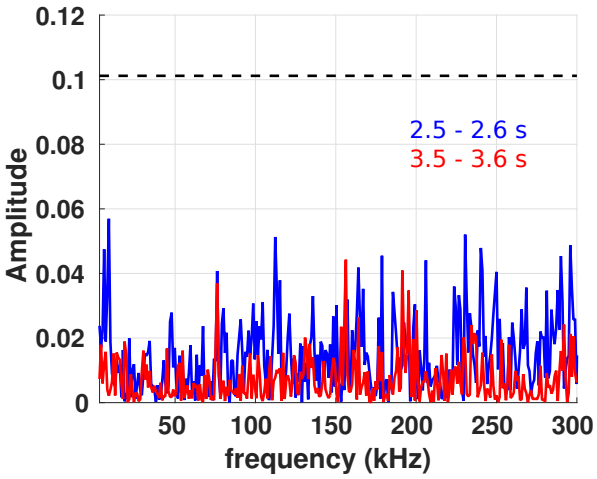

Figure 5.4: Cross-coherence between phase and amplitude of Q-band LFS signal by FFH reflectometer at different time ranges and ρ_{pol} locations - (red) $t : 2.5 - 2.6s, \rho_{pol} \approx 0.99$ and (blue) $t : 3.5 - 3.6s, \rho_{pol} \approx 1.01$, discharge #33484. Dashed line corresponds to the significance level.

where $u(t) = A(t)cos(\phi(t))$ is the output FM-CW reflectometry signal and $\hat{u}(t)$ is derived from the analytic signal $s(t) = u(t) + i \cdot \hat{u}(t)$ obtained by the application of the Hilbert transform technique.

In the case of the FFH system the phase ϕ is calculated directly using equation 5.4.

Once the phase is defined in the interval [-π, π], the phases from both systems need to be unwrapped. For this, we consider the Seo algorithm [189] which is given by:

$$\Delta\phi_{i+1} = 2sin^{-1}\frac{x_i y_{i+1} - y_i x_{i+1}}{\sqrt{(x_i + x_{i+1})^2 + (y_i + y_{i+1})^2}} \tag{5.12}$$

$$\phi_j = \sum_{1}^{j} \Delta\phi_i, \tag{5.13}$$

where x_i and x_{i+1} are the normalized real part of the complex signal corresponding to two consecutive measurements and y_i and y_{i+1} are the normalized imaginary parts of the complex signal. The relative phase difference between (x_i, y_i) and (x_{i+1}, y_{i+1}) is $\Delta\phi_{i+1}$ and ϕ_j is the absolute phase. Successive accumulation of the relative phase differences between two time points provides the absolute unwrapped phase. This method is valid providing that the phase variation between successive measurements is within $\pm\pi$.

[1]

[1] A similar algorithm is employed in the Matlab function unwrap used here.

5.3.1 Removal of phase runaway

The wrapped phase (derived either from the FFH or the FM-CW systems) is characterized by phase jumps that cannot be related to plasma density fluctuations as depicted in Figure 5.5 where typical time traces of wrapped (a) and unwrapped (b) phase signals are depicted.

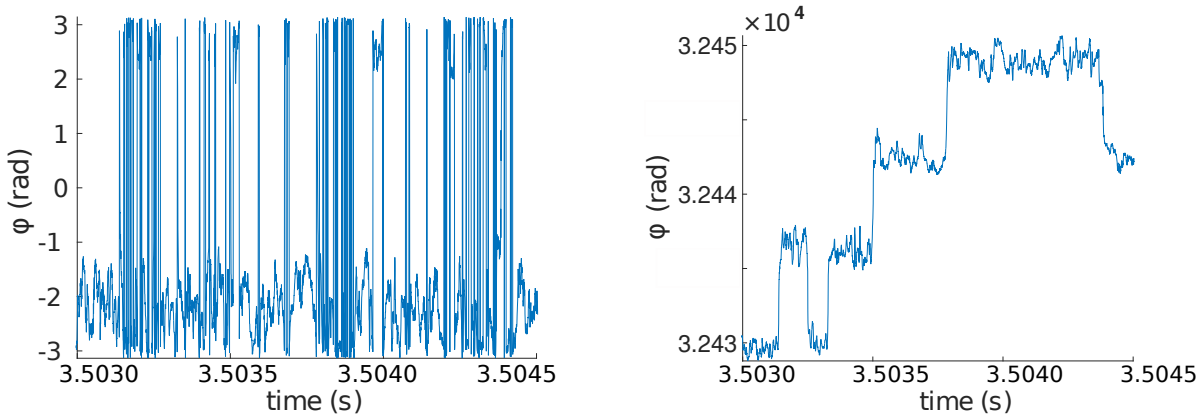

(a) wrapped ϕ (b) unwrapped ϕ

Figure 5.5: Time traces of (a) wrapped and (b) unwrapped phase signals.

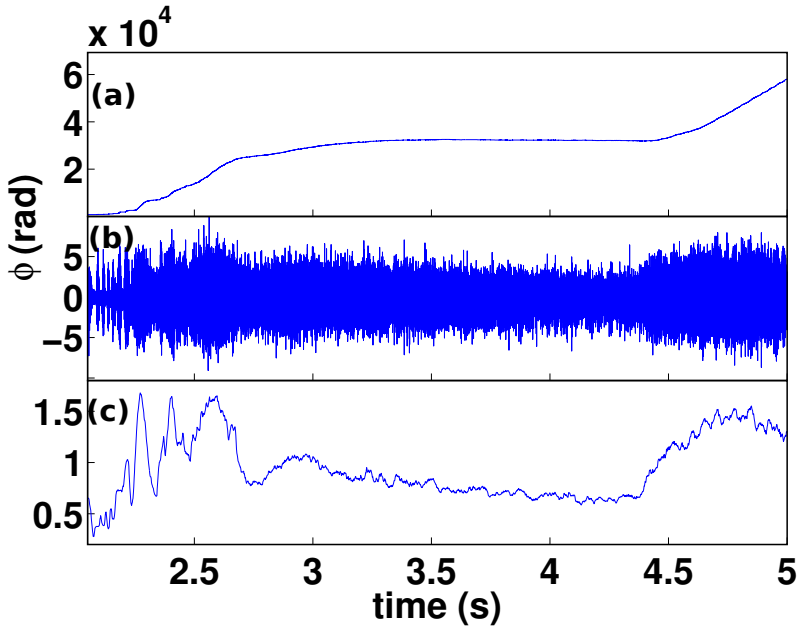

Figure 5.6: Time traces of (a) unwrapped phase, (b) filtered phase and (c) standard deviation of phase for Q band signal of FFH reflectometer in density ramp-up discharge #33484.

An illustrative example for a larger time scale is presented in Figure 5.6 displaying results from measurements performed with the Q band of the FFH reflectometer, operating in fixed frequency during the entire discharge #33484. Shown in the figure are time traces of: (a) the unwrapped phase; (b) the unwrapped phase after filtering out the low frequency components;

and (c) the standard deviation of the signal displayed in (b) using a 1.5 ms time windows. As can be seen in Fig. 5.6.a, there is an almost continuous increase of the phase (due to the cumulative $\pm 2\pi$ phase jumps), while a continuous motion of the plasma reflecting layer with this magnitude would be unrealistic. This type of phase evolution usually called phase drift or runaway has been observed in many tokamaks [190–192]. The phase jumps are reported in many reflectometer signals [159, 190, 193, 194] and are reproduced also by full-wave simulations for high level of density fluctuations [195].

The best way to remove the phase runaway effect is to apply a high pass filter. After testing different types of digital filters, high pass filters with cutoff frequency of ≈5 kHz with an order of 4096 and an Hamming window were selected, for signals with Nyquist frequency of 1 MHz and 8 s of acquisition. The Matlab function filtfilt was used, which performs zero-phase digital filtering by processing the input data in both the forward and reverse directions [196].

Figure 5.6 provides a clear illustration of the strongly pronounced (and cumulative in time), phase runaway effect (Fig. 5.6.a) and the importance of filtering out the low frequency components of the phase signal (Fig. 5.6.b). It is observed that filtering is effective in removing phase runaway.

The adopted procedure to remove runaway effects proved to be very effective as illustrated in Fig. 5.6.c. As it will be shown in chapter 8, the results in that figure demonstrate the high sensitivity to the phase derived from reflectometry to the changes of plasma fluctuations along the discharge.

5.4 Comparison of phases from FFH and FM-CW systems

To test the reliability of results obtained with the Hilbert Transform technique, the phase derived from the homodyne signal of the FM-CW system was compared with the phase obtained directly from the heterodyne FFH system (ϕ_{ref}), taken as a reference.

First, the phase is estimated from the quadrature signal, Q^{HT} of the FFH obtained using the Hilbert transform technique (the Q signal is not used) and the corresponding phase estimation ϕ^{HT}_{FFH} is compared with the reference phase ϕ_{ref}. Secondly, the Hilbert transform is applied to the signal from FM-CW system (I signal) and the phase ϕ^{HT}_{FM-CW} is determined.

Table 5.1 summarizes the data analysis steps used to estimate absolute density fluctuations levels from reflectometry signals with the FFH and FM-CW systems.

The phase from different estimations in AUG shot #33484 with the Q band of both reflectometry systems operating at F = 36 GHz are displayed in Figure 5.7.

It should be noted here that although the antennas of the two reflectometers are located

Table 5.1: Data analysis steps

FFH reflectometer (I, Q signals)	FM-CW reflectometer (I signal only)
1. Correction of I, Q signals	1a. Applying HTT to $I(t) = A(t)cos(\phi(t))$ signal to obtain analytical $Q'(t)$ signal 1b. Correction of $I(t)$ and $Q'(t)$ signals
2. Obtaining phase $\phi(t) = tan^{-1}[Q(t)/I(t)]$ and/or $\phi'(t) = tan^{-1}[Q'(t)/I(t)]$ 3. Phase unwrapping (by Seo method) 4. Removal of phase runaway by filtering out low frequency components 5. Estimation of $\delta n_e/n_e$ with 1D C. Fanack model (see section 3.5.1) using phase and local density gradients	

at different toroidal sectors and at slightly different Z-coordinates (see section 3.3), the two systems operating at the same probing frequency ensures probing layers at quite close radial locations.

As can be seen from Figure 5.7, the three phase estimations are both in good qualitative and quantitative agreement demonstrating the reliability of the phase measurements derived from FM-CW using the Hilbert Transform technique.

However, it seems that the sensitivity to variations of the fluctuations along the discharge is lower when the Hilbert Transform technique is applied. This is illustrate in Fig. 5.7.(a) for [t $\approx$ 2.0$-$2.7 s], where the strong/fast oscillations of the phase derived from the IQ signals of the FFH system, are less pronounced when HTT is applied, especially when it is applied to the FM-CW signal.

5.5 Estimation of the density fluctuation level

The level of density fluctuations and the corresponding radial profile (particularly at the edge plasma), are the relevant quantities for physics studies in fusion devices, as they can contribute to improve the understanding of transport and its related plasma losses.

Under the adopted Fanack model [155], the level of fluctuations is estimated from:

$$\frac{\delta n_0}{n_{cr}} = \frac{\Delta\Phi_{max}}{\pi\sqrt{2}} \left(\frac{k_f/k_0}{L_n/\lambda_0} \right)^{1/2}, \tag{5.14}$$

where n_{cr} is the value of the density at the cut-off, $\Delta\Phi_{max}$ is the maximum phase shift, k_f is the wavenumber of the fluctuations, k_0 is the vacuum wavenumber, L_n is the density gradient length at the cutoff layer, and λ_0 is the vacuum wavelength (see section 3.5.1).

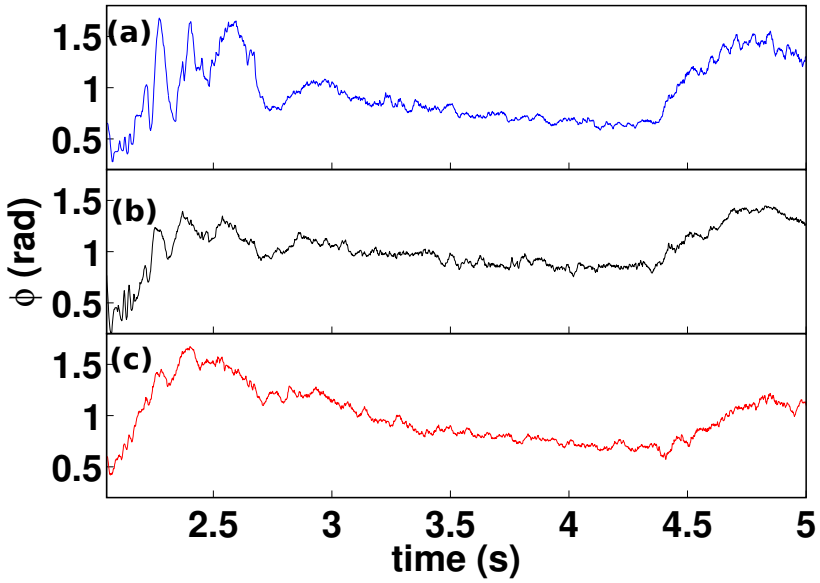

Figure 5.7: Phase standard deviations obtained in the AUG density ramp-up discharge #33484 with the Q band signals of both FFH and FM-CW reflectometers, operating at the same frequency (F = 36 GHz). Displayed results correspond to phases obtained using: (a) IQ signals from the FFH system (reference phase ϕ_{ref}); (b) the Hilbert transform applied to the I signal from the FFH system (phase ϕ^{HT}_{FFH}) and (c) the Hilbert transform applied to the homodyne signal of the FM-CW system (phase ϕ^{HT}_{FM-CW}).

Therefore, the estimation of the density fluctuation level requires a separate measurement of the density profiles to obtain the local gradients for the estimation of plasma fluctuations and also the radial position of each probed density layer.

5.5.1 Density profiles from reflectometry

Averaged density profiles are obtained using FM-CW reflectometer operating in swept mode or from IDA (which is a combination of Thomson scattering (TS), Lithium beam (LIB) and reflectometry data when available). Normalized poloidal flux coordinates ρ_{pol} are normally employed because it allows the absolute comparison of the radial profile performed at different poloidal locations.

Measurements in this study were focused in the region around separatrix where density gradients are high and the uncertainty about the radial location of probed plasma layers from reflectometry diagnostic is low (in the range of a few mm). However, the ρ_{pol} estimation that requires a magnetic equilibrium reconstruction introduces additional uncertainties in the position of the separatrix (in the order of a few mm).

Although density profiles can be obtained from other diagnostics, there are significant advantages in obtaining the density profiles from the operation in swept mode of the FM-CW

reflectometer. It is the only density profile diagnostic that performs profile measurements at both the HFS and LFS and it features both high spatial and temporal resolutions [109]. Moreover fluctuations and profiles are obtained with the same system, thus providing measurements with the same reflectometry technique and at the same radial location.

5.5.2 Density fluctuation level

The method to estimate the density fluctuation level was described both here and chapter 3. The basic quantity is the unwrapped phase obtained after the removal of the low frequency components due to the runaway effects. However there are some cases where the low frequency components are not only due to the runaway effects but are also due to plasma fluctuations.

As shown in the chapter 8, in the SOL, the low frequency components (below 15 kHz) of density fluctuations in a density ramp-up discharge increase with the line-averaged density being dominant at high densities. So, if a high pass filter (with cutoff frequency around 5 kHz) is applied to remove phase runaway, the absolute fluctuations levels would be underestimated. Consequently, for those situations the phase analysis presented here cannot be applied and an alternative method must be employed. Taking as a basis previous experimental studies performed at CTT and DIII-D, showing that the complete homodyne reflectometry signal, although cannot provide quantity information about the density fluctuations, can closely represent the density fluctuation behaviour [156], we use the homodyne FM-CW signal. A weighting factor $\sqrt{\lambda_0/L_n}$ such as it is included in the Fanack model was introduced in the analysis to take into account the reflectometry response to different density gradients. It will be shown later that the fluctuation properties derived from this analysis are in good agreement with results from the reciprocating Langmuir probe.

5.5.3 Radial profiles of density fluctuations

An example of a radial profile of density fluctuations obtained with Q and V channels in L-mode USN discharge #33547 using both fluctuation data from FFH and FM-CW reflectometers is presented in Figure 5.8. This discharge was selected because the FFH reflectometer was operated in long frequency steps (100 ms) thus providing a good statistics. The density fluctuations levels were estimated using data from both reflectometers probing the same fixed densities layers. The location of the corresponding cutoff layers and the local density gradients were obtained from FM-CW reflectometer operating in swept (profile) mode in the pair discharge #33546. As seen in the figure, the radial profiles of the density fluctuations from the two reflectometry sys-

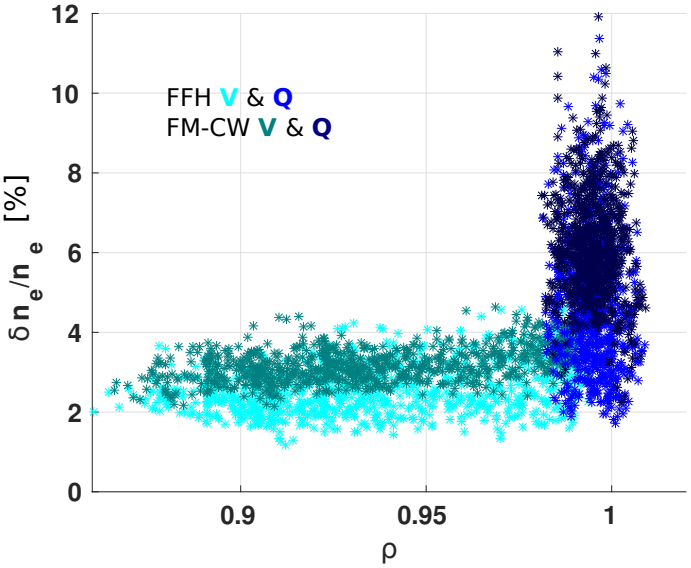

Figure 5.8: Radial profiles of density fluctuations, $\delta n_e/n_e(\rho_{pol})$, obtained in USN discharge #33547 with the Q and V bands of the FFH (cyan and blue) and FM-CW (dark cyan and dark blue) reflectometers, operating at the same frequencies - 36 GHz (Q band) and 52 GHz (V band). The locations of the probed layers were taken from FM-CW density profile measurements performed in paired discharge #33546.

tems are in good agreement. In particular, the large increase of the fluctuation level near the separatrix is detected by both diagnostics.

Also, for the same density layers and radial locations, similar values of $\delta n_e/n_e$ are obtained. This is a strong point for validating of the data analysis procedure used to estimate fluctuations from the homodyne signal from FM-CW reflectometer which is of key importance because it only that system measures at both HFS/LFS.

Comparison of density fluctuations from reflectometry and Langmuir probes

A further proof of the reliability of the fluctuation measurements with the FM-CW system is the comparison of reflectometry results with data from other AUG diagnostics, especially from Langmuir probes that is usually the reference diagnostic to study SOL fluctuations.

Figure 5.9 displays the density fluctuations at several radial locations derived from FM-CW reflectometer data at the LFS in L-mode discharge #33484 (during a time interval where the edge line-averaged density was $\bar{n}_e \approx 1.3 \cdot 10^{19}$ m^{-3}) and from the reciprocating Langmuir probe data (estimated using the ion saturation current measurements neglecting temperature fluctuations) in similar experimental conditions [11].

As can be seen from the figure, the radial profile of density fluctuations from reflectometry match quite well the Langmuir probe data. The larger values obtained with Langmuir probes may be justified by the fact that density fluctuation are overestimated when calculated from

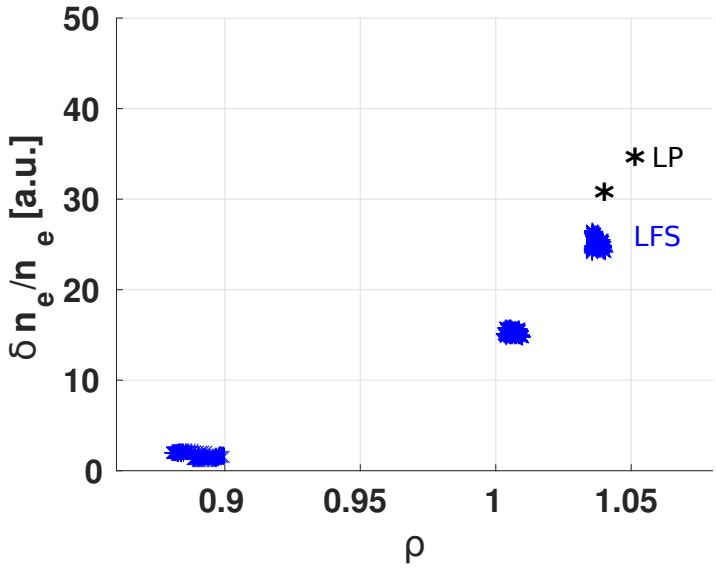

Figure 5.9: Radial profiles of $\delta n_e/n_e$ obtained in the LFS from the FM-CW reflectometer in L-mode discharge #33484 with an edge line-averaged density of $\bar{n}_e \approx 1.3 \cdot 10^{19}$ m^{-3}. The location of the probed layers is measured with the FM-CW system operated in profile mode in the paired discharge #33483. The star symbols indicate values of $\delta n_e/n_e$ estimated from the reciprocating Langmuir probe data at the LFS in similar experimental conditions [11].

the ion saturation current neglecting temperature fluctuations. The good agreement between reflectometry and Langmuir probe fluctuating data further confirm the reliability of reflectometry $\delta n_e/n_e$ estimations, even in the cases where the turbulence level is significantly high.

5.6 Discussion and outlook

The methodology here developed to estimate density fluctuations from the homodyne signal measured with the FM-CW reflectometry signal relies on estimation of the phase associated to fluctuations using the Hilbert transform technique. Experimental results and its comparison with similar data from other AUG diagnostics show the reliability of the estimated fluctuation levels, although there may be some limitations of the Hilbert transform application to the reflectometry homodyne signals. First it was shown that the phase derived from the FM-CW system and the phase obtained directly from the heterodyne FFH system are in good agreement. Secondly, the validity of the 1D Fanack model (see section 3.5) was tested from the comparison of reflectometry results with similar data from other ASDEX Upgrade diagnostics. Here, a good agreement was also found between density fluctuations from the FM-CW system and similar data from Langmuir probes (outside the separatrix) and Li beam diagnostic (just inside the separatrix) [197].

However, the validation of the fluctuation data from the FM-CW reflectometry by comparison

with other AUG diagnostics cannot be fully performed because those diagnostics are limited to the LFS SOL while reflectometry can measure also beyond the separatrix both at LFS and the HFS.

Full-wave simulations coupled to turbulence codes might contribute to the validation of the results in the full regions where fluctuations are probed by reflectometry. Numerical studies would as well be useful to support the density fluctuations especially at high turbulence levels, that is a critical issue in the SOL plasma.

According to the 1D Fanack model, in order to estimate the $\delta n_e/n_e$ levels from reflectometry it is necessary (in addition to the phase data) to know the local density gradients. Those are obtained from the density profiles measured with the same FM-CW system operating in swept frequency mode. The density profiles provide also the location of the density layers where the fluctuations are measured. For a reliable study of $\delta n_e/n_e$ poloidal asymmetries measurements of density profiles at the both the HFS and the LFS sides are essential. Indeed, it was found that density profiles are LFS/HFS symmetric only in L-mode discharges when the core line-averaged density is $\lessapprox 4 \cdot 10^{19}$ m^{-3}. For higher electron densities n_e profiles are LFS/HFS asymmetric [109]. It will be shown in section 6.3, that the asymmetry is more pronounced with improved confinement (I-phase) rather than in L-mode.

As presently, the FM-CW diagnostic is not able to change the operation regime during one discharge, the measurement of density fluctuations requires two identical discharges profiles, one in fixed frequency (to obtain the basic signal for fluctuation analysis) and the other in swept mode to measure the density profile (that provides the local gradients and also the location of probed layers). As quite often it is not easy to get two identical discharges, it may difficult the investigation, especially when the density profiles exhibit variations in short time scales (below the millisecond) that overlap with the typical time scales of turbulence.

Chapter 6

Turbulence in different magnetic configurations

> "Well, I never heard it before, but it sounds uncommon nonsense."
>
> — Lewis Carroll, Alice in Wonderland

The ballooning character of the transport suggests that LFS/HFS turbulence should strongly depend on the single/double magnetic topology because the connections between the LFS and the HFS regions are modified. In this chapter, we investigate the impact of different magnetic configurations on the HFS/LFS density fluctuations. The experimental data at the HFS is very limited, so the ballooning character of turbulence can be further studied from the radial profiles of density fluctuations, inside and outside of separatrix at both the LFS and the HFS. The magnetic configurations differ mainly at the edge/SOL, so it is expected that transport should be modified in those two regions.

Studies where the edge turbulence is characterized in the USN and LSN configurations can also contribute to the understanding the mechanisms responsible for the dependence of the power threshold on the ion ∇B direction. There are experimental observations that the L-H transition power threshold [126, 198, 199] strongly depends on unfavorable/favorable configuration (that corresponds to ion ∇B drift direction away/towards the dominant X-point, which can be achieved in upper/lower magnetic topology). The L-H threshold power is lower for the favorable configuration than for the unfavorable one [123–125]. A possible candidate for the P_{th} difference is the $E \times B$ shear flow, once a stronger flow shear was observed in AUG for magnetic topologies with a lower L-H power threshold near the separatrix [120].

The effect of magnetic configuration on plasma turbulence was studied in other machines,

such as Alcator-C Mod, DIII-D, ASDEX and EAST [92, 97, 115–117, 119]. Measurements were limited either to the SOL (Alcator-C Mod, ASDEX and EAST) or to the edge (DIII-D) plasmas, but no global and unique interpretation was presented. Further investigation is needed to obtain a consistent picture about the poloidal asymmetries of turbulence versus magnetic configuration that covers both edge and SOL plasmas.

Reflectometry FM-CW system is able to probe density fluctuations from edge to SOL at the LFS and simultaneously at the HFS, where experimental information is scarce. Therefore this diagnostic can provide a valuable contribution for better understanding transport asymmetries (e.g. ballooning-like transport). Furthermore, the diagnostic operates in O-mode, which is a major advantage to study the effects on density fluctuations of different magnetic topologies, once the measurements solely depend on the plasma density and are not sensitive to the magnetic field.

6.1 Reference case: LSN L-mode

We consider as the reference case plasmas in LSN and L-mode confinement regime because tokamaks typically operate in LSN magnetic topology and most of the experimental data is available for this configuration.

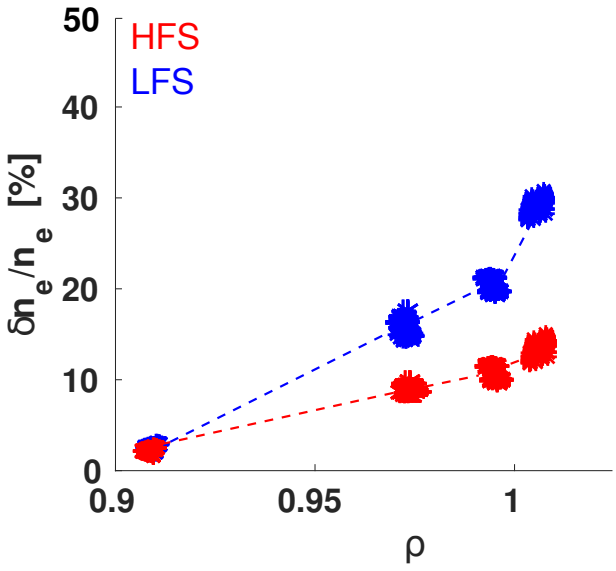

Figure 6.1: Radial profiles of $\delta n_e/n_e$ at the HFS (red) and the LFS (blue) in L-mode LSN discharge #33631 .

Not only density fluctuations measurements are important for turbulence analysis but also density profiles from reflectometry are essential for turbulence analysis because they provide the localization of the plasma layers where density fluctuations are measured and the local

density gradients needed to estimate the fluctuation level. When reflectometry profiles were not available and profile symmetry could be assumed, IDA profiles (obtained only at the LFS) were used. This is the case of low density discharges in L-mode but, for higher core line-averaged electron densities ($n_{e,c} > 4 \cdot 10^{19}$ m^{-3}) the density profiles exhibit strong HFS/LFS asymmetries [109] and reflectomery data must be employed.

Radial profiles of $\delta n_e/n_e$ at the HFS and the LFS in LSN magnetic configuration (L-mode) are displayed in Fig. 6.1 for discharge #33631 at a period when the core line-averaged density is constant, $n_{e,c} \approx 3.7 \cdot 10^{19}$ m^{-3}. Fluctuation levels were estimated using a time range of 100 ms.

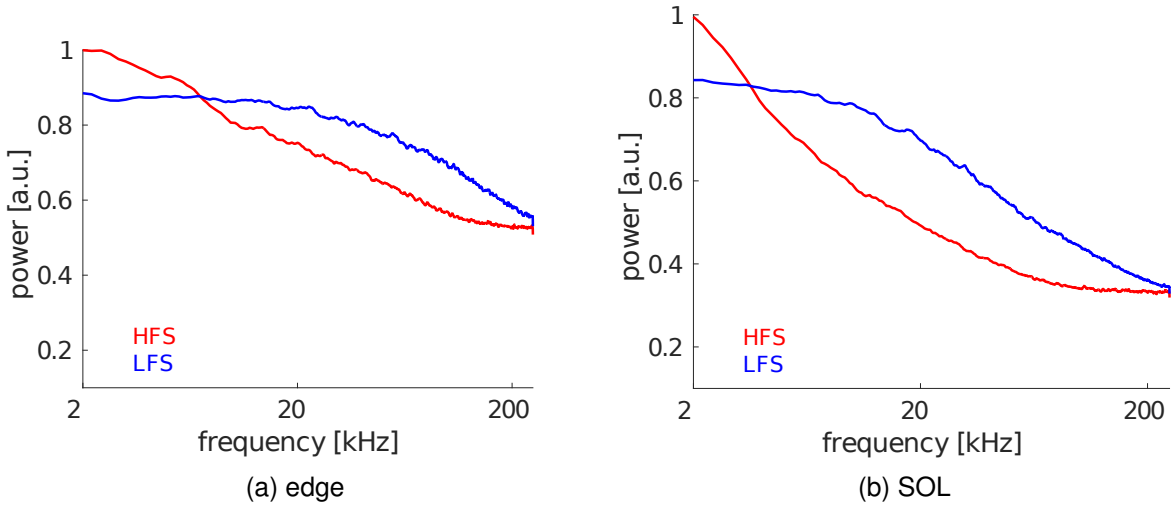

(a) edge (b) SOL

Figure 6.2: Power spectra of FM-CW reflectometer signals measured in L-mode LSN discharge # 21418 at the LFS (blue) and the HFS (red) at: (a) edge [$\rho : 0.92 - 0.93$] and (b) SOL [$\rho : 1.02 - 1.03$].

Results reveal that density fluctuations increase radially at both the LFS and the HFS in the edge and SOL regions as expected. Fluctuations are lower at the HFS by a factor of $\sim$2 in the SOL ($\rho \approx 1.01$) and close to the separatrix, which is consistent with the dominant ballooning-like transport.

It has been shown previously in [156] that the reflectometry homodyne signals represent properly the density fluctuations behaviour even at the high fluctuations levels as those occurring at the SOL. Figure 6.2 displays the frequency power spectra of the homodyne signals at the LFS and the HFS measured in the LSN L-mode discharge #21418 with core line-averaged density $n_c \approx 3.7 \cdot 10^{19}$ m^{-3}. The HFS and the LFS power spectra are different at both the edge and the SOL. Significantly narrower power spectra are observed at the HFS than at the LFS, as was also found in Alcator C-Mod at the SOL [86].

6.2 Comparison of turbulence in USN and LSN (L-mode)

Turbulence was studied in upper single null and lower single null discharges with similar plasma parameters. Results were compared with numerical data from the dedicated simulations using a gyrofluide GEMR code.

6.2.1 Radial profiles of density fluctuations

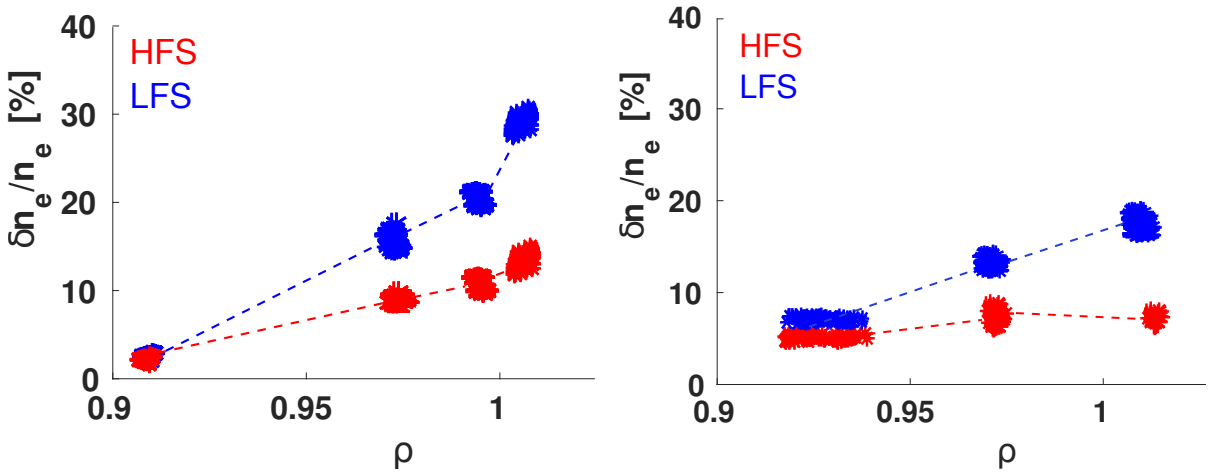

(a) LSN (b) USN

Figure 6.3: Radial profiles of $\delta n_e/n_e$ at the HFS and the LFS in L-mode for (a) LSN and (b) USN magnetic configurations. LSN data are measured in discharge #33631, USN in discharge #34534.

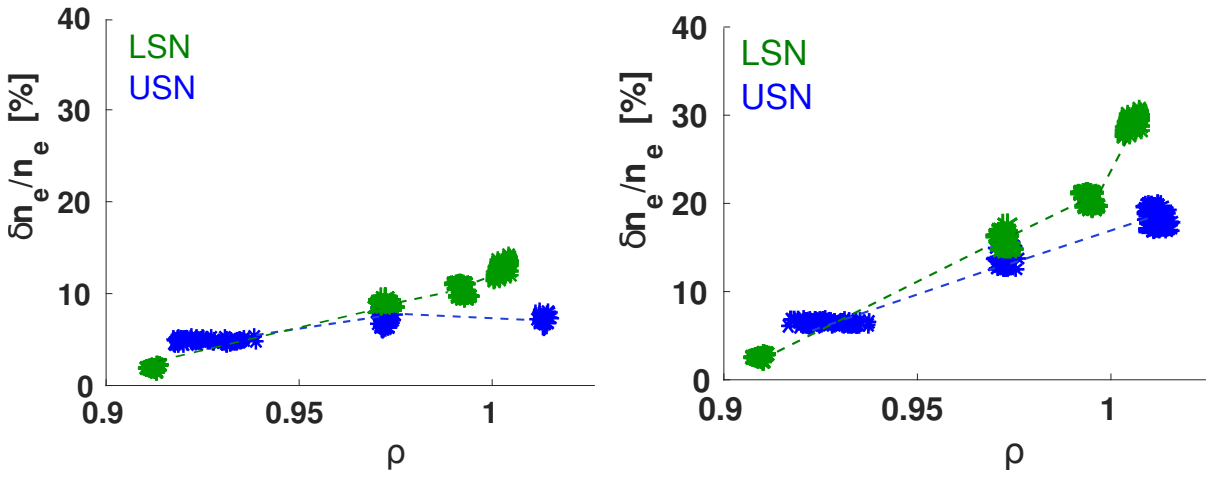

(a) HFS (b) LFS

Figure 6.4: Radial profiles of $\delta n_e/n_e$ at (a) the HFS and (b) the LFS in L-mode for USN in discharge #34534 (blue) and LSN in discharge #33631 (green).

Radial profiles of the density fluctuations are compared between the LFS and the HFS (Figure 6.3) and for the USN and LSN configurations in L-mode (Figure 6.4).

In the SOL ($\rho \approx 1.00 - 1.02$), density fluctuations are larger at the LFS than at the HFS by a factor of around 2 in LSN and USN, which is consistent with the dominant ballooning-like transport for both magnetic configurations. Reflectometry data also reveal that in the SOL density fluctuations are lower in USN than in LSN by a factor around 2 both in the HFS and the LFS. In the edge plasma no significant differences are observed between USN and LSN configurations and between the HFS and the LFS differences are smaller than in the SOL.

6.2.2 Density and temperature gradients

In order to understand the mechanism behind the different fluctuation levels in USN and LSN in L-mode (seen in the previous section), we analyze the density and temperature profiles in both configurations. Figure 6.5 shows the electron density profiles obtained by the new Lithium beam diagnostic at the LFS for the USN discharge #34568 (blue) and LSN discharge #33426 (green). The density gradients are similar in both magnetic configurations around the separa-

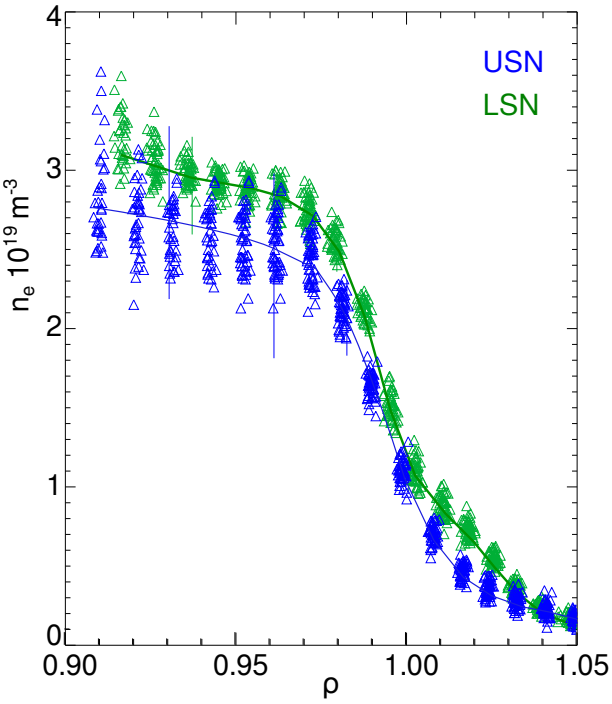

Figure 6.5: Electron density n_e radial profiles at the LFS for USN and LSN magnetic configuration by the Lithium beam diagnostic in discharges #34568 and #33426, correspondingly.

trix, while clear differences are observed in the fluctuation level in this region (see Figure 6.4b). The density is higher (approximately, 20% higher) and density gradients are steeper in the LSN than in the USN. Therefore, the observed lower fluctuation level in USN cannot be attributed to the density gradients. We consider also the electron temperature profiles, provided by the Thomson scattering diagnostic. Figure 6.6 displays the electron temperature radial profiles at

the LFS in USN and in LSN L-mode discharges. As can be seen, T_e profile is steeper for

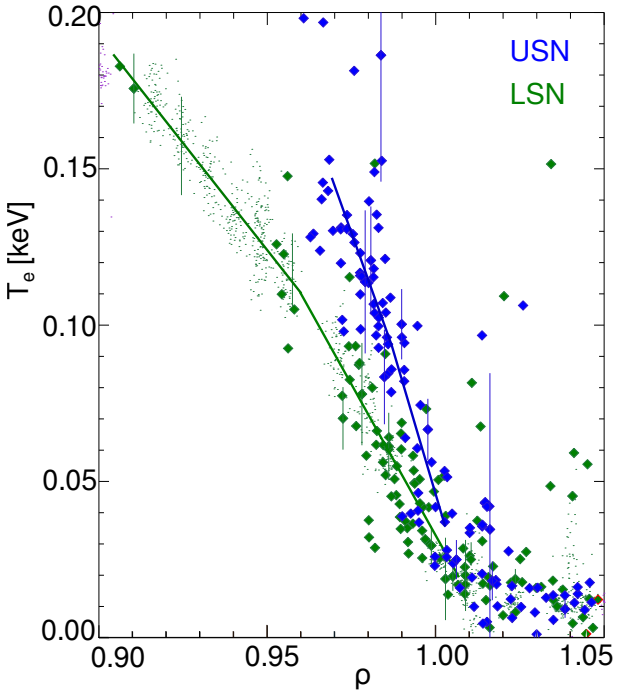

Figure 6.6: Electron temperature T_e radial profiles at the LFS for USN and LSN magnetic configuration by Thomson scattering diagnostic in discharges #34568 and #33426, correspondingly.

the USN configuration at the separatrix region. Under an assumption that ion temperature T_i is similar to the electron temperature T_e at the separatrix region, one would also expect a larger radial pressure gradient and correspondingly a higher radial electric field E_r shear at the separatrix region for USN. Therefore, lower density fluctuation levels in USN could be justified correspondingly to higher radial electric field shear. The electron temperature and density gradients revealed to be similar ($L_{n_e}/L_{T_e} \approx 1$) in USN. Our results show that the poloidal asymmetries in the density fluctuations have a ballooning character and that the driven mechanisms do not appear to be different for USN and LSN magnetic configurations.

6.2.3 GEMR simulations

Motivated by the unexpected lower level of density fluctuations at the SOL for the USN than in LSN configuration, GEMR simulations have been performed by Peter Manz with support of Tiago Ribeiro.

Experiments with different magnetic configurations have been simulated with the gyrofluid GEMR code with the same plasma parameters used for the both configurations. The numerical simulation studies were done in circular plasma geometry and different configurations were simulated by varying the position of limiters. Although the X-point geometry is not taken into

account, the configurations are called here LSN and USN to simplify the comparison between simulated and experimental results [114]. In this work, a setup with equal electron temperature and density gradients $L_{n_e} = L_{T_e}$ was chosen according to the experimental data.

Radial profiles of $\delta n_e/n_e$ at the LFS and the HFS obtained with GEMR for the USN and LSN magnetic configurations are shown in Figure 6.7. The simulations performed in a circular

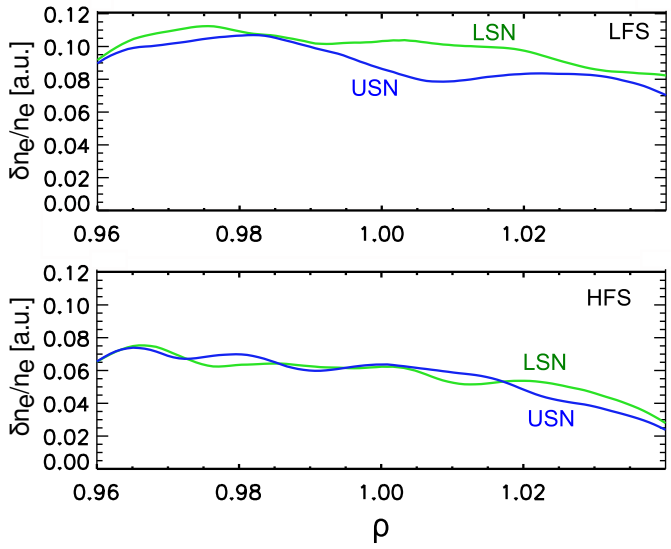

Figure 6.7: Radial profiles of $\delta n_e/n_e$ at the LFS (top) and the HFS (bottom) for USN (blue) and LSN (green) magnetic configurations obtained by GEMR simulations.

geometry with limiter cut configurations, the turbulence levels show the configuration dependence. At the SOL, contrary to the edge plasma, more clear differences are observed between the two configurations. At the HFS, $\delta n_e/n_e$ differences between the USN and LSN are modest and limited to the far-SOL ($\rho > 1.02$). The strongest differences between the two configurations are predicted for the region $0.99 \leq \rho \leq 1.03$ at the LFS where fluctuation are lower for the USN in agreement with our observations. Overall, it can be concluded that the simulations support the experimental results.

6.2.4 Discussion

The results presented above are focused on lower and upper single null L-mode plasmas with the ion ∇B drift directed towards/away from the X-point, respectively. We show that the magnetic topology has a strong influence on the SOL $\delta n_e/n_e$ profiles. Radial profiles of $\delta n_e/n_e$ from reflectometry reveal an increasing level with radius both at the HFS and the LFS. Power spectra of fluctuations are narrower at the HFS than at the LFS, which is consistent with results in Alcator C-Mod at the SOL [86].

Density fluctuations reveals pronounced poloidal asymmetries in both topologies. In each

magnetic configuration, the fluctuation levels at the HFS are lower by a factor of ≈2 (at the SOL region, $\rho_{pol} \approx 1.00 - 1.02$), which is consistent with the dominant ballooning-like transport. The comparison reveals that density fluctuation levels at the edge (for $\rho < 1.00$) are similar in both configurations, while for $\rho > 1.00$, $\delta n_e/n_e$ in USN are found to be lower than in LSN by a factor of ≈2 (at $\rho \approx 1.00 - 1.02$), both at the LFS and the HFS. Dedicated simulations with the gyrofluid GEMR code support these experimental findings. Thus, the comparison USN/LSN reveals that USN, characterized by a higher power threshold of the L-H transition, is accompanied by lower density fluctuation levels, which seems at the first look to be contradictory. The lower density fluctuations in USN than in LSN has been also observed in other tokamaks such as Alcator C-Mod and at DIII-D close and outside the separatrix, but no interpretation was given. At DIII-D results were obtained with beam-emission spectroscopy at the LFS edge for $\rho : 0.90 - 1.00$ [119], while at Alcator C-Mod measurements were performed at the LFS and the HFS SOL [97] by Langmuir probes, showing a more pronounced effect at the LFS SOL for ~ 1 cm from separatrix) [97].

At AUG, the observed difference of density fluctuation levels cannot be attributed to the density gradients. A possible candidate may be associated with the observed difference in gradients of electron temperature (larger in USN at the separatrix region) and correspondingly different $E \times B$ shear flow, which is considered as a stabilizing mechanism for density fluctuations [145–147]. The larger positive E_r shear is expected in USN in comparison to the LSN near the separatrix at the LFS. Larger $E \times B$ shear flow can lead to a lower fluctuations levels and to a reduced radial transport. Indeed, at the SOL lower density fluctuation levels are observed both experimentally and with gyrofluid simulations in USN.

The USN magnetic configuration is also known to be characterized by an higher L-H power threshold [25]. According to the shear decorrelation mechanism, the difference in turbulence properties and L-H transition power threshold for both favorable and unfavorable magnetic configurations could be also associated with the radially sheared $E \times B$ flows [145, 200, 201]. As the L-H transition is expected to occur when the sheared flow is high enough to overcome the turbulence growth rate, the larger E_r shear can be expected to correspond to the lower power threshold P_th, which does not seem to be the case in USN.

Overall, the large E_r shear assumed at the separatrix region in USN (in comparison with LSN) could justify the observed lower density fluctuation levels but can not be easily linked to the higher P_{th}.

Figure 6.8 displays the confinement parameter H_98, the ohmic heating power P_{OH} and the total radiation power P_{rad} for the considered time range of the discharges in USN and LSN

configurations in L-mode. The total radiation power is higher in USN, while the heating power

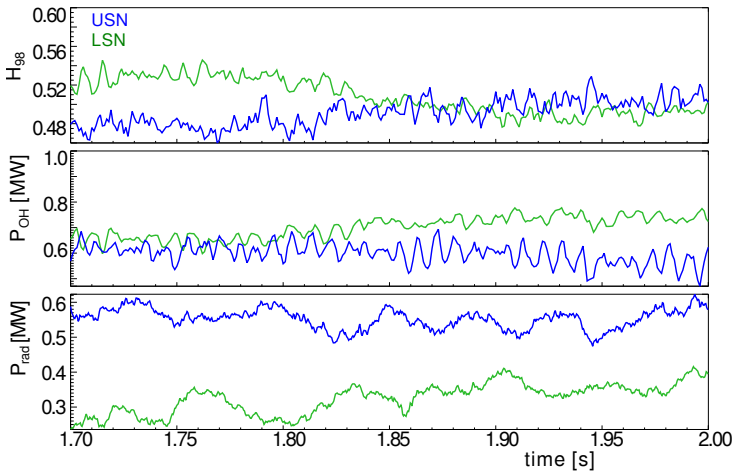

Figure 6.8: Confinement parameter H_98, ohmic heating power P_{OH} and the total radiation power P_{rad} for USN (blue) and LSN (green) magnetic configurations in L-mode in discharges #34568 and #33426, respectively.

is similar. The larger radiation losses in USN can be a possible justification for the higher P_{th}.

Further studies with simultaneous measurements of the Er shear and density fluctuation levels around the separatrix in discharges with different magnetic configurations/reversed magnetic field for different density values should be performed for a better understanding of the relationship between shear flows, density fluctuations and the L-H transition aiming at clarifying the turbulence stabilization mechanism.

6.3 Comparison of fluctuations in LSN and DN (I-phase)

It was found for the first time on ASDEX [112] that density fluctuations in the double null configuration at the HFS are insignificant, i.e. when the separatrix connects the upper and lower X-points thus subdividing the SOL into the LFS and the HFS regions without any connection along field lines [92]. Experiments in double-null plasmas on Alcator C-Mod [113] confirmed that turbulence levels are substantially lower at the HFS SOL than at the LFS, revealing further compelling evidence for the existence of a strong ballooning-like transport mechanism.

Here we analyze dedicated AUG discharges where the magnetic topology evolves from upper single null to lower single null through double null. We study the temporal evolution of the density profiles and the correspondent fluctuation levels in the lower single null and double null magnetic configurations, where the confinement is characterized by the I-phase regime (see description of the experiment in section 4.3).

6.3.1 Radial profiles of density fluctuations

Density profiles in the I-phase are displayed in Figure 6.9. The dashed lines correspond to the three probed density layers where fluctuations are measured with frequencies in the K(n_{eK}), Ka(n_{eKa}), and Q(n_{eQ}) bands. As can be seen, LFS/HFS density profiles are poloidally asymmetric in the I-phase, as they are steeper at the HFS SOL the probed layers at the HFS are located outside the separatrix. Radial profiles of the density fluctuation levels in I-phase are

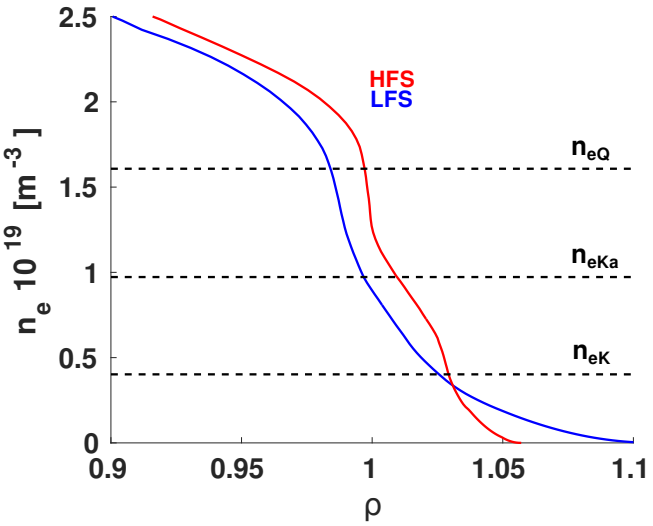

Figure 6.9: Electron density n_e radial profiles at the LFS and the HFS in I-phase discharge #32432. Profiles are averaged over 50 ms.

compared between the LFS and the HFS (Figure 6.10) and for the DN and LSN configurations (Figure 6.11). The error bars along the radius represent the deviation of the probed density layer location during the considered time interval. At the SOL lower $\delta n_e/n_e$ are found in DN in

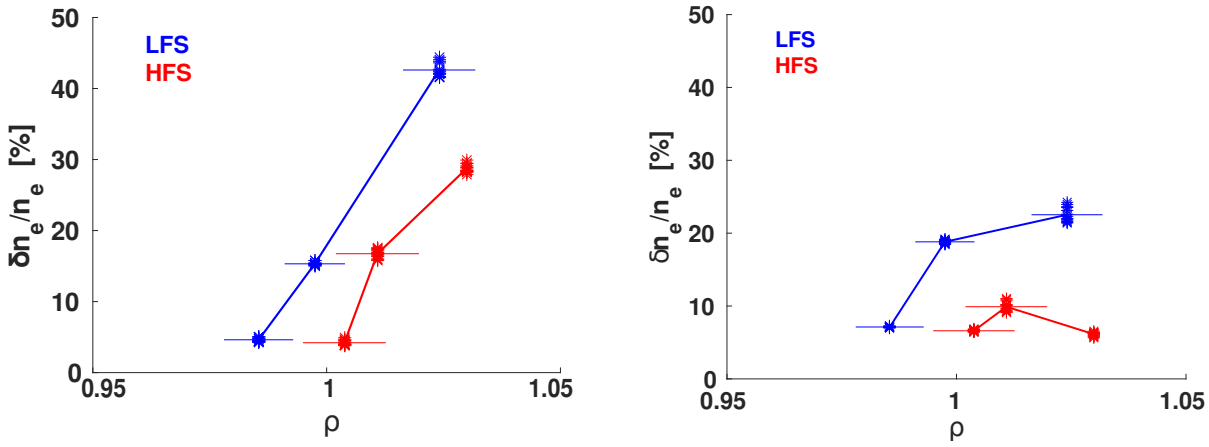

(a) LSN (b) DN

Figure 6.10: Radial profiles of $\delta n_e/n_e$ at the HFS and the LFS in I-phase for (a) LSN and (b) DN magnetic configurations, discharge #31634.

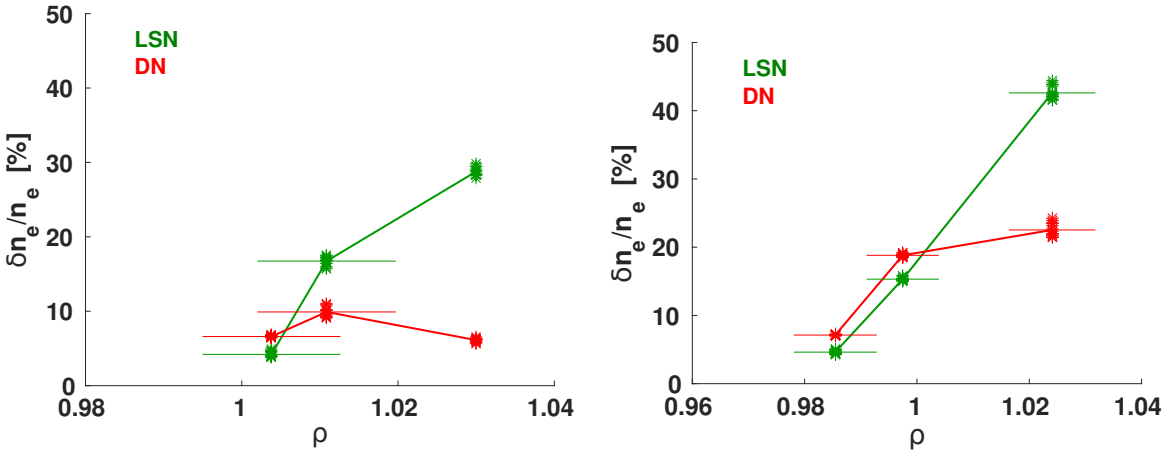

(a) HFS (b) LFS

Figure 6.11: Radial profiles of $\delta n_e/n_e$ at (a) the HFS and (b) the LFS in I-phase for DN (red) and LSN (green) magnetic configurations in discharge #31634.

comparison with LSN magnetic configuration both at the LFS and the HFS, while at the LFS just inside the separatrix no significant differences are observed. The ratio of density fluctuation levels for DN to that in LSN at the SOL ($\rho \sim 1.03$) is around 0.2 and 0.5 at the HFS and the LFS, respectively. Contrary to the single null configurations, in DN density fluctuations profiles display a modest radial variation in the SOL. The poloidal asymmetries of $\delta n_e/ne$ are seen in both DN and LSN configurations with the strongest one found in DN, due to the pronounced decrease of $\delta n_e/n_e$ at the HFS SOL (see Fig. 6.10b). Results suggest that the LFS and the HFS SOL plasmas become disconnected in DN, providing an additional indication of a strong ballooning transport mechanism.

Spectrograms of reflectometry homodyne signals in Figure 6.12a represent the evolution of the density fluctuations in DN and LSN magnetic configurations at the HFS and the LFS SOL ($\rho \approx 1.03$). Figure 6.12b shows the integrated power of signal at the HFS SOL for three frequency ranges around the transition to the DN configuration, revealing that HFS density fluctuations in DN start to be reduced for frequencies above 200 kHz. The reduction of the high frequencies, which corresponds to micro scale turbulence, expands later to the lower frequency range of fluctuations associated with large scale $\delta n_e/n_e$. High frequency density fluctuations have similar amplitudes at the LFS and the HFS SOL, contrary to LF that are smaller at the HFS. This suggests that high frequency density fluctuations at the HFS could be originated at the LFS and therefore react first at the isolation of the HFS from the LFS when the DN configuration is reached.

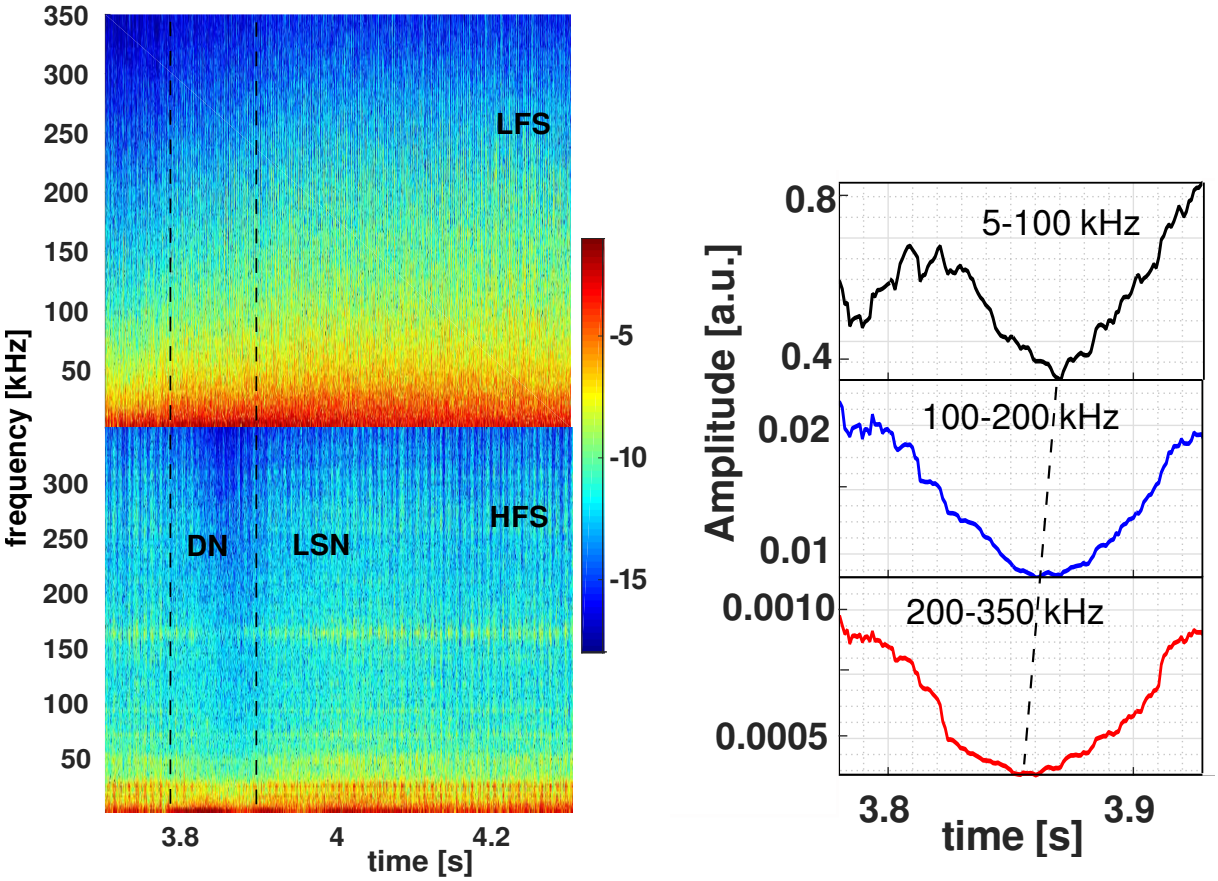

Figure 6.12: (a) Spectrogram of signals by FM-CW reflectometer representing the $\delta n_e/n_e$ at the LFS (top) and the HFS (bottom) at SOL [$\rho : 1.03$] for discharge #31634. Time range corresponding to DN magnetic configuration is indicated by vertical dashed lines; (b) standard deviation of the HFS SOL reflectometry signal corresponding for three frequency ranges indicated at the plot, showing that reduction of $\delta n_e/n_e$ in DN evolves from the high to the low frequencies.

6.3.2 GEMR simulations

GEMR simulations (see section 2.8.1) have been performed with the input of plasma parameters, corresponding to the presented above DN and LSN configurations. A setup with roughly equal electron temperature and density gradient lengths $L_{n_e} = L_{T_e}$ at the separatrix was chosen according to the experimental data (not shown).

Radial profiles of $\delta n_e/n_e$ at the LFS and the HFS obtained with GEMR are shown in Figure 6.13 for the both magnetic configurations. The simulated density fluctuation profiles clearly show a dependence on the magnetic configuration, particularly at the SOL. The strongest difference between configurations is predicted for the region $\rho \geq 1.00$ at the HFS, corresponding to the isolation of HFS SOL plasmas from the LFS SOL. Density fluctuations are observed to be lower in DN configuration also at the LFS SOL. Both findings are in a good agreement with our experimental results. Simulations also predict enhanced level of $\delta n_e/n_e$ in DN at the LFS edge,

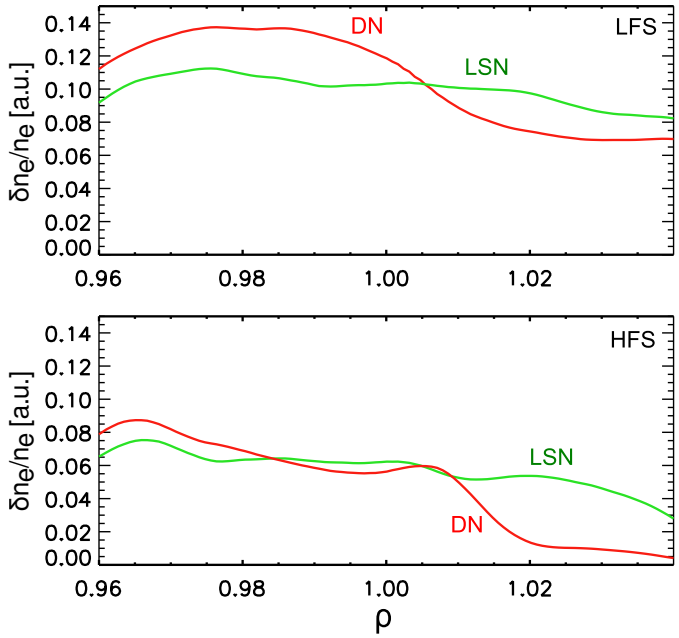

Figure 6.13: Radial profiles of $\delta n_e/n_e$ at the LFS (top) and the HFS (bottom) for DN (red) and LSN (green) magnetic configurations by GEMR simulations.

which is not clearly seen in the experimental data. However, the lack of reflectometry data at the edge due to the outward movement of the probed density layers does not allow a definitive conclusion to be drawn. Furthermore, the predicted reduction of the density fluctuations at the HFS SOL for DN is stronger than observed experimentally. In part, this could be justified by the by the intrinsic noise of the reflectometry system.

6.3.3 Radial electric field profiles

To better understand the reduced density fluctuation level in DN at the LFS SOL, the radial electric field E_r profiles measured by Doppler reflectometry in both configurations at the LFS were compared as shown in Figure 6.14 for discharge #31633. At the LFS, the E_r shear is found to be similar in the SOL and separatrix region for both configurations. Inside the separatrix a lower E_r shear is observed in DN than in LSN. Then, according to the turbulence stabilization theory [145–147], lower fluctuation levels can be expected in LSN than in DN inside the separatrix. Indeed, both the GEMR simulations and experimental results at the LFS show lower fluctuations in LSN at the edge region ($\rho_{pol} < 1$). The mechanism of higher fluctuation levels observed at the LFS SOL in LSN than in DN (experimentally and with the GEMR simulations) requires further investigations, preferably in L-mode, where the Doppler data is more robust.

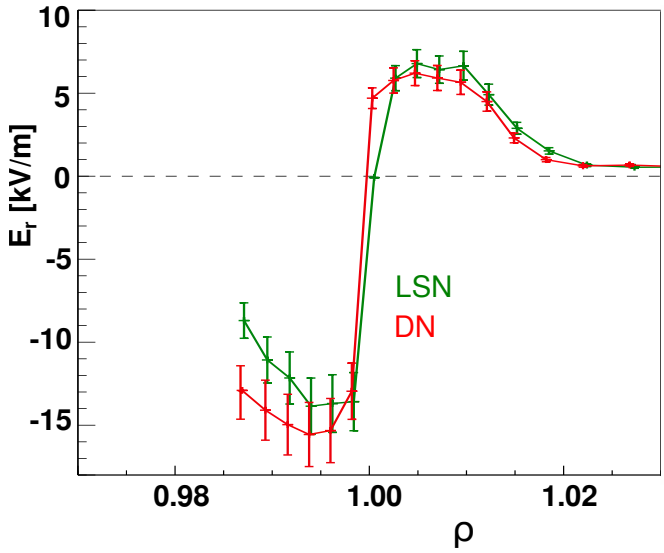

Figure 6.14: Radial electric field E_r profiles at the LFS for DN (red) and LSN (green) magnetic configurations in I-phase by Doppler reflectometry in discharge #31633.

6.3.4 Discussion

Comparison of the experimental results obtained in DN and LSN configurations in I-phase and the corresponding simulations by the GEMR code are in a good agreement, both indicating a lower $\delta n_e/n_e$ in DN in the SOL region. Density fluctuations are observed to be strongly reduced at the HFS SOL in the DN configuration, when this region becomes isolated from the LFS. This provides a strong evidence of the ballooning character of transport. The reduction of density fluctuations in DN at the HFS SOL is supported by previous GEM simulations [114] and results obtained at other machines, namely ASDEX [112], Alcator C-Mod [113, 117]. We further show that the fluctuations reduction starts at the micro scale turbulence (in the frequency range $f > 200$ kHz) and evolves towards lower frequencies. This could indicate a direct connection of micro scale high frequency turbulence at the LFS and HFS SOL plasmas. The lower $\delta n_e/n_e$ observed at the LFS inside the separatrix in LSN configuration may be related with a stronger E_r shear according to the turbulence shear stabilization theory [145–147].

6.4 Summary

Experimental results obtained in USN, LSN and DN reveal a strong influence of the magnetic topology on the density fluctuations, which is mainly pronounced in the SOL rather than in the edge. Poloidal asymmetries of fluctuations are observed to depend on the magnetic topology, in all configurations supporting the ballooning transport mechanism. Dedicated simulations performed with the gyrofluide GEMR code are in a good agreement with the reflectometry

turbulence data.

Both the GEMR simulations and experimental results at the LFS show lower fluctuations in LSN at the edge region ($\rho_{pol} < 1$). This can be associated with a higher E_r shear observed in LSN than in DN, according to the turbulence stabilization theory. Lower $\delta n_e/n_e$ are observed in DN as compared to LSN (I-phase) at the SOL, a better understanding of the mechanism requires further investigations, preferably in L-mode, where the Doppler data is more robust.

At the HFS SOL, the strong reduction of fluctuations in DN indicates that the plasma from the HFS becomes disconnected from the LFS, therefore providing a clear support for a strong ballooning transport.

In L-mode lower fluctuation levels were found in USN than in LSN configuration in the SOL. The mechanism behind the lower turbulence for USN may be associated with a larger E_r shear at the separatrix region suggesting lower fluctuations levels and a reduced radial transport at the SOL.

For further investigation of the connections between density fluctuations and shear flows, comparative experiments with different magnetic configurations in direct/reversed magnetic field for different density values should be performed. This may contribute for better understanding of the edge and SOL turbulence and the mechanisms driving the L-H transition.

Chapter 7

Edge density fluctuations in I-phase

"Curiouser and curiouser!"

— Lewis Carroll, Alice in Wonderland

The I-phase is the intermediate confinement regime between L- and H-mode characterized by the presence of limit cycle oscillations (LCOs) with frequencies from 0.5 to 5 kHz [39]. Understanding the I-phase is important because although a significant progress has been made in describing the L-H transition, the physical mechanism triggering the H-mode has still not been clearly identified. During the LCOs a competition between a turbulence drive and an enhanced shearing flow is observed at AUG leading to modulations in the density fluctuation level and poloidal flow velocity [39]. Also, LCOs were found to modulate the density profile starting inside the LCFS and radially propagating outward into the far scrape-off layer at AUG [37]. In this chapter we further characterize the turbulence properties in I-phase namely to study the radial propagation of density fluctuations and their modulation by LCOs.

7.1 Density fluctuations sensitivity to the confinement inside the separatrix

We study here density fluctuations in the confined region (close to the separatrix) in the I-phase in DN and LSN magnetic configurations using the discharges with magnetic configuration scan described in section 4.3. As shown in chapter 6, density fluctuation in the edge plasma show a weak dependence on the magnetic configuration. Figure 7.1 presents the evolution of density fluctuations and beta normalized in the I-phase, revealing that the density fluctuations are sensitive to confinement changes at the LFS separatrix. The dependence of density fluctuation levels on the beta normalized inside and at the separatrix at the LFS can be clearly seen in

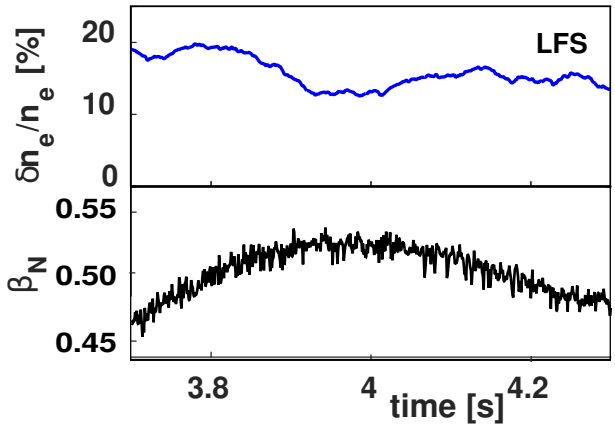

Figure 7.1: Time traces of $\delta n_e/n_e$ at the separatrix at the LFS and beta normalized β_N during a DN-LSN magnetic configuration scan in discharge #31634.

Figure 7.2. At the edge, density fluctuation levels display the expected dependence on the con-

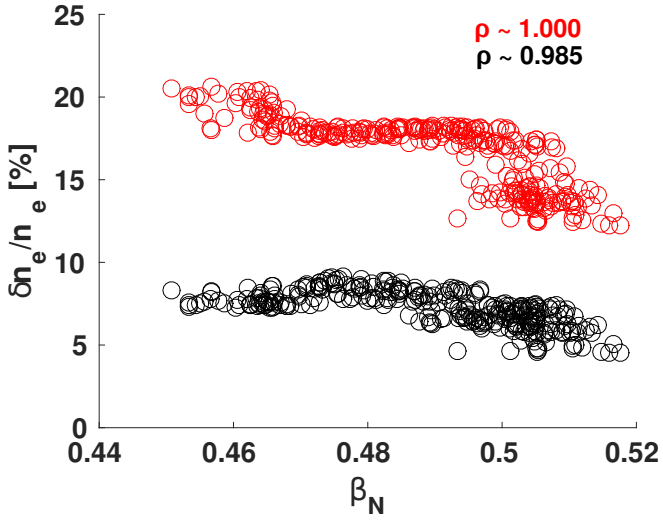

Figure 7.2: Density fluctuation levels $\delta n_e/n_e$ versus beta normalized β_N at the LFS edge and the separatrix at the LFS in discharge #31633.

finement parameter - as β_N increases, density fluctuation levels decrease. This effect is more pronounced at the separatrix, where a confinement increase of approximately 15% corresponds to a decrease of the density fluctuations by $\approx 30\%$.

It should be noted that no fluctuation analysis could be performed at the HFS edge because HFS n_e profiles are steep and shifted outwards(see section 6.3), causing the probed layers to move towards the SOL region.

7.2 Turbulence modulation by LCOs at LFS edge

The above results show that fluctuations are sensitive to the confinement changes in I-phase, which are dominated by LCOs. Here we study the influence of LCOs on the edge plasma fluctuations. Figure 7.3a depicts the frequency power spectra of the reflectometry homodyne signal probing the LFS plasma inside the separatrix (ρ_{pol}: [0.95 - 0.98]) for the time ranges corresponding to the L-mode and I-phase in discharge #31634. It should be noted, that the confinement improvement was achieved by changing the magnetic topology from USN (displaying higher L-H power threshold) through DN and to LSN (with a lower power threshold). The evolution of the power spectra at the LFS edge should be related primarily with the confinement regime modifications rather than with the changes in the magnetic configuration, which has only a modest influence on the edge plasma, as found in the previous chapter 6.

The power spectra (in Fig. 7.3a) show that density fluctuations change significantly from L-mode to I-phase. During the I-phase, density fluctuations decrease in the frequency range $5 - 150$ kHz, a quasi coherent mode (QCM) is clearly seen around $80 - 120$ kHz for the period with the maximum confinement (corresponding to DN) and frequency components below 5 kHz increase. The QCM was studied in AUG before [202, 203] and is typically observed in the I-phase or just after the L-H transition. For better understanding the different behaviour of low and

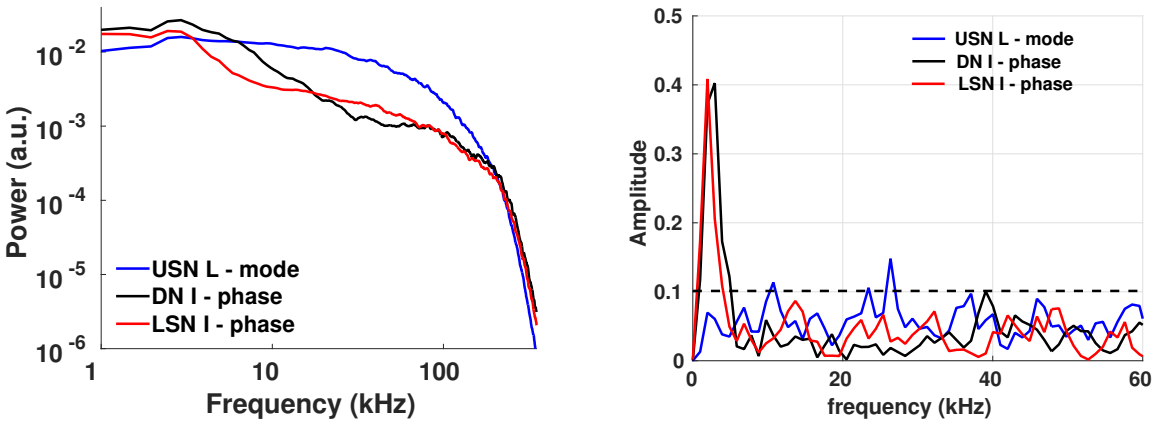

Figure 7.3: (a) Power spectra of Q-band LFS signal by FM-CW reflectometer at edge [ρ : $0.95 - 0.98$] for different magnetic configurations and confinement regimes from USN in L-mode to DN and LSN in I-phase, discharge #31634. (b) Cross-coherence of Q-band LFS signal and its envelope (estimated using fluctuations above 250 kHz) for the same time ranges. Dashed line corresponds to the coherence significance level.

high frequency components of density fluctuations, the envelope and cross-coherence analysis (see appendix A) is applied to the reflectometry data. This method has been used before for demonstrating that the high frequency density fluctuations can be modulated by low frequency

components (due to geodesic acoustic modes (GAMs), zonal flows or other meso-scale structures). Modulations is imprinted on the envelope of the microscopic fluctuations [204], assuming that it has a relation with the $E \times B$ velocity [205]. According to the methodology described in appendix A the envelope of $\delta n_e/n_e$ is obtained by applying the Hilbert transform to the high pass filtered signal (above 250 kHz) measured by reflectometry.

The cross-coherence between the envelope and the measured reflectometry homodyne signal probed at the LFS edge for time ranges corresponding to the different magnetic configurations is presented in Fig. 7.3b for discharge #31634. For time ranges corresponding to the I-phase an increased cross-coherence between measured signals and its envelope is observed indicating the presence of a $\delta n_e/n_e$ amplitude modulator with frequency < 5 kHz.

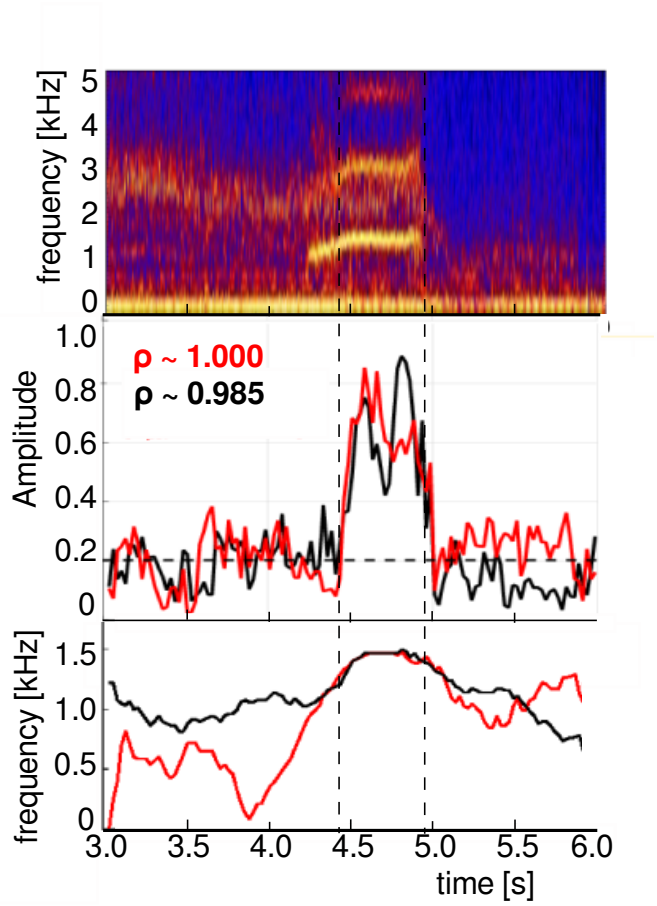

Figure 7.4: At the top spectrogram of signal by Mirnov coil B31-14 (upper divertor) displaying the LCOs presence with $f \approx 1.5$ kHz. Below there are time traces of the maximum cross-coherence between signals and its envelopes (above 250 kHz) measured by FM-CW reflectometer at the LFS edge and the separatrix. At the bottom, frequencies corresponding to the maximum of cross-coherence. Discharge #31633.

Figure 7.4 shows the evolution of the density fluctuations modulation - maximum of the cross-coherence and its corresponding frequency together with the spectrogram of the signal from a magnetic coil. The cross-coherence is estimated using a time windows of 25 ms implying

a significance level of ≈ 0.2. The LCOs are clearly seen in the magnetic signals (measured by a Mirnov coil B31-14) as a strong MHD activity at frequency $\approx$ 1.5 kHz with several harmonics. A strong modulation of the high frequency fluctuations (> 250 kHz) is observed at the edge, coinciding with the presence of the LCOs at the same frequency. Our results clearly indicate that the broadband density fluctuations at the LFS edge are modulated by the LCOs. This modulation is pronounced at $\rho_{pol,Q} \approx [0.96 - 0.985]$ and at $\rho_{pol,Ka} \approx [0.985 - 1.00]$ (estimated from Q and Ka signals, respectively), while it is not detected outside the separatrix.

7.3 Density fluctuations during LCOs

The above results reveal that edge density fluctuations are strongly modulated during I-phase by a $\sim$1.5 kHz frequency that correspond to LCOs as detected by the Mirnov coils. Here we analyze the modulations seen by reflectometry and its radial-temporal evolution along the LCOs. Figure 7.5 depicts Mirnov coil signals and reflectometry homodyne signals probing

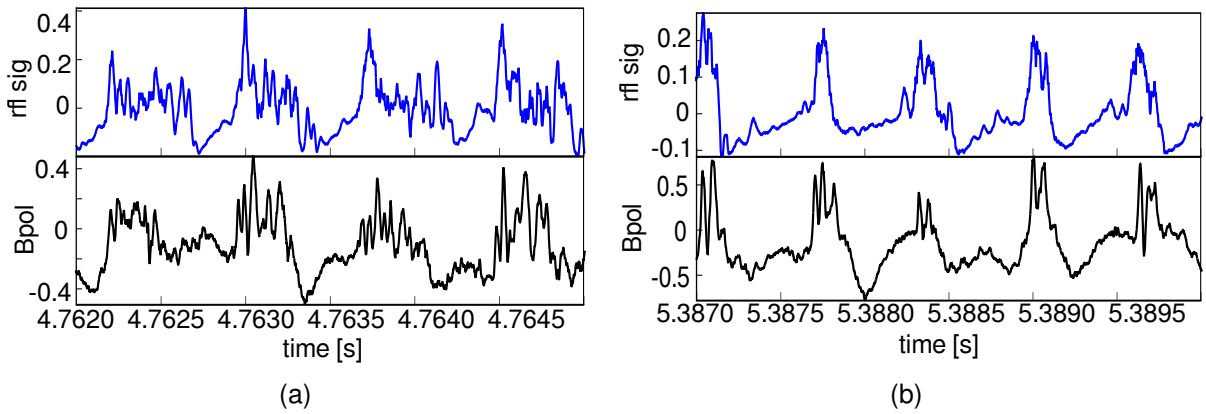

Figure 7.5: The time traces showing a short segments of the LCOs in discharge #31634. The LCOs are visible in the reflectometry Q-band signal at the LFS edge [$\rho : 0.95 - 0.98$] (top plot) and Mirnov coil B31-14 signal(bottom plot) for: (a) lower($\beta_N \approx 0.47$) and (b) higher ($\beta_N \approx 0.52$) confinement in I-phase.

plasma layers inside the separatrix (at $\rho_{pol} : 0.95-0.98$) obtained during the I-phase in discharge #31634 in two time intervals corresponding to: (a) low ($\beta_N \approx 0.47$) and (b) high ($\beta_N \approx 0.52$) confinement. Results show that low frequency modulations from reflectometry are in phase with the magnetic coil signals.

The LCOs and the associated pulsation are known to be characterized by periods with high shear/low fluctuations alternating with periods with high fluctuations as studied in detail at AUG [37–39, 206]. The fast changes of the reflectometry and Mirnov coils signals correspond to the fast switching between enhanced and reduced fluctuation states. The oscillations of the reflectometry signals can be associated with modulations of the edge density fluctuations

and/or oscillations of the plasma density profile.

In order to check if the fluctuations are modulated, the root-mean-square (RMS) of the reflectometry signals is considered. In Figure 7.6 are displayed a Mirnov coil signal and the RMS of the reflectometry signals from the Ka(red) and Q(blue) channels, probing densities $n_e \approx 0.97$ and $1.61 \cdot 10^{19}$ m^{-3}, corresponding to plasma layers located inside the separatrix at $\rho_{pol} \approx 0.99$ and 0.97, respectively. From the cross correlation analysis of the RMS reflectometry signals, a 30-50 μs delay is obtained indicating a radial propagation of the modulation of the density fluctuations by LCOs. This does not exclude that oscillations of the plasma density profile also contribute to the observed modulations.

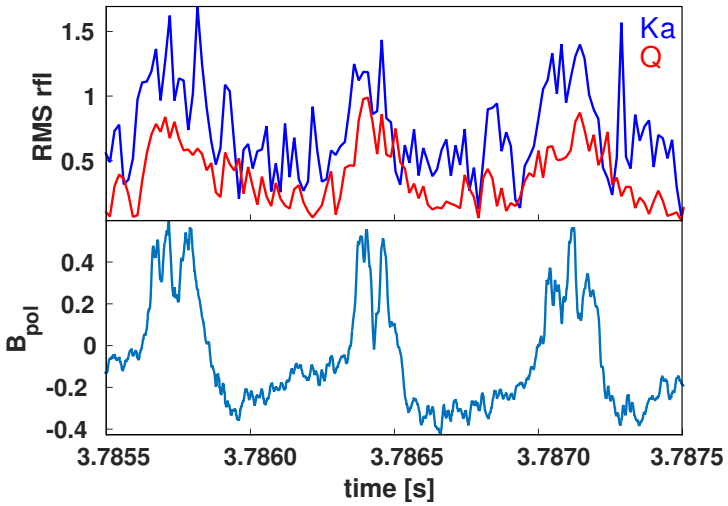

Figure 7.6: A short segment of the LCOs in discharge #31634. The modulation is visible in the RMS of reflectometry Ka and Q-band signals at the LFS edge ($\rho_{pol} \approx$ 0.97 and 0.99) (top plot), LCOs are presented by Mirnov coil B31-14 signal at upper divertor (second from the top) and in the inner and outer divertor currents (first and second plots from the bottom, respectively).

It should be noted that reflectometry and magnetic signals are not always in phase as can be seen from Figure 7.6. The phase difference between reflectometry signals and its envelope has been estimated for frequencies corresponding to the cross-coherence maximum as presented in Figure 7.7a. The estimation of the phase shift between reflectometry and magnetic signals (see Figure 7.7b) leads to similar values confirming the results based only on reflectometry data. It can be seen that the phase between the Ka- and Q-band signals for periods of high coherence (unshaded regions) is in the range from 0.5π up to π, suggesting an inward radial propagation of the density fluctuations associated with the LCOs, that is in agreement with results presented in Figure 7.6. As the probed layers measured by the both signals are separated by ≈ 1 cm and a delay between RMS of the signals of 30-50 μs was found, a radial propagation velocity of $\sim$200-300 m/s can be estimated, which is in a reasonable agreement with previous results obtained on AUG [37], in spite of different direction of propagation. In

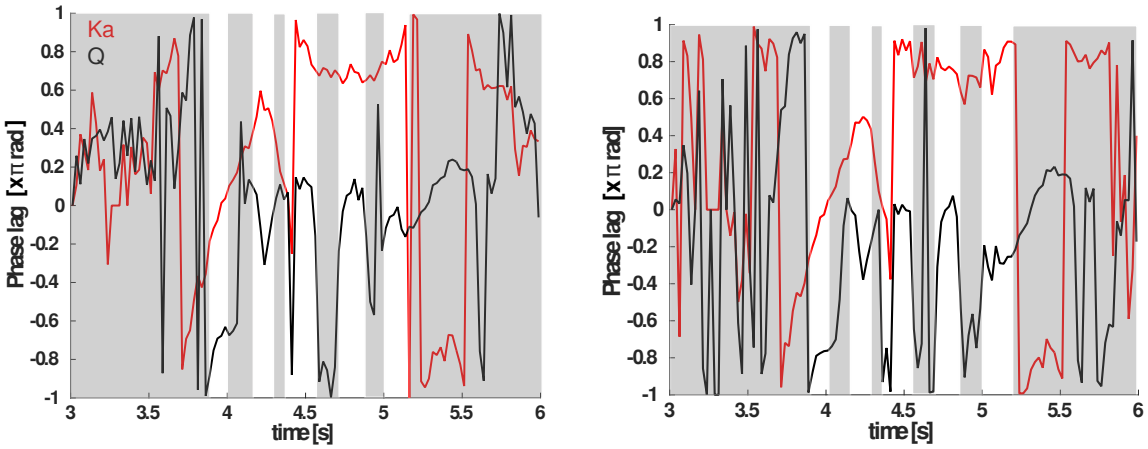

(a) reflectometry signals and its envelopes

(b) reflectometry and magnetic signals

Figure 7.7: Time traces of the cross spectrum phase for frequencies corresponding to maximum cross-coherence between: (a) Q-/Ka-band signals at the LFS and its envelopes (above 250 kHz) measured by FM-CW reflectometer at edge [$\rho : 0.94 - 0.98$] and [$\rho : 0.98 - 1.00$], respectively and (b) Q-/Ka-band reflectometry signals at the LFS and Mirnov coil B31-01 signal in discharge #31634. Unshaded regions correspond to time ranges when cross-coherence amplitude for both Ka and Q signals and its envelopes is higher than 0.6.

ref. [37] a modulation in the density profile starting inside the separatrix and propagating outward with a radial velocity in the order of $100-300$ m/s into the far SOL layer was described. On TJ-II stellarator oscillations associated with the L-H transition were also studied [207], where an inward and outward radial propagation velocity of the oscillation pattern of density fluctuations inside the separatrix in the range of $50 - 200$ m/s was characterized.

7.4 Summary and discussion

In this chapter it was investigated, the magnetic signature of LCOs (during the I-phase of ASDEX Upgrade plasmas) in the density fluctuations at the very edge of the confined region at the LFS. The high frequency density fluctuations ($>$ 250 kHz) inside the separatrix ($0.95 < \rho_{pol} < 1$) were shown to follow the magnetic field perturbations being modulated by ~ 1.5 kHz that correspond to the frequency of LCOs inherent to the I-phase. The modulation is not radially uniform, and propagates inward with an estimated velocity of $\sim 200 - 300$ m/s. This value is similar to the velocity obtained previously at AUG with Li beam and Doppler reflectometry [37], as well as at TJ-II with Doppler reflectometry [207]. The observation that the modulation does not occur simultaneously across the edge suggests that suppression/enhancement of turbulence is not radially uniform.

It was reported at AUG, that the magnetic fluctuations during the I-phase can be caused by the relaxation current due to ballooned transport resembling the Stringer spin-up [38], where

in-out asymmetry is considered to play a prey role (while the up-down asymmetry is a predator [208]). In the analyzed discharges in I-phase the HFS density profiles become much steeper than at the LFS, the HFS and the LFS density profiles display a strong asymmetry. Profiles at the HFS become much steeper than at the LFS, causing the HFS probed density layers to move outwards into the SOL, thus preventing fluctuations to be measured at edge.

As the mechanism causing the I-phase is not yet completely understood, further investigation of the density fluctuations in LCOs is needed. It should include HFS/LFS comparative studies at the same normalized radial location in order to estimate the in-out asymmetry. Future experiments to study HFS/LFS fluctuations asymmetry should be focused in low density ($n_e \lesssim 3 \cdot 10^{19}$ m^{-3}) discharges with symmetric HFS/LFS density profiles enabling to probe edge plasma layers at both sides.

Chapter 8

Turbulence in different divertor states

> "It would be so nice if something made sense for a change."
>
> — Lewis Carroll, Alice in Wonderland

Observations from a large number of tokamak experiments provide clear evidence that the turbulence drive is ballooning-like, favoring the outboard plasma region [66, 86, 92, 95–97, 99–101, 104]. However, most of the present knowledge of turbulence comes from measurements at the low-field-side (LFS) scrape-off layer (SOL), while data from the high-field-side (HFS) is scarce and is needed to evaluate the poloidal variations that are essential to draw further conclusions about the turbulent transport [43, 47, 113]. Simultaneous fluctuation measurements at the LFS and the HFS midplane will be essential to characterize edge turbulence and to investigate a possible link between midplane and divertor conditions.

In this chapter the density fluctuations and their poloidal asymmetries are studied at ASDEX Upgrade tokamak in L-mode density ramp discharges where divertor conditions evolve from attached to completely detached (see section 4.3). These discharges are characterized by the development of a high-field-side high density (HFSHD) region [10] associated with detachment of the inner divertor that expands up to the midplane [108], leading to strong poloidal asymmetries in the SOL density, which are studied in detail in Ref. [109]. Also, at the beginning of outer divertor detachment an enhanced cross-field transport has been reported at AUG LFS leading to a flatter density profile [11, 131, 209, 210]. Heretofore, the dependence of turbulence along the detachment has been studied mainly at the LFS, while the HFS may also be influenced by the divertor conditions. Motivated by the relevance of characterizing turbulence at both sides to investigate the possible influence of varying SOL boundary conditions and accompanying enhanced filamentary transport, we use here the unique capabilities of the ASDEX Upgrade (AUG) reflectometry diagnostic able to measure density fluctuations simultaneously at both the

LFS and the HFS.

8.1 Evolution of density profiles during the divertor detachment

Density ramp-up discharges were performed in a standard lower single null (LSN) magnetic configuration with the ion ∇B drift towards the X-point by increasing the deuterium gas injected while maintaining constant levels of additional heating power. Following the density ramp-up, the divertor evolves from attached to detached regime. The detachment process undergoes three different detachment states: onset, fluctuating and complete detachment state that are described in section 4.3. In Figure 8.1 are displayed density profiles at the HFS and the LFS representative of the three divertor states.

As the plasma parameters evolve slowly (typically on the timescale of seconds), the reflectometry profiles (measured each 1 ms) were averaged over 250 ms (250 profiles). The time intervals where profiles were measured are indicated in the Figure 8.1 caption. The dashed lines indicate the three density layers probed for fluctuation measurements, which move outwards both at the HFS and the LFS as a consequence of the profile evolution. The density profiles provide not only the variable location of the probed layers but also the local density gradients that is needed for the estimation of the density fluctuation amplitudes (see section 3.5).

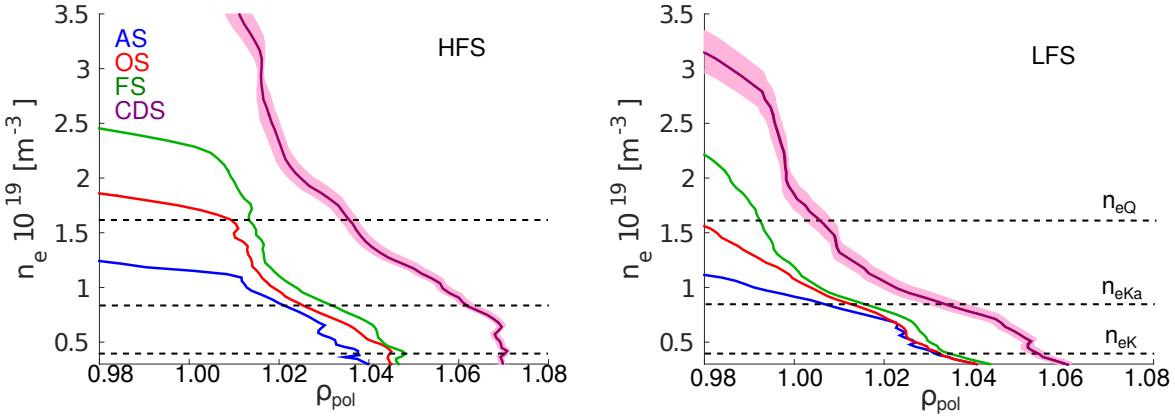

(a) HFS (b) LFS

Figure 8.1: Density profiles from reflectometry at (a) the HFS and (b) the LFS in different divertor detachment states in discharge #33483. Profiles are averaged over 250 ms. Time intervals for profile averaging are: (i) AS [1.75−2.0 s]; (ii) OS [2.15−2.4 s]; (iii) FS [2.4−2.65 s], (iv) CDS [3.35−3.6 s]. Probed density layers in K, Ka and Q frequency ranges used in the paired discharge #33484 are indicated by dashed lines. The shadow regions around the profiles in CDS indicate standard deviation of 250 profiles (corresponding to the selected 250 ms time ranges).

For low line-average densities corresponding to the initial attached state ($t < 2.1$ s), the

density profiles are roughly HFS/LFS symmetric (Fig. 8.1). After $t \approx 2.1$ s the inner divertor detaches and the profiles become poloidally asymmetric as a consequence of a strong increase of the SOL density at the HFS. This increase is particularly strong towards the later phase of the discharge as a consequence of the development of the HFSHD region [109]. At the LFS, a pedestal-like structure is formed near the separatrix starting around the fluctuating state, following the increase in the core and edge line-averaged densities (see Figure 8.1). During complete detachment, the LFS density profile broadens with the flatten region extending up to $\rho_{pol} \approx 1.05$), as was previously observed by the lithium beam and the reciprocating Langmuir probe diagnostics at AUG [11]. This flattening was shown to occur when a certain divertor collisionality is surpassed leading to an increase of the convective transport caused by plasma filaments [11, 131, 209, 210].

8.2 Radial profiles of the density fluctuations at the LFS and the HFS

Fluctuation data from reflectometry were compared with similar data from a reciprocating probe available at the LFS mid-plane measuring, among other parameters, the ion saturation current ($I_{sat} \propto n_e(T_e + T_i)^{1/2}$) at the same acquisition rate (2 MHz) as reflectometry [165].

An absolute comparison of density fluctuations at the HFS and the LFS can be derived from the phase of the reflected signals at low line-averaged densities or in other cases where the filtering out of the low frequency components does not hamper the analysis of the density fluctuations (as described in section 3.5). Figure 8.2 displays the radial evolution of density fluctuations at edge and SOL regions estimated from the FM-CW homodyne phase in discharge #33484. Data were obtained in the initial part of the discharge when the edge line-averaged density is low ($\bar{n}_e \leq 1.5\ 10^{19}$ m^{-3}). Also displayed in the figure is the fluctuation amplitude by the reciprocating Langmuir probe inferred from [11] in similar experimental conditions. The density fluctuation amplitudes are seen to increase radially at both the LFS and the HFS as it is typically observed in fusion plasmas [43, 97]. Levels in the confined region are found to be as low as $\approx 2\ \%$ while in the near SOL they range from $15-25\ \%$ on the LFS and from $5-15\ \%$ on the HFS. The lower values of $\delta n_e/n_e$ in the HFS SOL (by a factor of ≈ 2) is consistent with ballooned transport. Radial profile of density fluctuations from reflectometry at the LFS matches quite well the Langmuir probe results (taking into account an expected pronounced increase of density fluctuations towards the far SOL [43]) and that density fluctuations by the reciprocating probe were estimated from the ion saturation current measurements ignoring the

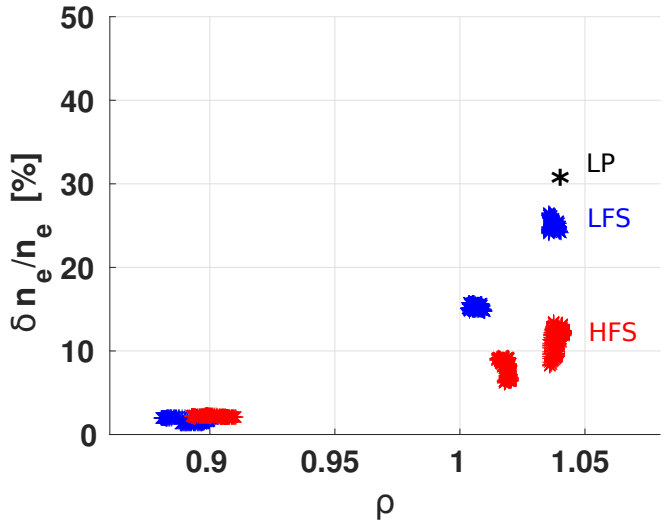

Figure 8.2: Radial profiles of $\delta n_e/n_e$ at the LFS and the HFS obtained from FM-CW reflectometry in discharge #33484 with an edge line-averaged density of $\bar{n}_e \approx 1.3 \cdot 10^{19}$ m^{-3}. The location of the probed layers is measured with the FM-CW system operated in profile mode in the paired discharge #33483. The star symbols indicate values of $\delta n_e/n_e$ estimated from the reciprocating Langmuir probe data at the LFS in similar experimental conditions [11].

contribution of temperature fluctuations.

8.3 Density fluctuations at the LFS SOL

For the analysis of the density fluctuations along with detachment we first consider the LFS and later (in section 8.5) the HFS. From now on we use the standard deviation of the homodyne reflected signals due to the relevance of the low frequency components of fluctuations (that would be filtered out under Hilbert transform approach), as explained in chapter 5. Therefore the density fluctuation results are presented in arbitrary units.

The evolution of the density fluctuations in the LFS SOL for discharge #33484 (characterized in section 4.3) is depicted in Figure 8.3. Data was estimated using a sliding window of 5 ms. Also shown is the location along the discharge (from $\rho_{pol} 1.04$ to 1.06) of the probed layer with $n_e = 0.40 \cdot 10^{19}$ m^{-3} (from K-band reflectometry channel). The increasing trend (up to $t \approx 3.5s$) of the amplitude of the density fluctuations at the LFS SOL is observed, as expected due to the combined effects of the outward shift of the probed layer and the rising line-averaged density. Indeed, data from a larger number of experiments indicate that density fluctuations usually increase with line-averaged density and with radius [43]. Unexpectedly, for $t > 3.5$s during CDS, despite the continuous increase of the edge line-averaged density, the density fluctuations do not vary significantly and a modest evolution of the density profiles is observed, as can be inferred from the unchanged location of the probed layer. Apart from the general

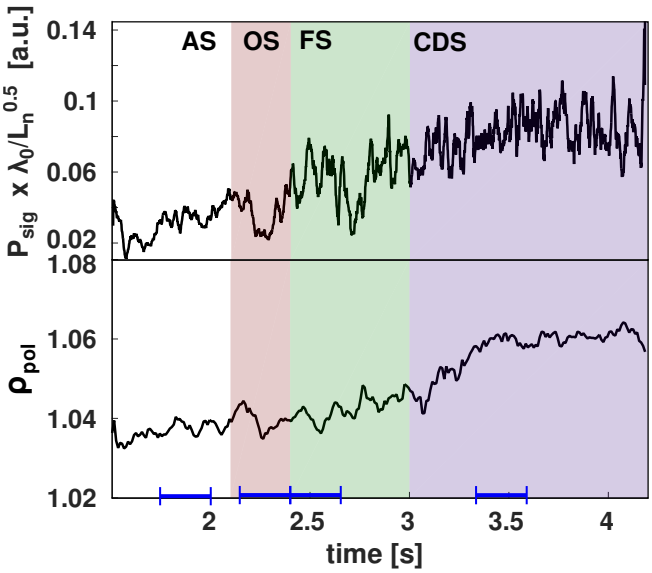

Figure 8.3: Time traces of the standard deviation of the FM-CW reflectometer K band signal in the LFS SOL multiplied by $\sqrt{\lambda_0/L_n}$, where λ_0 is the vacuum wavelength and L_n the density gradient length. The variable location of the probed layer is shown at the bottom. Divertor detachment states AS, OS, FS and CDS are indicated by the color blocks. The time intervals ($\Delta t = 250$ ms) shown in blue indicate the periods used to estimate the average properties of density profiles and fluctuations in each detachment state.

increasing trend throughout the discharge, fluctuations at the LFS SOL display features such as oscillations that coincide with the changes in the divertor conditions (such as, for example, divertor oscillations [10] occurring at the FS for $t = 2.4 - 3.0$s).

The radial profiles of the density fluctuations

The radial profiles of the density fluctuations $\delta n_e/n_e$ and the non-normalized fluctuations δn_e (obtained by multiplying $\delta n_e/n_e$ and by the probing density n_e) in the LFS SOL for discharge #33484 (characterized in section 4.3) for each divertor state were estimated from data obtained at three density layers, $n_e = 0.4$, 0.84 and 1.61×10^{19} m^{-3}, using a 42.5 ms time window (during this time range the line-averaged density varies by $< 5\%$). Results are displayed in Figure 8.4, where the color of the points indicates the divertor state. The locations of each probed layer were obtained from the reflectometry density profiles also averaged over 42.5 ms. As the probing densities are fixed the radial coverage changes following the profile dynamics.

Relative density fluctuations $\delta n_e/n_e$ are seen to increase with radius for all the divertor states (Figure 8.4). Changes with the density along the discharge seem to depend on ρ_{pol} locations. Close to the separatrix ($\rho_{pol} \approx 1.00$), density fluctuations do not display significant changes with the divertor state, while at $\rho_{pol} \approx 1.04$ density fluctuations increase along the evolution of divertor from the attached towards the complete detachment state. In the completely

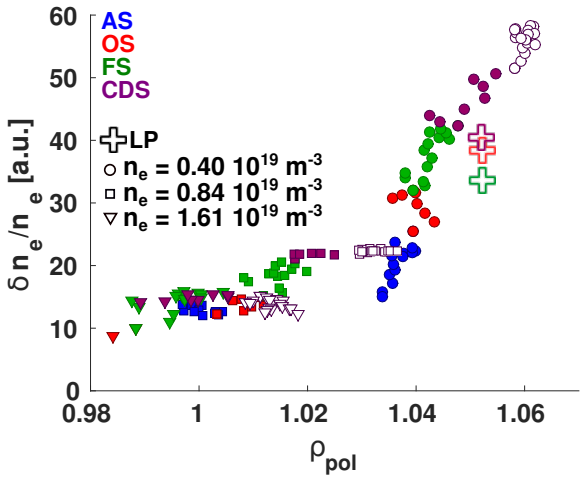

Figure 8.4: LFS SOL: radial profiles of $\delta n_e/n_e$ density fluctuations obtained using the standard deviation of the homodyne signal from FM-CW reflectometry in K-, Ka- and Q-bands. Data were measured in discharge #33484 and were estimated using a 42.5 ms time window. Color of points corresponds to the different divertor states: attached (blue), onset (red), fluctuating (green) and complete detachment state (purple, closed symbols attributed to the beginning of the state from 3 to 3.35 s, open circles to the later part of the state). Symbols correspond to different probed densities: $n_{eK} = 0.40 \cdot 10^{19}$ m^{-3} (circles), $n_{eKa} = 0.84 \cdot 10^{19}$ m^{-3} (squares) and $n_{eQ} = 1.61 \cdot 10^{19}$ m^{-3} (triangles). Cross symbols correspond to the density fluctuations estimated using the ion saturation current I_{sat} signal measured by the reciprocating Langmuir probe in the similar discharge #30303.

detached state, the radial coverage is extended towards the far SOL ($\rho_{pol} \approx 1.06$) due to the density profile outward shift (see Figure 8.1), which hampers the comparison with fluctuations in the other detachment states. For the comparison with other detachment states, we use here density fluctuation levels of the ion saturation current signal from the reciprocating Langmuir probe for a similar density ramp discharge (#30303), measured at $\rho_{pol} \approx 1.05-1.055$ in three successive plunges during the onset, the fluctuating and the complete detachment state. At this location the dependence of the I_{sat} fluctuation level on the density is modest, with a lower value seen in the fluctuating state. Our results suggest therefore that density fluctuation levels have a modest dependence on the line-averaged density in the near and far SOL regions, contrary to the observation around $\rho_{pol} \approx 1.04$ where density fluctuations increase along with the density ramp. Non-normalized density fluctuations δn_e depicted in Figure 8.5(obtained by multiplying the data in Figure 8.4 by the probing density value, see Figure 8.5) are seen to decrease with radius in the near SOL that can be associated with parallel transport losses. In the later phase of the complete detachment state δn_e display an increase in the far SOL, which can not be attributed to the change of the characteristics of the filaments. However, it may be associated with other sources of density perturbations for instance resulting from fast variations in the divertor condition. Finally, it cannot be excluded that at such high level of fluctuations in

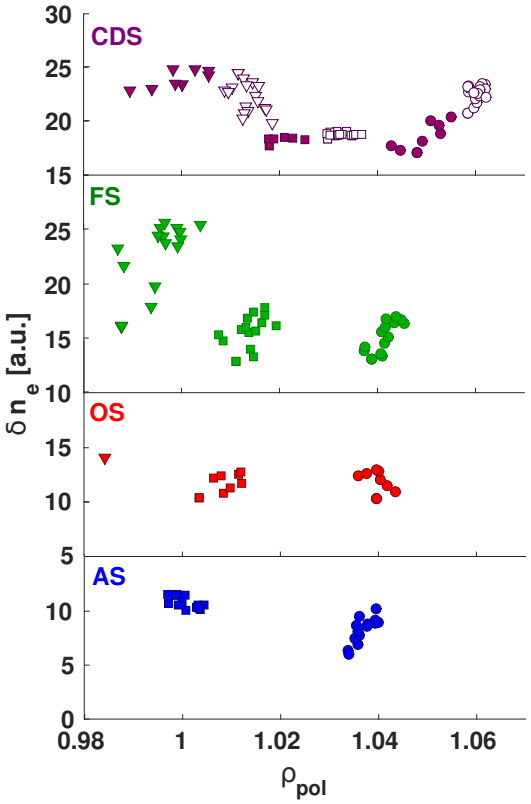

Figure 8.5: LFS SOL: radial profiles of non-normalized δn_e density fluctuations obtained by multiplying $\delta n_e/n_e$ (Figure 8.4) to the probing densities. Symbols correspond to different probed densities: $n_{eK} = 0.40 \cdot 10^{19}$ m^{-3} (circles), $n_{eKa} = 0.84 \cdot 10^{19}$ m^{-3} (squares) and $n_{eQ} = 1.61 \cdot 10^{19}$ m^{-3} (triangles). In the complete detachment state (the top plot), closed symbols are attributed to the beginning of the state from 3 to 3.35 s and open circles to the later part of the state.

the far SOL, 2D and 3D propagation effects might play a role, which is not considered in the data analysis.

8.4 Frequency-resolved analysis of density fluctuations

A first picture of the typical density fluctuations at each divertor state can be inferred from the time traces of I_{sat} obtained by the reciprocating Langmuir probe in three successive plunges in discharge #30303 as displayed in Figure 8.6. At the onset state, fluctuations are characterized by fast, low amplitude fluctuations while during complete detachment large I_{sat} spikes are seen that are associated with filaments, which become significantly larger and less frequent. In the fluctuating state the amplitude of the filaments increases with respect to the onset state and pronounced low frequency oscillations are superimposed possibly related to the oscillations in the divertor conditions [10]. The increase of filamentary activity along the discharge can be quantified by the skewness of the fluctuations for the different divertor states: the values are about 0.3, 0.5 and 1.1 in the onset, fluctuating and complete detachment state, respectively.

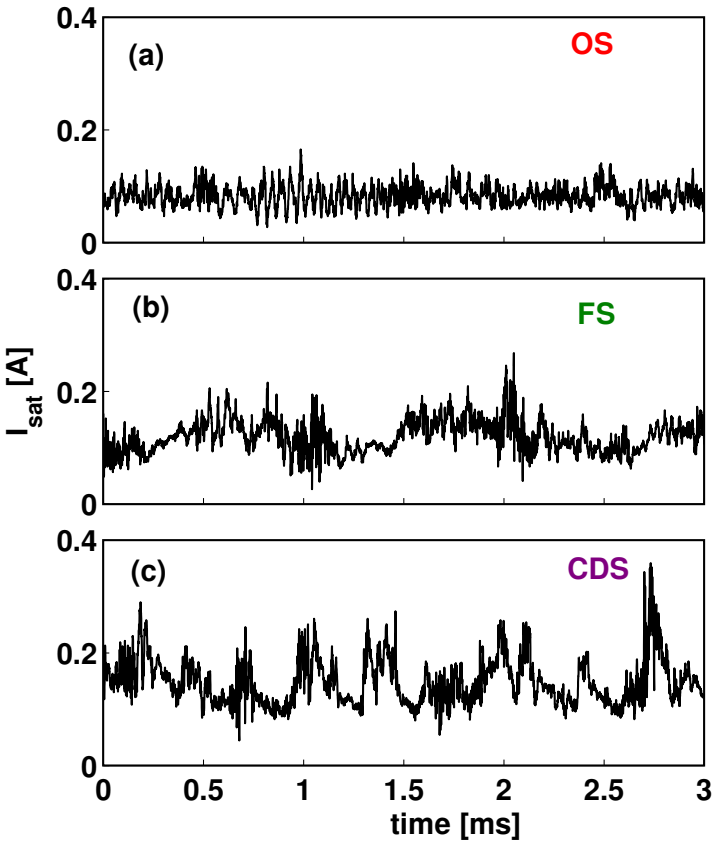

Figure 8.6: Ion saturation current time traces obtained by the reciprocating Langmuir probe for [ρ_{pol} : $1.050 - 1.054$] in 3 ms periods during 3 plunges corresponding to the (a) onset, (b) fluctuating and (c) complete detachment states in discharge #30303.

To characterize the dominant frequency components of the midplane fluctuations along the divertor detachment, we present the evolution of the fluctuation power spectra from reflectometry probing the far SOL layer at the LFS [ρ_{pol}: 1.04−1.06], as shown in Figure 8.7 (left). For

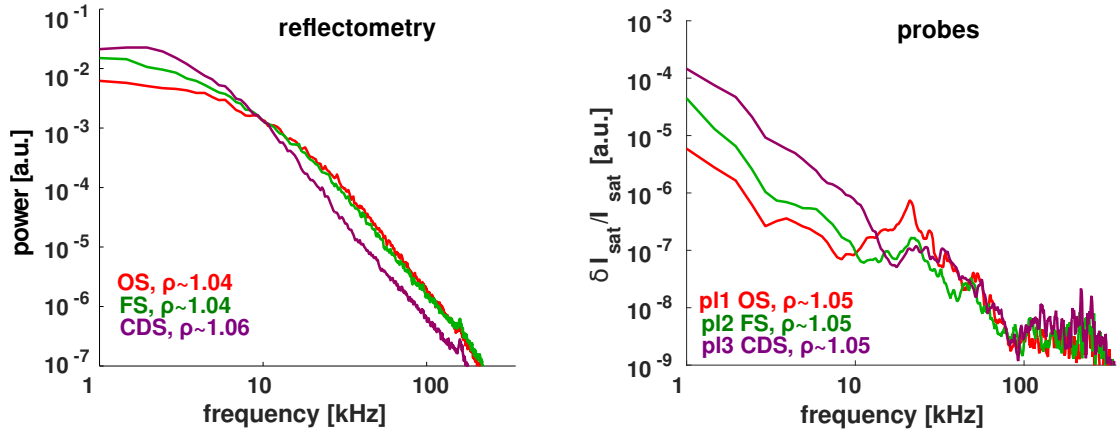

Figure 8.7: At the left power spectra of the K-band LFS homodyne signal measured by the FM-CW reflectometer in the SOL [$\rho_{pol} = 1.04-1.06$] in onset, fluctuating and complete detachment states during discharge #33484; at the right power spectra of the ion saturation current measured by the reciprocating Langmuir probe at the mid-plane LFS SOL in the similar discharge #30303 during the same detachment states.

comparison, Figure 8.7 at the right depicts the power spectra from the I_{sat} signal measured by the reciprocating Langmuir probe at $\rho_{pol} \approx 1.05$. Fluctuations with a broad frequency spectrum are obtained from both diagnostics showing that the increase of the fluctuation amplitude described above (see Figure 8.4) results mainly from an increase of the low frequency components ($f < 15$ kHz).

As indicated by the time traces of the ion saturation current from the reciprocating probe (see figure 8.6), the increase of low frequency components in the fluctuating state is associated with both filaments and low frequency oscillations at the midplane, while in the complete detachment state the increase should result mainly from the increase in the filamentary activity. Indeed, during the complete detachment state fluctuations are dominated by large, infrequent filaments lasting more than 0.1 ms (see figure 8.6) in good agreement with the frequency range where the power spectrum is observed to increase. We can therefore conclude that the increase in the low frequency fluctuations measured by reflectometry at the LFS SOL is due to an increase of filamentary activity. The decrease of the high frequency ($f > 15$ kHz) components seen during the CDS in the power spectra from reflectometry can not so far be explained requiring further investigation based on measurements with better spatial resolution.

8.5 Density fluctuations at the HFS SOL

We turn now our attention to the behavior of the fluctuations at the HFS. HFS/LFS asymmetries

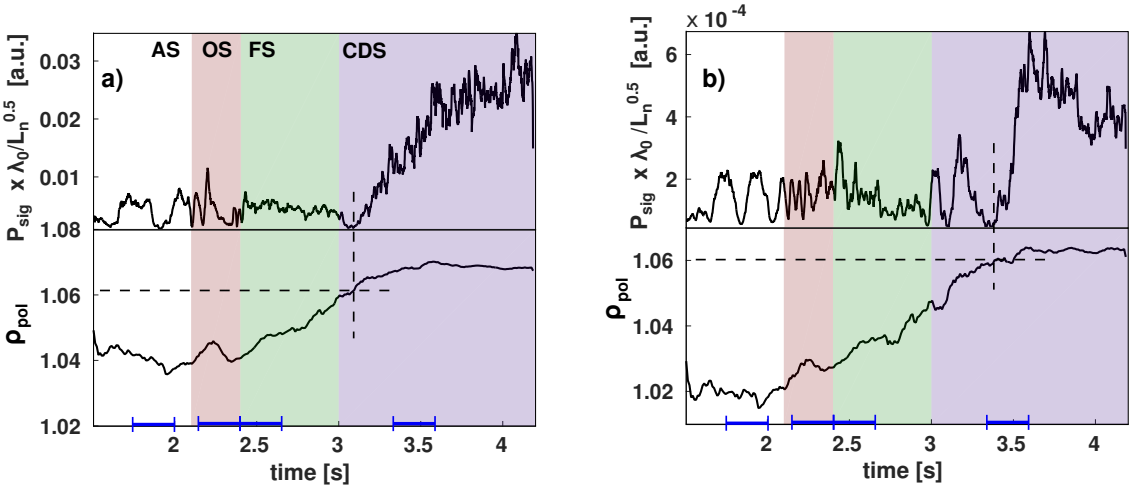

Figure 8.8: Time traces of the standard deviation of the FM-CW reflectometer signals from (a) the K- and (b) the Ka-band at the HFS SOL in discharge #33484 multiplied by $\sqrt{\lambda_0/L_n}$ inferred from the paired discharge #33483. The variable location of the probed density layers n_{eK} and n_{eKa} is shown at the bottom of each plot. Divertor detachment states (AS, OS, FS and CDS) are indicated. The time intervals $\Delta t = 250$ ms shown in blue indicate the periods used to estimate the average properties of density profiles and fluctuations in each detachment state.

are expected as a consequence of ballooned transport in the SOL. The link between the LFS and the HFS SOL and the possible influence of the divertor conditions will also be investigated.

Figure 8.8 presents the evolution of the relative density fluctuations at the HFS SOL in discharge #33484 derived from reflectometry signals probing the density layers (a) $n_{eK} = 0.40 \cdot 10^{19}$ m^{-3} (K-band) and (b) $n_{eKa} = 0.84 \cdot 10^{19}$ m^{-3} (Ka-band). The locations of the two probed layers are displayed in the two lower plots. As illustrated in Figure 8.8, there is no clear trend of density fluctuations behaviour at the HFS SOL until the complete detachment state, where the most pronounced changes are observed. In particular, fluctuations at the HFS do not increase in the fluctuating state contrary to the LFS, where an enhancement of filamentary transport and low frequency oscillations are observed (Figs. 8.4 and 8.6).

During complete detachment, however, the situation changes and the relative density fluctuations on the HFS start to increase significantly when the probed density layer reaches a certain radial location in the far SOL ($\rho_{pol} \approx 1.06$). This justifies why the increase of fluctuations is seen first at the K-band n_{eK} (for $t \approx 3.05$ s) and later at the Ka-band signal n_{eKa} (for $t \approx 3.40$ s). The radial profiles of the density fluctuations for the different divertor states shown in Figure 8.9 (obtained with a 42.5 ms time window from K-, Ka- and Q-band data), confirm the modest evolution of the HFS fluctuations until complete detachment is reached and a weak radial variation up to $\rho_{pol} \approx 1.06$. During the complete detachment state, density fluctuation profiles exhibit a sharp increase in the far SOL ($\rho_{pol} \approx 1.06$).

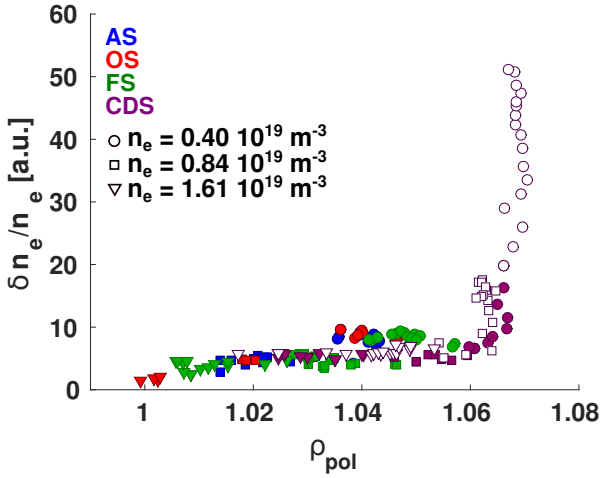

Figure 8.9: HFS SOL: radial profiles of relative $\delta n_e/n_e$ density fluctuations obtained using the standard deviation of the homodyne signal from FM-CW reflectometry in K-, Ka- and Q-bands. Data were measured in discharge #33484 and were estimated using a 42.5 ms time window. Color of points corresponds to the different divertor states: attached (blue), onset (red), fluctuating (green) and complete detachment state (purple, closed symbols attributed to the beginning of the state from 3 to 3.35 s, open circles to the later part of the state). Symbols correspond to different probed densities: $n_{eK} = 0.40 \cdot 10^{19}$ m^{-3} (circles), $n_{eKa} = 0.84 \cdot 10^{19}$ m^{-3} (squares) and $n_{eQ} = 1.61 \cdot 10^{19}$ m^{-3} (triangles).

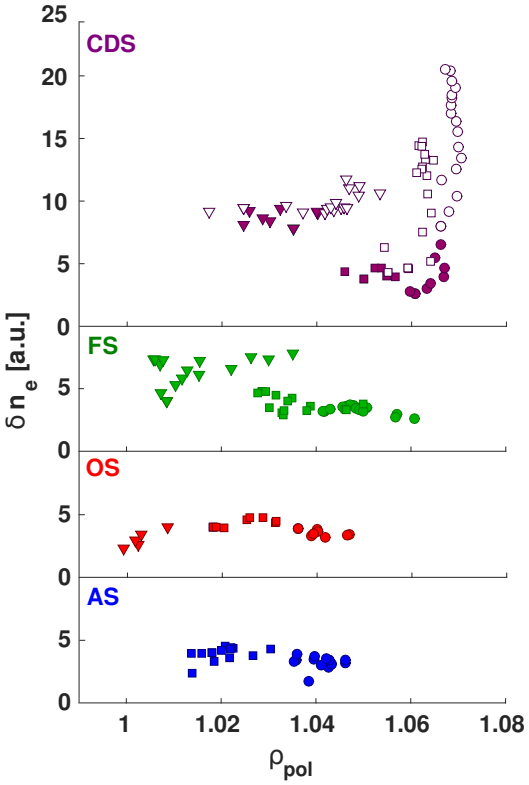

Figure 8.10: HFS SOL: radial profiles of non-normalized δn_e density fluctuations obtained by multiplying $\delta n_e/n_e$ (Figure 8.9) to the probing densities. Symbols correspond to different probed densities: $n_{eK} = 0.40 \cdot 10^{19}$ m^{-3} (circles), $n_{eKa} = 0.84 \cdot 10^{19}$ m^{-3} (squares) and $n_{eQ} = 1.61 \cdot 10^{19}$ m^{-3} (triangles). In the complete detachment state (the top plot), closed symbols are attributed to the beginning of the state from 3 to 3.35 s and open circles to the later part of the state.

It was previously shown at AUG [11] that during complete detachment the radial velocity of the filaments increases, leading to broad density profiles at the LFS. As filaments are generated around the LFS midplane and propagate along the field lines they are expected to reach the far SOL at the HFS. Assuming a typical radial velocity of 300 m/s characteristic of the complete detachment state [11] and propagation at sound speed along the field lines, filaments should be detected in the HFS far SOL around $\rho_{pol} \approx 1.1$. This is further out than observed but still in reasonable agreement with the experimental findings from reflectometry, taking into account that the radial velocity of filaments coming from the LFS midplane, may not be constant radially across the SOL and also they can be originated at the top of the LFS resulting in shorter paths to the HFS midplane. The fact that non-normalized density fluctuations depicted in Figure 8.10 increase in the far-SOL gives further evidence that these fluctuations are not due to local radial transport but rather to parallel transport originated at the LFS. Therefore, we suggest that under certain divertor conditions, such as occurring during the complete detachment state, the HFS SOL may be strongly influenced by the presence of the turbulent structures coming from the LFS.

8.6 Summary

Results from reflectometry reveal that density fluctuation levels on the LFS have a modest dependence on the line-averaged density close to the separatrix at $\rho_{pol} = 1.00-1.01$ and also around $\rho_{pol} = 1.05$ as seen from the reciprocating Langmuir probe data. This is in contrast to the observations around $\rho_{pol} = 1.04$ where density fluctuations from reflectometry increase along with the density ramp. The increase of density fluctuation levels in the complete detachment state results mainly from an increase of the low frequency components (< 15 kHz) also observed in the reciprocating Langmuir probe data that is in agreement with the generally accepted view that radial transport at the LFS SOL is dominated by the filamentary activity. As the plasma density is ramped-up, less frequent and faster filaments are observed when a density shoulder is formed at the LFS [11].

When filaments become faster and less frequent at the LFS, relative density fluctuations at the HFS strongly increase in the far SOL region ($\rho_{pol} > 1.06$), which may be interpreted as a presence of faster filaments that propagate parallel to the magnetic field lines from the LFS to the HFS. Although the present spatial coverage of FM-CW reflectometry at high density is limited, results indicate that under certain divertor conditions, such as occurring in the complete detachment state, the HFS SOL can be strongly influenced by the presence of turbulent structures originated at the LFS. However, due to the lack of data we cannot conclude if some of the changes, for example the decrease of the high frequency components of the density fluctuations during complete detachment, can be attributed to the radial variations of the probing layers or to the evolution of the fluctuations. This requires further investigation that would benefit from an increased spatial coverage using additional probing frequencies in an upgraded FM-CW diagnostic.

This work presents for the first time at AUG simultaneous measurements of the density fluctuations at the HFS and the LFS that provide a consistent picture of the poloidal asymmetry in the density fluctuations as well as of the influence of the divertor conditions on the midplane density fluctuations. The capability of FM-CW reflectometry to measure simultaneously both at the LFS and the HFS opens the way to address key topics such as the link between the inboard and outboard plasma regions. This can contribute towards achieving a global picture of the SOL transport characteristics in fusion devices.

Chapter 9

Conclusions and outlook

"Science is not only a disciple of reason
but, also, one of romance and passion."

— Stephen Hawking

This thesis aimed at studying the edge ($\rho < 1$) and SOL turbulence and its poloidal asymmetries at ASDEX Upgrade tokamak. The study of edge/SOL plasmas in tokamaks is of great importance because the anomalous radial cross-field transport causes the dominant losses of energy and particles thus limiting the effectiveness of a fusion reactor. It is generally accepted that anomalous perpendicular transport is caused by plasma turbulence, so understanding turbulence properties in the edge/SOL plasmas is crucial to build a future magnetic fusion reactor. Edge turbulence is known to be ballooned and therefore it is also important to investigate its poloidal asymmetries.

The study use as main diagnostic the FM-CW O-mode reflectometer installed at AUG midplane, able to measure density fluctuations and density profiles with high spatial/temporal resolution, both at the HFS and the LFS. A methodology was developed to extract the phase from the homodyne reflectometry signal, which is a key information to estimate the level of density fluctuations, $\delta n_e/n_e$.

Experiments were performed in plasma conditions where the edge/SOL turbulence should undergo significant changes, namely (i) plasmas with LSN, USN and DN magnetic configurations displaying different connections between the HFS and the LFS. Once the magnetic configurations differ mainly at the edge/SOL, turbulence should be modified mostly in those regions. Turbulence changes in L-mode (USN versus LSN) and I-phase (DN versus LSN) were also characterized. As USN and LSN topologies display different power thresholds for the L-H transition, the comparative study has the potential to provide important information about the edge pre-requisites for the transition from L- to H-mode; (ii) in I-phase we analyze the influence

of the LCOs in the midplane turbulence, which can as well contribute to understand the L-H transition. Dedicated simulations by GEMR code were performed in support of the experiments with different magnetic configurations; (iii) L-mode density ramp discharges where divertor conditions evolve from attached to completely detached. These discharges are characterized by enhanced cross-field transport at the LFS and a flattening of density profile at the beginning of outer divertor detachment [11, 51, 131, 209]. So, it is expected that filamentary transport at the SOL depends on the divertor conditions and may influence the midplane turbulence. Heretofore, the dependence of turbulence along detachment has been studied mainly at the LFS, while the HFS may also be influenced by the divertor conditions. In these discharges we investigate the possible influence of varying SOL boundary conditions and accompanying enhanced filamentary transport at both sides.

Conclusions

Methodology to estimate the level of fluctuations from the homodyne reflectometry signal:

The FM-CW reflectometry system has homodyne detection providing output signals with non-separable amplitude and phase components. To extract the phase, which is a key information to estimate $\delta n_e/n_e$, a method was developed using the Hilbert transform. The procedure was validated by comparison with the phase data (LFS, edge and SOL) from the fast frequency hopping (FFH) reflectometer at AUG, installed at the LFS and equipped with I/Q heterodyne detection providing phase directly. The fluctuation levels from the homodyne FM-CW signal are in good agreement with similar data from Langmuir probe at the LFS SOL.

The possibility to obtain the level of density fluctuations from the FM-CW system is a relevant achievement (the FM-CW system is the only system that can measure $\delta n_e/n_e$ at both the HFS and the LFS) due to the importance of measuring density fluctuation at the HFS where data is scarce or non existing and also to study the poloidal asymmetries of turbulence.

USN and LSN magnetic configurations (L-mode):

Radial profiles of density fluctuation levels from reflectometry were obtained using the above methodology. In the LSN topology mostly used at AUG $\delta n_e/n_e$ increase with radius both at the HFS and the LFS. At the HFS, the fluctuation levels (at separatrix) are lower by a factor of $\sim$2, which is consistent with the dominant ballooning-like transport. Power spectra of fluctuations are narrower at the HFS than at the LFS, both inside and outside the separatrix, in agreement with results from Alcator C-Mod obtained at the SOL. Profiles of density fluctuations in USN increase also with radius at both the HFS and the LFS. Pronounced poloidal asymmetries of

density fluctuations are seen both in LSN and USN topologies. At the SOL for both configurations, the typical ratios LFS/HFS of density fluctuation levels, are ∼2 (for $\rho \approx 1.02$), which is consistent with a dominant ballooning-like transport. At the edge (for $\rho < 1.00$), density fluctuation levels are similar in both configurations, while for $\rho > 1.00$, in USN $\delta n_e/n_e$ are lower than in LSN by a factor of ∼2 (at $\rho \approx 1.02$), both at the LFS and the HFS. The lower density fluctuation levels found in USN, are in agreement with numerical results obtained with the gyrofluid GEMR code and also with experimental results obtained in other tokamaks such as Alcator C-Mod (at the LFS SOL for ≈ 1 cm from separatrix) [97] and at DIII-D (at the LFS edge for $\rho : 0.90 - 1.00$) [119]. However, no explanation has so far been found. USN is characterized by a higher power threshold of the L-H transition, therefore lower fluctuation levels of fluctuations may seem contradictory. At AUG, the difference of density fluctuation levels, cannot be attributed to density gradients once they are similar in both configurations. A possible explanation can be that larger electron temperature gradients at the separatrix region in USN (as observed at the LFS with the Thomson scattering diagnostic), can lead to higher Er shear (assuming similar electron and ion temperatures at the separatrix). In this case lower density fluctuations levels and a reduced radial transport can be expected in USN, as observed.

DN and LSN magnetic configurations (I-phase discharges):

In DN configuration, fluctuations are found to be lower than in LSN displaying a modest radial variation at the SOL. Changing the magnetic configuration from LSN to DN affects $\delta n_e/n_e$ at the SOL but not at the edge. The largest poloidal asymmetry is found in DN due to the pronounced reduction of $\delta n_e/n_e$ at the HFS SOL. The ratio of density fluctuations DN/LSN at the SOL ($\rho \sim 1.03$) is around 0.2 at the HFS and 0.5 at the LFS. The strong reduction of density fluctuations at the HFS in DN indicates the disconnection of the LFS and the HFS plasmas, therefore providing a clear support for a strong ballooning transport. The reduction starts at the high frequencies (above 200 kHz) expanding to the lower frequencies. This suggests that in the SOL plasma a direct connection exists between LFS and HFS high frequency turbulence. At the LFS edge, the lower $\delta n_e/n_e$ observed in LSN than in DN can be associated with a higher E_r shear according to the turbulence shear stabilization theory [145–147].

Edge density fluctuations in I-phase at the LFS:

High frequency density fluctuations (> 250 kHz) are strongly modulated by the LCOs (at $f \sim 1.5$ kHz) inside and close to the separatrix ($0.95 < \rho < 1$), and this modulation is not observed at the SOL.

The modulation frequency corresponds to the frequency of the limit cycle oscillations inher-

ent to the I-phase, as confirmed by the spectrogram of the magnetic signals. The modulation of density fluctuations (measured by reflectometry) does not occur simultaneously along radius, which suggests that suppression or/and enhancement of turbulence is not radially uniform. The modulation propagates radially inwards with an estimated velocity of $\sim 200 - 300$ m/s, in good agreement with result obtained previously at AUG with Li beam diagnostic and Doppler reflectometry [37]. This value is also similar to the velocity obtained at TJ-II with Doppler reflectometry [207].

L-mode density ramp-up discharges with divertor detachment:

At the SOL, radial profiles of density fluctuation levels display different HFS and LFS responses to the divertor detachment. A conclusion cannot be drawn at the edge because data is limited during the density ramp-up, due to the movement of the probed layers from the edge to the SOL. At the LFS SOL, the low and high frequency components of fluctuations (lower and higher than 15 kHz) evolve differently: LF fluctuations increases while the HF decreases. Inside the separatrix, the LF frequency components do not increase and the behavior of HF/LF fluctuations cannot be clearly distinguished.

In the complete detachment state, the increase of fluctuations at the LFS SOL is dominated by the LF components and is accompanied by the flattening of the n_e profiles at the SOL. Both observations are associated with enhanced filamentary activity.

In the HFS SOL, the density fluctuations levels are lower than at the LFS, as expected from a ballooning-like transport. At fixed ρ_{pol} positions, relative density fluctuations do not change significantly in the different detachment states. This behavior changes abruptly in the far SOL region ($\rho_{pol} > 1.06$) at the beginning of the complete detachment state. Fluctuations start to increase suddenly, this increase being associated with faster filaments propagating from the LFS to the HFS along the magnetic field lines.

The strong HFS/LFS poloidal asymmetry of density fluctuation behavior at the SOL may be explained by different transport mechanisms occurring in high density discharges: a dominant contribution of filamentary transport at the LFS, while the HFS profiles may be influenced by the development of a HFSHD front [109].

Summary:

This thesis presents a study of turbulence at the HFS and the LFS at the AUG tokamak using mainly data from the FM-CW reflectometry diagnostic, covering regions both inside and outside the separatrix thus providing a consistent picture about turbulence poloidal asymmetries. HFS data is most relevant due to the lack of density data in this region. A tool was developed to

estimate phase from FM-CW reflectometry that is essential to obtain the unique HFS and LFS measurements of the density fluctuation levels.

Experimental studies show that density fluctuation levels ($\delta n_e/n_e$) in L-mode increase with radius at both the HFS and the LFS. In the LFS SOL, density fluctuations are a factor of two larger than at the HFS, which is in agreement with ballooned transport.

It is shown that magnetic configuration and divertor conditions influence mainly the midplane turbulence at the SOL, while at the edge density fluctuations are more sensitive to confinement modifications.

The level of density fluctuations changes for each magnetic topology, which can be associated with a variable E_r shear. Dedicated simulations performed with the gyrofluid GEMR code are in a good agreement with the experimental results from reflectometry. In I-phase, the HF components of turbulence at the LFS edge are strongly modulated by the LCOs, displaying a non uniform radial dependence. Our study shows that midplane turbulence at the SOL is influenced by the divertor conditions. In the LFS SOL, low frequency components are responsible for the increase of density fluctuations along the discharge, which is in agreement with an enhanced convection of filaments. In the HFS, the level of fluctuations is lower as expected from ballooned transport. At the HFS far-SOL, a strong increase is seen suggesting that faster filaments originated at the LFS propagate to the HFS.

Outlook

Our study showed that FM-CW reflectometry diagnostic at AUG can measure plasma turbulence asymmetries due to its unique HFS/LFS measuring capabilities, providing a joint picture of plasma turbulence and its poloidal asymmetries at the edge and SOL regions. This can contribute to validate and/or improve theoretical and simulation models, which is essential for understanding the physics mechanisms driving turbulence as well as the related radial transport.

Our study of the influence of plasma conditions on turbulence confirmed previous findings in other machines and also in AUG, namely the ballooned character of transport (found in all experiments). The study reveals also new properties of turbulence, such as for example, lower density fluctuation levels in USN (featuring higher L-H transition power threshold) than in LSN and a strong connection between the midplane turbulence and the divertor conditions. The results open new lines of research, for example the investigation of the mechanism behind the lower density fluctuations in USN that seems to be associated with E_r shear. Also, the connections between turbulence development and shear flows should be clarified. Complementary

measurements in discharges with different magnetic configurations in both direct/reversed magnetic field, for several average densities would be important as they are known to influence the SOL/divertor conditions.

Turbulence data (HFS/LFS) from FM-CW reflectometry at edge and SOL, together with E_r measurements at the LFS from Doppler reflectometry (and CXRS) should contribute for better understanding not only the role of E_r shear but also the driving mechanisms of edge/SOL turbulence and the L-H transition. Detailed simulations with GEMR code using as input parameters the data from the above experiments are important to support the investigation.

The results obtained in DN (I-phase) suggest a direct connection between micro scale turbulence at HFS and LFS SOL plasmas. Those data were measured in DN configuration during a magnetic scan resulting in unstable plasma conditions. A new set of experiments in stable L-mode DN configuration would allow a more comprehensive investigation of the SOL connections between different scales turbulence both at the HFS and the LFS.

In I-phase, the turbulence was found to be modulated by LCOs at the LFS edge. Measurements at the HFS edge could not be performed due to the steepening of the HFS density profiles moving the probed layers into the SOL. Experiments in low density ($n_e \lesssim 3 \cdot 10^{19}$ m^{-3}) discharges would provide the HFS/LFS edge data, enabling to study the poloidal asymmetry of fluctuations. This study is important for the investigation of the mechanism of LCOs that is not still clear. In the theoretical works it is assumed that LCOs can arise from any energy transfer term within the system, where the in-out asymmetry in the pressure takes the role of the prey, and the up-down asymmetric flow perturbation takes the role of the predator [136, 208]. As this mechanism is not restricted to the I-phase, the study of in-out asymmetries of density profiles and fluctuations is also important to analyze cases where the transport is strongly ballooned, as for example during ELMs or other resonance phenomena, including the LCOs.

Our study in density ramp-up discharges with divertor detachment revealed that the behavior of density profile and fluctuations change significantly in complete detachment state. The phenomenon triggering this transition is not clear. Experiments in similar paired discharges are important to have a better description of the evolution of density and fluctuations profiles that is essential to investigate possible threshold parameters for the transition. Results suggest that a possible candidate could be a density threshold being surpassed during the complete detachment state. Discharges with different ramp-up rates may help to establish a finer connection with the detachment states.

From the point of view of the reflectometry diagnostic, the temporal resolution of density profiles should be improved. In our study, the temporal resolution was limited to 1 ms, while the

temporal resolution of the phase data proportional to density fluctuations is 0.5 μs. Presently the FM-CW reflectometry diagnostic can provide density profiles with resolution higher than 1 ms. This is important to perform detailed studies of density fluctuations and density profiles dynamics during L-H transition, I-phase and other phenomena with corresponding frequency range $\lessapprox$ 1 kHz.

Our study of the density fluctuations for changing divertor states provide measurements that are in good agreement with results obtained previously at AUG and other machines thus validating FM-CW reflectometry as a diagnostic for fluctuations in tokamak plasmas. Its capability to measure simultaneously both at the LFS and the HFS opens the way to address key topics such as the connection between the inner and outer sides. The possibility that filaments originated at the LFS may reach the HFS is an important result to understand the influence of the divertor conditions in the radial and parallel transport.

Our analysis was, however, limited by the probing capability of the FM-CW system in fixed frequency that allows only one fixed density layer to be probed per channel and per discharge, that limited the spatial-time coverage of the plasma. Diagnostic upgrades are underway that will extend significantly the spatial-time coverage.

Some open questions were raised by our study that requires further investigation. For example it was observed that during the second phase of CDS, density fluctuation levels do not vary significantly and a modest evolution of the density profiles is observed at the edge and SOL both at the LFS and the HFS despite the density ramp up. Also it was found that high frequency components of density fluctuations at the LFS decrease and it is important to find the radial location of this phenomena with better space resolution measurements. The FM-CW system is planned to be upgraded with hopping capability that will allow several density layers to be probed per channel in each discharge improving greatly the radial resolution and coverage of the fluctuation measurements. Finally, filamentary activity can be studied in more detailed by filament detection using the phase derivative of the FM-CW signal plus the application of conditional averaging techniques [211].

Bibliography

[1] https://www.euro-fusion.org/.

[2] http://iter.rma.ac.be/.

[3] http://w3.pppl.gov/.

[4] J.A. Alonso, "Experimental Techniques in Plasmas, Nuclear Physics and Materials." http://fusionsites.ciemat.es/jaalonso/files/2014/10/ExperimentalTechniques-Notes.pdf, 2014.

[5] F. Chen *Phys. Fluids 8 912*, 1965.

[6] U. Stroth and M. Ramisch *C. R. Physique 7 686–691*, 2006.

[7] S. Ramos, *MHD and fast particle mode studies using fast frequency hopping reflectometers aon the ASDEX Upgrade tokamak*. PhD thesis Universidade Tecnica de Lisboa, 2009.

[8] A. Silva, *The ASDEX Upgrade broadband microwave reflectometry system*. PhD thesis Universidade Tecnica de Lisboa, 2006.

[9] J. Vicente et al. *HTPD to be submitted*, 2018.

[10] S. Potzel et al. *Nucl. Fusion 54 013001*, 2014.

[11] D. Carralero et al. *Nucl. Fusion 54 123005*, 2014.

[12] https://lasers.llnl.gov/.

[13] N. Keishiro *Nuclear Fusion, Cambridge University Press; 1 ed. ISBN-10: 0521113547*, 2009.

[14] L. Spitzer *Phys. Fluids, 1, p. 253*, 1958.

[15] C. Mercier *Nucl. Fusion, 4, p. 213*, 1964.

[16] J. Wesson and D.J. Campbell, *Tokamaks*. OUP Oxford ISBN, 2011.

[17] B.B. Kadomtsev, V.D. Shafranov *Advances in Physical Sciences (in Russian) 139/3 399*, 1983.

[18] F. Chen *Introduction to plasma physics, ISBN o-471-55951-2, Plenum Press, New York*, 1974.

[19] Y. Xu *A general comparison between tokamak and stellarator plasmas, Matter and Radiation at Extremes*, 2016.

[20] F. Wagner et al., "Development of an Edge Transport Barrier at the H-Mode Transition of ASDEX," *Phys. Rev. Lett. 53 1453 - 1456*, 1984.

[21] P.C. Stangeby and J.D. Elder *Nucl. Fusion 35 1391*, 1995.

[22] W. Horton *Rev. Mod. Phys. 71 735*, 1999.

[23] M. Keilhacker et al. *Physica Scripta., Vol. T2/2, 443-453*, 1982.

[24] H. Matsumoto, T. Ogawa, H. Tamai, K. Odajima, et al. *Nucl. Fusion, 27(7):1181*, 1987.

[25] F. Ryter et al. *Nuclear Fusion 49, 062003*, 2009.

[26] J.W. Hughes et al. *Phys. Plasmas 9 3019*, 2002.

[27] T.H. Osborne et al. *Plasma Phys. Controlled Fusion 40 845*, 1998.

[28] W. Suttrop et al. *Plasma Phys. Controlled Fusion 39 2051*, 1997.

[29] C.S. Pitcher et al. *Phys. Plasmas 4 2577*, 1997.

[30] M. Bernert, "Analysis of the H-mode density limit in the ASDEX Upgrade tokamak using bolometry," *PhD Thesis Ludwig-Maximilians-Universität München*, 2013.

[31] R.J. Colchin et al. *Phys. Rev. Lett. 88 255002*, 2002.

[32] R. Colchin et al. *Nucl. Fusion 42 1134*, 2002.

[33] E.R. Solano et al. and JET EFDA Contributors *Proc. 40th EPS Conf. on Plasma Physics*, 2013.

[34] N. Vianello et al. *Proc. 42nd EPS Conf. on Plasma Physics*, 2015.

[35] G. Xu et al. *Nucl. Fusion 54 103002*, 2014.

[36] Z. Yan, G.R. McKee, R. Fonck, P. Gohil, R.J. Groebner and T.H. Osborne *Phys. Rev. Lett. 112 125002*, 2014.

[37] G. Birkenmeier et al. *Nucl. Fusion 56, 086009*, 2016.

[38] P. Manz et al. *Phys. Plasmas 23, 052302*, 2016.

[39] G.D. Conway et al. *Phys. Rev. Lett. 106 065001*, 2011.

[40] G.R. Tynan et al. *Nucl. Fusion 53, 073053*, 2013.

[41] P. Manz et al. *Phys. Plasmas 19, 072311*, 2012.

[42] L. Schmitz et al. *Phys. Rev. Lett. 108, 155002*, 2012.

[43] S.J. Zweben et al. *Plasma Phys. Controlled Fusion 49 S1–S23*, 2007.

[44] C. Hidalgo *Plasma Phys. Controlled Fusion 37 A53*, 1995.

[45] C. Silva, *Relatório para Provas de Habilitação para o Exercício de Funções de Coordenação Científica em Engenharia Física Tecnológica*. Universidade Tecnica de Lisboa, 2012.

[46] R.H. Kraichnan *Fluid Mechanics 47, p525*, 1971.

[47] M. Endler *J. Nucl. Mater. 266–269 84*, 1999.

[48] B.A. Carreras *IEEE Trans. Plasma Sci. 25 1281*, 1997.

[49] B.A. Carreras *J. Nucl. Mater. 337–339 315*, 1997.

[50] J.A. Boedo et al. *Phys. Plasmas 8 4826*, 2001.

[51] J. Boedo *J. Nucl. Mater., 390-291 29*, 2009.

[52] P.C. Liewer *Nucl. Fusion, 25 1281*, 1985.

[53] A.J. Wootton et al. *Phys. Fluids B, 2 2879*, 1990.

[54] C. Hidalgo ,M.A. Pedrosa and B. Goncalves *New Journal of Physics 4 51.1–51.12*, 2002.

[55] B.A. Carreras et al. *Phys. Plasmas, 6 1885*, 1999.

[56] M.A. Pedrosa et al. *Phys. Rev. Lett., 82 3621*, 1999.

[57] G.Y. Antar et al. *Phys. Plasmas 10 419*, 2003.

[58] B. Scott *Plasma Phys. Controlled Fusion 39 1635*, 1997.

[59] S. Niedner, B.D. Scott, U. Stroth *Plasma Phys. Controlled Fusion 44 397*, 2002.

[60] B.B. Kadomcev, V.D. Shafranov, "Magnetic confinement of plasma," *Uspekhi physicheskikh nauk, 139, 3, 399-431*, 1983.

[61] W. Horton, B.G. Hong, W.M. Tang *Phys. Fluids 31 2971*, 1988.

[62] F. Romanelli *Phys. Fluids B 1 (1989) 1018*, 1989.

[63] B.B. Kadomtsev, O.P. Pogutse, in: M.A. Leontovitch *Reviews of Plasma Physics, vol. 5, Consultant Bureau, New York, p. 249*, 1970.

[64] H. Tanaka et al. *Nucl. Fusion 49 065017*, 2009.

[65] G.S. Kirnev et al. *Plasma Phys. Controlled Fusion 46 621*, 2004.

[66] G.S. Kirnev et al. *Nucl. Fusion 45 459*, 2005.

[67] B.A. Carreras et al. *Phys. Plasmas 8 3702*, 2001.

[68] S.J. Zweben et al. *Nucl. Fusion 23 825*, 1983.

[69] S.J. Zweben et al. *Phys. Fluid B, 1 2058*, 1989.

[70] C. Hidalgo et al. *Plasma Phys. Controlled Fusion 43 A313*, 2001.

[71] C. Hidalgo et al. *J. Nucl. Mater. 313–316 863*, 2003.

[72] D.L. Rudakov et al. *Plasma Phys. Controlled Fusion 44 717*, 2002.

[73] A.H. Nielsen et al. *Phys. Plasmas 3 1530*, 1996.

[74] R.A. Moyer et al. *J. Nucl. Mater. 241–243 633*, 1997.

[75] J. Stockel et al. *Plasma Phys. Controlled Fusion, 41 A577*, 1999.

[76] B. LaBombard et al. *Phys. Plasmas 8 2107*, 2001.

[77] A.J. Wootton et al. *Plasma Phys. Controlled Fus. 30 (11) 1479*, 1988.

[78] E. Sánchez et al. *Plasma Phys. 7 1408*, 2000.

[79] G.S. Xu et al. *Phys. Plasma, 13 102509*, 2006.

[80] J.A. Alonso et al. *Plasma Phys. Controlled Fusion, 48 B465*, 2006.

[81] G. M. et al.

[82] O.E. Garcia et al. *Plasma Phys. Controlled Fusion 48 L1*, 2006.

[83] O.E. Garcia et al. *Plasma Phys. Controlled Fusion 49 B47*, 2007.

[84] O.E. Garcia et al. *Nucl. Fusion 47 667*, 2007.

[85] R.J. Maqueda et al. *Rev. Sci. Instrum. 72 931*, 2001.

[86] J.L.Terry et al. *Phys. Plasmas 10 1739*, 2003.

[87] E.A. Novikov and R.W. Stewart, "The intermittency of turbulence and the spectrum of energy dissipation fluctuations," *Izv. Akad. Nauk. Ser. Geophys., 3, 408*, 1964.

[88] S. Krasheninnikov, "Multifaceted Physics of Edge Plasma In Magnetic Fusion Devices," *ICPP International Congress LAWPP Latin American Workshop*, 2010.

[89] V.P. Budaev, S.P. Savin, L.M. Zelenyi, "Observations of intermittency and generalized self-similarity of edge turbulence layers in laboratory and magnetospheric plasmas: towards quantifying the transport characteristics," *Uspekhi physicheskikh nauk, 181, 9, 905-949*, 2011.

[90] C. Hidalgo et al. *Plasma Phys. Controlled Fusion, 44 1557*, 2002.

[91] D.A.D'Ippolito, J. R. Myra, and S. J. Zweben *Phys. Plasmas, 18 060501*, 2011.

[92] M. Endler et al. *Nucl. Fusion 35 1307*, 1995.

[93] S. Krasheninnikov et al. *Phys. Lett. A 283 368*, 2001.

[94] G.Y. Antar et al. *Phys. Rev. Lett. 87 065001*, 2001.

[95] B. LaBombard and B. Lipschultz *Nucl. Fusion 27 81*, 1987.

[96] V.A. Vershkov et al. *J. Nucl. Mater. 241–243 873*, 1997.

[97] N. Smick et al. *Journal of Nuclear Materials 337–339 281–285*, 2005.

[98] N. Asakura, N. Ohno, H. Tanaka, H. Kawashima, T. Nakano *Journal of Nuclear Materials 390–391 364–367*, 2009.

[99] C. Silva et al. *Plasma Phys. Controlled Fusion 53 085021*, 2011.

[100] R. Pitts, G. Vayakis and G.F. Matthews *J. Nucl. Mater. 175–177 893*, 1990.

[101] J. Stockel et al. *Plasma Phys. Controlled Fusion 47 635*, 2005.

[102] W.M. Stacey *Phys. Plasmas 9 3874*, 2002.

[103] P.J. Catto and A.N. Simakov *Phys. Plasmas 13 052507*, 2006.

[104] G.R. Tynan et al. *Phys. Rev. Lett. 68 3032*, 1992.

[105] P. Tamain et al. *J. Nucl. Mater. 390–391 347*, 2009.

[106] M. Lehnen et al. *Nucl. Fusion 43 168*, 2003.

[107] J. Boedo et al. *J. Nucl. Mater. 196–198 489*, 1992.

[108] S. Potzel et al. *J. Nucl. Mater. 462 541*, 2015.

[109] L. Guimarais et al., draft *Nucl. Fusion 58, 026005*, 2018.

[110] B. Lipschultz et al. *Nucl. Fus. 24 977*, 1984.

[111] D. Jablonski et al. *J. Nucl. Mater. 241–243 782*, 1997.

[112] A. Rudyj, " Untersuchung Transportrelevanter Fluktuationen in der Randschicht Von ASDEX," *PhD Thesis Technische Universität München IPP report III/160*, 1990.

[113] B. LaBombard et al. *Nucl. Fusion 44 1047-1066*, 2004.

[114] T.T. Ribeiro and B. Scott *Plasma Phys. Controlled Fusion 50 055007*, 2008.

[115] C.J. Boswell et al. *Plasma Phys. Controlled Fus. 46 1247*, 2004.

[116] S.C. Liu et al. *Phys. Plasmas 19 042505*, 2012.

[117] B. LaBombard et al. *Nuclear Materials and Energy 000 1–9*, 2016.

[118] B. Hnat et al. *Nucl. Fusion 48 085009*, 2008.

[119] C. Fenzi et al. *Phys. Plasmas 12 062307*, 2005.

[120] J. Schirmer et al. *Nucl. Fusion 46 S780–S791*, 2006.

[121] V. Rozhansky et al. *Nucl. Fusion 49 025007*, 2009.

[122] J.E. Rice et al. *Nucl. Fusion 38 75*, 1998.

[123] ASDEX TEAM *Nucl. Fusion 29 1959*, 1989.

[124] F. Ryter et al. *Nucl. Fusion 36 1217*, 1996.

[125] A. Hubbard et al. *Plasma Phys. Contr. Fusion 40 689*, 1998.

[126] P. Gohil et al. *Journal of Physics: Conference Series 123 012017*, 2008.

[127] F.L. Hinton et al. *Nucl. Fusion 25 1457*, 1985.

[128] F.L. Hinton and G.M.Staebler *Nucl. Fusion 29 405*, 1989.

[129] T.N. Carlstrom et al. *Plasma Phys. Controlled Fusion 40 669*, 1998.

[130] N. Smick et al. *Nucl. Fusion 53 023001*, 2013.

[131] D. Carralero et al. *Phys. Rev. Lett. 115 215002*, 2015.

[132] N. Asakura et al. *J. Nucl. Mater. 241–243 559*, 1997.

[133] M.R. Wade et al. *J. Nucl. Mater. 266–269 44*, 1999.

[134] R.A. Pitts et al. *J. Nucl. Mater. 290–293 940–6*, 2001.

[135] O.E. Garcia et al. *Phys. Plasmas 13 082309*, 2006.

[136] P. Manz et al. *Phys. Plasmas 22, 022308*, 2015.

[137] D.A. D'Ippolito et al. *Phys. Plasmas 19 102301*, 2012.

[138] V. Budaev et al. *Plasma Phys. Controlled Fusion 35 429*, 1993.

[139] R.A. Moyer et al. *J. Nucl. Mat. 266 1145*, 1999.

[140] S. Braginskii, *Reviews of Plasma Physics vol 1*. New York: Consultants Bureau p 205, 1965.

[141] B.N. Rogers, J.F. Drake and A. Zeiler *Phys. Rev. Lett. 81 4396*, 1998.

[142] X.Q. Xu et al. *J. Nucl. Mater. 266 993*, 1999.

[143] B. D. Scott *Contrib. Plasma Phys. 46, 714*, 2006.

[144] T.T. Ribeiro and B. Scott *Plasma Phys. Controlled Fusion 47 1657*, 2005.

[145] H. Biglari, P.H. Diamond and P.W. Terry *Phys. Fluids B 2 1*, 1990.

[146] K. Burrell *Phys. Plasmas 6 4418*, 1999.

[147] T.S. Hahm et al. *Phys. Plasmas 6 922*, 1999.

[148] K. G. Budden, *Radio Waves in the Ionosphere*. Cambridge University Press, 1961.

[149] V. Ginzburg, *The Propagation of Electromagnetic Waves in Plasmas*. Pergamon Press, Second edition, 1970.

[150] F. Simonet, "Measurement of electron density profile by microwave reflectometry on tokamaks," *Review of Scientific Instruments, 56(5):664–669*, 1985.

[151] F. Simonet, "Etude de la reflectometrie hyperfrequence en modes ordinaire et extraordinaire pour la mesure du profil radial et des fluctuations locales de la densite electronique dans les tokamaks," *PhD thesis Universite de Nancy I*, 1985.

[152] M. A. Heald and C. B. Wharton, *Plasma Diagnostics with Microwaves*. John Wiley & Sons, 1965.

[153] V. Ginzburg, *Propagation of Electromagnetic Waves in Plasma*. Gordon & Breach Science Publishers Ltd, 1961.

[154] I.H. Hutchinson, *Principles of Plasma Diagnostics*. Cambridge University Press, 2002.

[155] C. Fanack et al. *Plasma Phys. Controlled Fusion 38, 1915 - 1930*, 1996.

[156] T.L. Rhodes et al. *Plasma Phys. Controlled Fusion 40 493–510*, 1998.

[157] S. Heuraux et al. *Rev. Sci. Instrum. 74 (3), 1501*, 2003.

[158] G.D. Conway et al. *Plasma Phys. Controlled Fusion 38, 451*, 1996.

[159] R. Nazikian et al. *Phys. Plasmas 8, 1840*, 2001.

[160] N. Bretz *Phys. Fluids B 4, 2414*, 1992.

[161] K.P. Singh et al. *Phys. Plasmas 19, 113304*, 2012.

[162] A. Casati et al. *Phys. Rev. Lett. 102, 165005*, 2009.

[163] F. da Silva et al. *Journal of Comp. Physics 203 467*, 2005.

[164] B. Streibl et al. *Fusion Sci. Technol. 44 578*, 2003.

[165] B. Nold, G. D. Conway, T. Happel, et al. *Plasma Phys. Controlled Fusion 52, 065005*, 2010.

[166] G.D. Conway et al. *Plasma Phys. Controlled Fusion 46 951*, 2004.

[167] J. J. Thomson, *Conduction of Electricity through Gases*. Cambridge Univ. Press., 1906.

[168] H. Murmann et al. *Rev. Sci. Instrum. 63, 4941*, 1992.

[169] B. Kurzan et al. *Plasma Phys. Controlled Fusion 46, 299–317*, 2004.

[170] https://www.aug.ipp.mpg.de/~yagg/diag/principle.html.

[171] B. Kurzan and H. D. Murmann *Rev. Sci. Instrum. 82, 103501*, 2011.

[172] M. Bornatici et al. *Nucl. Fusion 23 1153*, 1983.

[173] H. Hartfuss et al. *Plasma Phys. Controlled Fusion 39 1693*, 1997.

[174] A. Bogomolov, *Visualisation of instabilities at the edge of ASDEX Upgrade plasmas*. PhD thesis Technische Universiteit Eindhoven, 2016.

[175] K. McCormick et al. *Fusion Eng. Design 34-35 125*, 1997.

[176] E. Wolfrum et al. *Rev. Sci. Instrum. 64 2285*, 1993.

[177] J. Schweinzer et al. *Plasma Phys. Controlled Fusion, 34 1173 1183*, 1992.

[178] M. Willensdorfer et al. *Rev. Sci. Instrum. 83 023501*, 2012.

[179] W. Schneider et al. *Fusion Eng. Des. 48, 127*, 2000.

[180] P. McCarthy et al., "The CLISTE Interpretive Equilibrium Code," *IPP-Report 5/85*, 1999.

[181] R. Fischer et al. *Fusion Sci. and Technol. 58/2 675*, 2010.

[182] F. Ryter et al. *Plasma Phys. Controlled Fusion 40 725–729*, 1998.

[183] G.D. Conway, G. Vayakis, J.A. Fessey and D.V. Bartlett *Rev. Sci. Instrum. 70, 3921*, 1999.

[184] E. Jakeman , C.J. Oliver and E.R. Pike, "Optical homodyne detection," *Advances in Physics, 24:3, 349-405*, 1975.

[185] R. V. Churchill, *Complex Variables and Applications*. New York: McGraw-Hill, 1960.

[186] P. Henrici, *Applied and computational complex analysis, Volume 1*. John Wiley and Sons, Inc., New York, 1988.

[187] M. Johansson, *The Hilbert transform. Master thesis. Mathematics/Applied mathematics*. Vaxjo University.

[188] E. Bedrosian et al., "On the quadrature approximation to the Hilbert transform of modulated signals," *Proc. IEEE, 51, 868 – 869*, 1963.

[189] S.-H. Seo et al. *Rev. Sci. Intrum. 76, 036104*, 2005.

[190] K. Shinohara et al. *Fusion Eng. Des., 34-35 433*, 1997.

[191] E. Mazzucato et al. *Phys. Rev. Lett., 77(15) 3145*, 1996.

[192] B. Brâ̂nas et al. *Rev. Sci. Instrum., 70(1) 1025*, 1999.

[193] E. Mazzucato and R. Nazikian *Rev. Sci. Instrum., 66 2 1237*, 1995.

[194] A. Ejiri et al. *Plasma Phys. Controlled Fusion, 39 (12) 1963*, 1997.

[195] G.D. Conway et al. *Plasma Phys. Controlled Fusion, 44 (4) 451*, 2002.

[196] A. V. Oppenheim, R. W. Schafer and J. R. Buck, *Discrete-Time Signal Processing, 2nd Ed.* Upper Saddle River, NJ: Prentice Hall, 1999.

[197] G. Birkenmeier *personal communication*, 2014.

[198] T. N. Carlstrom, R. J. Groebner, C. Fenzi, G. R. McKee, R. A. Moyer, and T. L. Rhodes *Plasma Phys. Contr. Fusion 44 A333*, 2002.

[199] L. D. Horton *Plasma Phys. Controlled Fusion 42 A37*, 2000.

[200] P. H. Diamond, Y.-M. Liang, B. A. Carreras, and P. W. Terry *Phys. Rev. Lett. 72, 2565*, 1994.

[201] E.-J. Kim and P. H. Diamond *Phys. Plasmas 10, 1698*, 2003.

[202] S. Graça et al. *Plasma Phys. Controlled Fusion 49, 1849–1872*, 2007.

[203] S. Graça,G.D. Conway, E. Viezzer, A. Silva, L. Cupido, M.E. Manso and the ASDEX Upgrade Team, 40th EPS Conf., Espoo, Finland. http://ocs.ciemat.es/EPS2013PAP/pdf/P4.110.pdf, 2013.

[204] S.-I. Itoh, K. Itoh et al. *Plasma Phys. Controlled Fusion 49, L7-L10*, 2007.

[205] Y. Nagashima, K. Itoh et al. *Plasma Phys. Controlled Fusion 49, L7-L10*, 2007.

[206] S.H. Muller et al. *Phys. Plasmas 21 042301*, 2014.

[207] T. Estrada, C. Hidalgo, T. Happel and P. H. Diamond *PRL 107, 245004*, 2011.

[208] B. D. Scott *New J. Phys. 7, 92*, 2005.

[209] D. Carralero et al. *Nucl. Fusion 57 056044*, 2017.

[210] J.A. Boedo *J. Nucl. Mater. 390–391, 29–37*, 2009.

[211] J. Vicente, *Plasma Filament Studies using Microwave Reflectometry on the ASDEX Upgrade tokamak*. PhD thesis Universidade de Lisboa Insituto Superior Técnico and Università degli Studi di Padova, 2015.

[212] P. Manz et al. *Nucl. Fusion 55, 083004*, 2015.

[213] D. Prisiazhniuk et al. *12th Int. Reflectometry Workshop FZ Jülich, Germany*, 2015.

Appendix A

Appendix chapter

A.1 Envelope and cross-coherence analysis

Envelope and cross-coherence analysis is used in this work to study a possible modulation of microscopic density fluctuations by meso-scale structures [204, 205]. The envelope analysis technique was applied previously [212] to the hopping and FM-CW reflectometers data at AUG to study the modulation of the weakly coherent mode (WCM) by geodesic acoustic modes (GAMs) in I-mode and to the poloidal correlation reflectometer to extract the turbulence modulations by GAMs [213].

The envelope of signal $s(t)$ is given by:

$$Env(t) = \sqrt{Re(s(t))^2 + Im(s(t))^2} \tag{A.1}$$

, where the real part in this work is measured directly by FM-CW reflectometer and the imaginary part deduced in frequency space from the Fourier transform $s(\omega)$ and is given by $-i \cdot sgn(\omega)s(\omega)$, where sgn is the signum function that extracts the sign of a real part. The inverse Fourier transform of this relation is the convolution $s(t) * 1/(\pi t) = H(s(t))$, which is the Hilbert transform by definition (see section 5.2.1).

Coherence (magnitude-squared coherence) is used to estimate a degree of relationship between two signals $x(t)$ and $y(t)$ as a frequency function:

$$C_{xy}(f) = \frac{|P_{xy}(f)|^2}{P_{xx}(f)P_{yy}(f)} \tag{A.2}$$

, where $P_{xy}(f)$ is cross-power spectrum between $x(t)$ and $y(t)$, $P_{xx}(f)$ and $P_{yy}(f)$ are power spectra of $x(t)$ and $y(t)$, respectively.

The number of data sets N_{av} defines the minimum level of statistical significance σ_l in the

coherence, if data sets are statistically independent, as:

$$\sigma_l = 1/\sqrt{N_{av}} = \frac{1}{\sqrt{L/n_{fft}}} \tag{A.3}$$

, where L is the signal length and n_{fft} is the number of FFT points. There is a compromise between minimizing the statistical noise level (number of averages) and maximizing the frequency resolution in the spectra (number of FFT points).

In this work the envelope of the density fluctuations measured by reflectometry is obtained by applying the Hilbert transform to the high pass filtered signal (typically, $f >$ 250 kHz). Then the increase of cross-coherence between the envelope and the measured signals indicates the existence of an $\delta n_e/n_e$ amplitude modulator and display a frequency of this modulator. The evolution of the $\delta n_e/n_e$ modulation along the discharge was also investigated by computing the temporal evolution of the maximum in the cross-coherence between signal and its envelope.